ACTIVE INTERROGATION METHODS FOR DETECTION OF SPECIAL NUCLEAR MATERIAL

by

Haori Yang

A dissertation submitted in partial fulfillment
of the requirements for the degree of
Doctor of Philosophy
(Nuclear Engineering and Radiological Sciences)
in The University of Michigan
2009

Doctoral Committee:

Professor David K. Wehe, Chair
Professor Frederick D. Becchetti
Professor Ronald F. Fleming
Assistant Research Scientist Mark D. Hammig

Dedication

To My Family and Friends

Acknowledgements

It would not be possible for me to finish this work without the help from many people. I would first like to thank my advisor, Professor David Wehe, for being supportive of my education and research. I have enjoyed our many discussions concerning my research topic. I appreciate his understanding and encouragement throughout the PhD journey. I am also grateful to my committee members, Prof. Ronald Fleming, Dr. Mark Hammig and Prof. Frederick Becchetti, who provided thoughtful questions and suggestions. I also want to thank Mr. James Berry for his willingness to listen to my questions and his ability to solve just about any of them.

I would like to recognize Mr. Bruce Curran from the department of Radiation Oncology, Dr. Martin Jones from the Ford Non-Destructive Evaluation Facility, and Dr. David Bartels from the Radiation Laboratory of the University of Notre Dame, for letting me use their facilities to conduct experiments. Thanks to Dr. Lister from Argonne National Laboratory for loaning us the HPGe detector.

My graduate student life at Michigan has been a wonderful experience. It wouldn't be like this without the company of my wonderful friends. Thanks to Stephen Anderson, Paul Barton, Troy Becker, Yan Cao, Weijiang Duan, Wei Guo, Jason Hayward, Manhee Jeong, Wei Ji, Hao Jiang, Willy Kaye, Kihyun Kim, Ben Kowash, Wonhoo Lee, Xiaoping Li, Liang Liang, Liyuan Liang, Jean Peng, Yongping Qiu, Rui Shu, Huarui Sun, Hao Wang, Weiyi Wang, Zhi Wang, Sunny Wu, Fang Xiang, Dan Xu, Jinan Yang, Yidan Yuan, Tingting Zhao, Yuefeng Zhu, for making my time at Michigan much more exciting and interesting than just research. I also want to thank Ms. Peggy Gramer for her kindness and her willingness to help me all the time.

I want to thank my parents for always being there for me. Their love and support mean very much to me. Last but not least, I want to thank my girlfriend, Annie. Her love and caring have always kept me company.

Table of Contents

List of Tables

List of Figures

List of Appendices

Abstract

After the attack on the world trade center, homeland security has turned into a major concern internationally. Effort is being made to find accurate, efficient, and practical ways to prevent smuggling of Special Nuclear Materials (SNM). Although passive techniques may be equally accurate in some cases, active interrogation methods offer unique flexibility: the energy and intensity of the interrogating radiation can be adjusted to provide an appropriate response intensity, the energy of the interrogation radiation can be adjusted to generate different responses from different nuclides, and in contrast to passive methods, active interrogation techniques can be applied to both low- and high-density materials, and even materials shielded with high-density materials.

This work will examine detection of SNM by studying two active interrogation methods: photon induced fission in fissile materials and Nuclear Resonance Fluorescence (NRF) reactions between incident photons and nuclei in target materials. This effort includes system simulations using Monte Carlo methods, digital spectroscopic measurement system development, and experimental demonstrations of the two detection techniques.

CHAPTER 1

Introduction

Active interrogation techniques have been used for more than 100 years since the discovery of X-rays. The primary focus of these techniques has been radiographic imaging. Various active interrogation systems have been developed during the last century. Until recently, these techniques haven't been widely used except in medical and special industrial applications. The main reasons are the cost and complexity of such equipment, the ability of passive detection methods to provide accurate results, and the concerns of radiation safety issues related to the deployment of radiation emitting systems outside of lab-coat environments. But in the last decade, especially after 9/11, security has become a dominant concern. Among all the possible terrorism scenarios, those ones involved with high Z fissile materials seem to evoke the most concern, probably because of the small volume of material needed to make a catastrophic impact.

Ninety percent of the trade goods brought into the U.S. each year enter through its 361 seaports [1]. The west coast ports of Los Angeles, Long Beach, Oakland, and Seattle are currently processing 11,000 containers per day, or 8 per minute on a 24/7 basis. The concern is that terrorists could use any one of these containers to smuggle SNM into the country. Currently, less than 2% of these containers are ever opened and inspected by customs service. On the other hand, based on an OECD report [2], a successful attack at a seaport would shutdown the entire maritime shipping system for a period up to 10 days

and would produce an economic loss of $58 billion in the U.S. alone. Thus, the ultimate goal is for every container entering the U.S. to be screened using techniques having an extremely high probability of detecting concealed Special Nuclear Materials (SNM). There are two primary approaches to detecting clandestine SNM: passive detection and active interrogation.

1.1 Passive Nondestructive Inspection

Passive nondestructive detection is based on the detection of naturally emitted gamma rays and/or neutrons from SNM. Because of the absence of an interrogating radiation source, the passive techniques are much simpler to deploy. Detection systems utilizing this approach deliver no radiation dose to the target.

1.1.1 Passive Gamma Ray Detection

As a result of the spontaneous α or β decay in heavy nuclei, γ-rays are emitted during the de-excitation process. These γ-rays have energies that are characteristic of the nuclei from which they come. Some of these γ-rays have sufficient energy to penetrate the fissionable materials that they come from and also the shielding around them. Detection of these γ-rays is the basis of passive γ-ray assay. The energy information can be used to discriminate these γ-rays from signals belonging to the background. Also, it's possible to identify the isotopes based on the energies of their emissions. The net number of counts is interpreted through a predetermined calibration to estimate the number of nuclei present in the sample. Such passive methods have found application in the assay of materials in DOE waste containers [3]. They are also utilized in the radiation portal monitors developed for security applications, for example, RadSentry by Canberra, AT-

900 by SAIC and Detective by ORTEC, together with passive neutron detection techniques.

Although not passive, a transmission density measurement is usually used as a supplement when an accurate γ-ray assay is needed. In this measurement, the sample is irradiated by an external source of photons of energies similar to the energies of interest. The measured attenuation of the photons by the object is used to correct the γ-ray assay results for the expected loss of emitted photons. This can extend the applicability of passive γ-ray assay to dense materials, through which only a fraction of the spontaneously emitted γ-rays can reach the detectors. If the object under investigation is close to the detector, it is usually spun during the scan to improve the uniformity of the sample response. Otherwise it is placed at a sufficient distance from the detector so that the source position variations can be ignored.

Various types of detectors find applications in passive γ-ray detection. These range from detectors with medium energy resolution (e.g., NaI(Tl), CdTe, BGO detector) to ones with excellent energy resolution (e.g. HPGe detector) [3]. Although passive γ-ray assay can provide both the identity and quantity of some nuclides, such as ^{238}U, ^{238}Pu, there are cases where its application is impractical due to the particular isotopes. For example, shielded Highly Enriched Uranium (HEU) is extremely hard to detect using passive γ-ray techniques. As shown in Figure 1.1, the main spectral feature in the bare HEU spectrum is the photopeak from ^{235}U at 185 keV. When lead shielding is placed between the HEU and the detector, this 185 keV peak is greatly attenuated. The primary spectral feature left is due to the isotopic impurity of ^{232}U. ^{232}U decays rapidly and enters the thorium decay chain. The final nuclide in this chain is ^{208}Tl which contributes to the

photopeak at 2615 keV. These 2615 keV gamma rays are very penetrating, thus easy to detect using passive detection technique. However, its intensity is low and it is part of the natural background in the environment, as shown in the background spectrum.

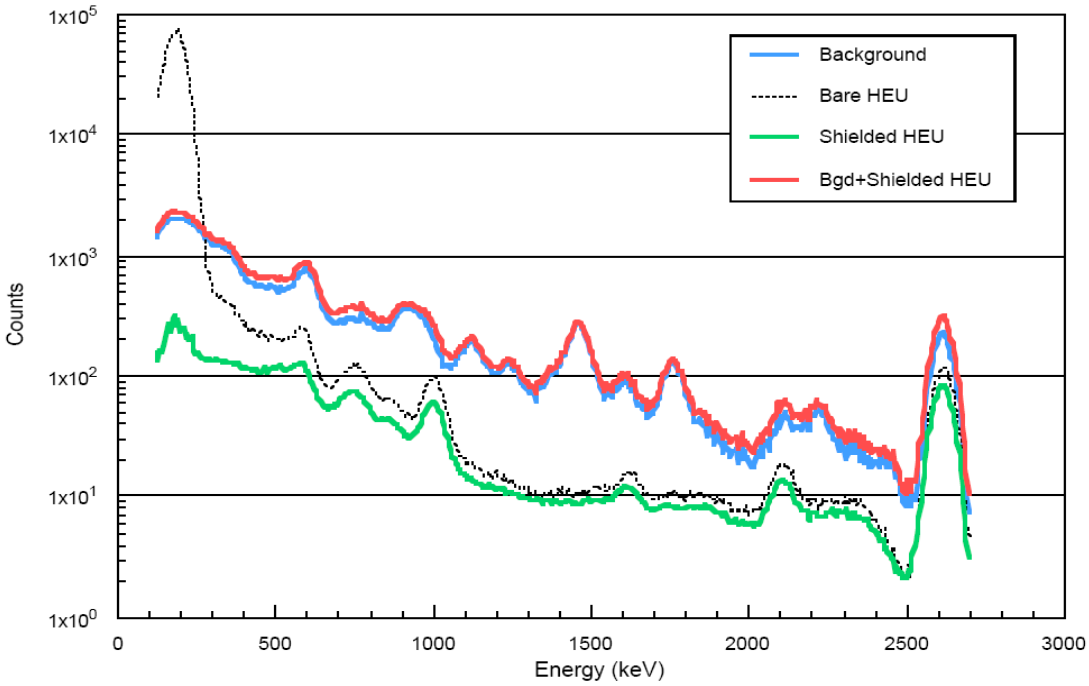

Figure 1.1 Computer synthesized sodium iodide gamma-ray pulse-height spectra from HEU and background radiation using COG code from LLNL [4]

1.1.2 Passive Neutron Detection

Neutrons are emitted as a result of spontaneous fission or as a result of the (α, n) reaction between the α-particles and the nuclides of low atomic number in the matrix material. These neutrons typically have high energies and can penetrate the object and shielding with a high probability. In passive neutron detection methods, these neutrons are detected by multiple detectors surrounding the container. Since the neutron energies are not unique to the nuclides from which they come, energy information is usually not measured in such techniques. Instead, only gross neutron counts are measured to tell the

gross content of neutron-emitting nuclides. The amount of a specific nuclide can still be determined given the neutron emission intensity and relative abundance of each nuclide. This technique is limited to detection of ^{238}U and some plutonium isotopes, where specific activity for spontaneous fission is high. The abundance of elements in the matrix materials surrounding the SNM that can be potential targets for (α, n) reaction will also affect the gross neutron counts [3].

In passive neutron detection, a coincidence technique is often used to distinguish fission neutrons from other sources, including (α, n) reactions in the matrix material. During a spontaneous fission, 2-3 neutrons are usually emitted simultaneously. In contrast, neutrons from other sources are emitted at randomly spaced intervals. For a well designed setup, the probability of detecting multiple fission neutrons within the coincidence time is relatively high. On the other hand, the probability of detecting an (α, n) neutron or background neutron in this time interval is no greater than it would be in any other time interval of the same duration. Thus, detectors working in coincidence mode have a preference to detect fission neutrons.

The two types of detectors mainly used in passive neutron detection are gas filled detectors and plastic detectors. When plastic detectors are used, fission neutrons and γ-rays are both counted with high probability but can be discriminated by pulse shape [5-8]. Plastic detectors, like most organic scintillators, have several advantages over other neutron detectors: faster time response [9-12], and higher amplitude pulses. However, they usually have poorer stability caused by gain drift in the PMT and variance in temperature, are less rugged and are sensitive to γ-rays [13].

Passive neutron detection techniques are usually used together with passive gamma ray detection techniques. They found application in waste assay and security applications as well [14].

1.2 Active Nondestructive Interrogation

Although most SNM naturally emit neutrons and/or γ-rays, the intensity of the spontaneous radiation is low, and the energies of the γ-rays are fairly low in most cases, as shown in Table 1.1. In security applications, it is prudent to assume that the SNM is well shielded to circumvent passive detection. Detecting well shielded SNM using passive techniques, with a low false positive rate in a reasonably short time observation, is almost impossible.

Table 1.1 Natural radiations from Uranium and Plutonium isotopes [15-16]

Nuclide	Decay Mode	Radiation, Type	Intensity ($s^{-1} \cdot g^{-1}$)
^{235}U	α-particle	185.7 keV, γ-ray	4.3×10^{4}
^{238}U	α-particle	1001.1 keV, γ-ray	1.0×10^{2}
		766.4 keV, γ-ray	3.9×10^{1}
	fission	fission neutrons	1.7×10^{-2}
^{238}Pu	α-particle	766.4 keV, γ-ray	1.5×10^{5}
		152.7 keV, γ-ray	6.5×10^{6}
	fission	fission neutrons	2.6×10^{3}
^{239}Pu	α-particle	413.7 keV, γ-ray	3.4×10^{4}
		129.3 keV, γ-ray	1.4×10^{5}
^{240}Pu	fission	fission neutrons	1.0×10^{3}
^{241}Pu	β-particle	208.0 keV, γ-ray	2.0×10^{7}
		164.6 keV, γ-ray	1.8×10^{6}
		148.6 keV, γ-ray	7.5×10^{6}
^{242}Pu	fission	fission neutrons	1.7×10^{3}

1.2.1 Basis of Active Nondestructive Interrogation Targeting SNM

Both neutrons and γ-rays can induce fission in SNM. On average, two to three energetic prompt neutrons and about eight prompt γ-rays are produced in each fission reaction. These radiations are emitted within 10^{-15} s of the time of fission. The fission products continue to emit another six to seven γ-rays and approximately 0.01 to 0.02 neutrons per fission. This radiation from the decay of the fission products is called delayed fission radiation. Both prompt and delayed fission radiation can be detected as the unique signature indicating the presence of special nuclear materials.

The most popular interrogation radiations are neutrons and photons. Both can be produced by either radioactive isotopic sources or charged particle accelerators. Radioactive isotope γ-ray sources are widely used in transmission radiography applications. The γ-ray energies from radioactive decay are high enough to penetrate objects for imaging, but not high enough to induce fission in heavy isotopes. Electron accelerators are common bremsstrahlung photon sources and extend the interrogating photon energy ranges upwards. The maximum photon energy is the energy of the electrons leaving the accelerator. Such bremsstrahlung sources have a broad energy spectrum, as shown in Figure 1.2. For a reasonable portion of the generated photons to induce fission, the endpoint energy has to be well above the fission threshold. However, neutrons from (γ, n) reactions in benign materials will inevitably be emitted under this condition. Table 1.2 shows threshold energies of photofission reaction in heavy metals and threshold energies of (γ, n) reactions in materials of interest. Photon based sources using electron accelerators usually work in pulse mode and the delayed radiation is measured to avoid the effects of neutrons emitted by the (γ, n) reaction. Reactions other

than bremsstrahlung of electrons in heavy target materials can produce cleaner photon sources. For example, 6 -7 MeV γ-rays can be generated through the $^{19}F(p, \alpha\gamma)^{16}O$ reaction [17].

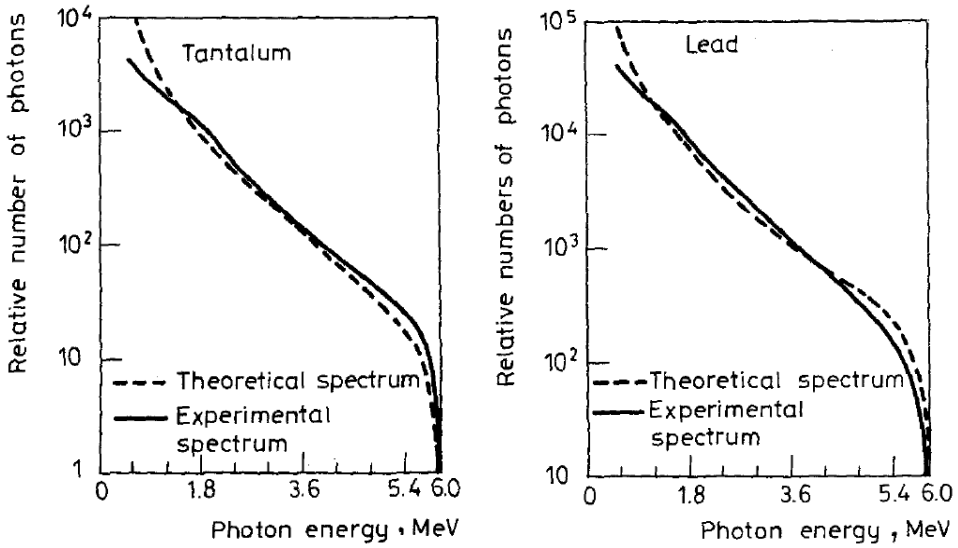

Figure 1.2 Bremsstrahlung spectra for lead (0.12 cm thick) and tantalum (0.007 cm thick) at 6 MeV electron energy [18]

Table 1.2 Photoneutron and photofission thresholds for materials of interest [19]

Material	Isotope	Natural Abundance (atom %)	Photoneutron Threshold (MeV)	Photofission Threshold (MeV)
H	^{2}H	0.01	2.22	2.22
C	^{12}C	98.93	18.72	
	^{13}C	1.07	4.95	
N	^{14}N	99.63	10.55	
	^{15}N	0.37	10.83	
O	^{16}O	99.76	15.66	
	^{17}O	0.04	4.14	
	^{18}O	0.2	8.04	
Al	^{27}Al	100	13.06	
Fe	^{54}Fe	5.85	13.38	
	^{56}Fe	91.75	11.20	
	^{57}Fe	2.12	7.65	
	^{58}Fe	0.28	10.04	
Pb	^{204}Pb	1.4	8.4	
	^{206}Pb	24.1	8.09	
	^{207}Pb	22.1	6.74	
	^{208}Pb	52.4	7.37	
U	^{234}U	0.0055	6.84	5.06
	^{235}U	0.72	5.3	5.31
	^{238}U	99.27	6.15	5.08
Pu	^{239}Pu	0	5.65	5.31
Th	^{232}Th	100	6.44	5.40

Common neutron sources in active nondestructive interrogation are (1) spontaneous fission sources, for example ^{252}Cf, (2) (α,n) sources, such as Am-Li, Am-Be sources, (3) photoneutron (γ, n) sources, utilizing either radioactive isotopes such as an Sb-Be source, or an electron accelerator with a neutron converter, and (4) reactions from accelerated charged particles, for example, (d,d), (d,t), (d,n), and (p, n) reactions. The energy of the incident radiation is very important in the active interrogation techniques, since both the fission cross section and the attenuation of the radiation are energy dependent. Higher energy neutrons are more penetrating and give a more uniform response throughout the nuclear material. However, the fission cross section is lower at high energies, which leads to a lower reaction rate. Photoneutron sources produce

neutrons whose energies can be adjusted by varying the energy of the incident photons. Similarly, the energy of neutrons from (p,n) or (d,n) reactions can be adjusted by using different materials as the target. The neutron energy can also be modified by adding materials between the interrogation source and the sample, to either cutoff low energy neutrons, or slow down high energy neutrons.

A variety of active nondestructive assay techniques can be formulated by combining different incident radiations and observed radiations [20]. These are types of techniques being explored and seem promising for homeland security applications. Active interrogation methods, as compared to passive methods, offer the advantages of adjustable energy and intensity of the interrogating radiation to provide optimal response; a higher intensity of the radiation from induced reactions; and the techniques are applicable to all fissile and fissionable materials.

Most active interrogation techniques rely on the detection and measurement of the delayed radiation, although prompt radiation provides many more counts per fission per unit time than delayed radiation. Thus, techniques that depend on prompt radiation detection have a much higher sensitivity. However, if prompt radiation is to be detected, the fission neutrons and γ-rays have to be distinguished from the interrogation radiation. While the interrogation radiation emitted by the neutron or γ-ray source is usually collimated, it can be scattered into the detector by shielding material, the surrounding environment, or the SNM. Discrimination is usually done based on the different energies of the incident and fission radiation, or the different response of the detector to different particles. It is also possible to distinguish fission induced radiation using coincident counting, similar to that in passive interrogation techniques. The detectors

have to be well shielded from the source so that accidental coincidences do not create a large background.

1.2.2 Active Nondestructive Interrogation Methods for Security Applications Targeting SNM

I. Techniques Involving Detection of Delayed Radiation

A unique signature of the SNM is the delayed neutron emission following a fission reaction. A fission reaction can be induced by interrogating γ-rays or neutrons in SNM. A few systems utilizing accelerators have extended the interrogation γ-ray energies above the photofission threshold (E_γ = 6 ~ 7 MeV) to deliberately induce fission in SNM. Delayed neutrons emitted following the fission process provide a different signal for γ-ray interrogation. Some work in this area has been done by researchers at Idaho National Laboratory, using a tabletop electron LINAC (4 -11 MeV) and also by researchers at Los Alamos National Laboratory (LANL) using a 6, 8, 11 MeV LINAC [21-26].

In addition to delayed neutrons, delayed γ-rays are also observed after a fission reaction. These delayed γ-rays are emitted during the beta decay of many short-lived fission products. Some of these delayed γ-rays have very high energies, thus easy to distinguish from the natural background where high energy γ-rays are rare. The delayed γ-rays signature has some advantages over the delayed neutron signature. First, the intensity of the high energy delayed γ-rays (E_γ > 3 MeV) is about 10 times larger than that of delayed neutrons. Second, the high energy γ-rays are highly penetrating. They typically undergo 10-100 times less attenuation in thick cargo than delayed neutrons [13]. Third, intense high energy delayed γ-rays are a unique signature for SNM. They are not

easily observed after the irradiation of benign materials or in the natural background, nor are they produced in significant amounts by neutron activation of the cargo and surrounding materials [27-30].

The use of the delayed fission product γ-rays after neutron interrogation was investigated by E. Norman and S. Prussin in 2003 [31]. Researchers from LLNL developed a "Nuclear Car Wash" system to detect hidden SNM in cargo containers based on this signature [28-30]. In this system, a d-d neutron source is used as the interrogating radiation source to induce fission in SNM. High energy delayed γ-rays emitted by fission products were collected by a large array of scintillator detectors. Their results showed that the interrogating neutron energy should be kept below 10 MeV. Otherwise, the interference caused by the activation of ^{16}O to produce ^{16}N becomes important. The 7 second β-decay of ^{16}N produces a 6 MeV γ-ray which could possibly cause false alarms in a system based on delayed γ-ray detection. Their work also showed that unwanted collateral effects of the interrogation such as neutron activation are trivial, even in the case when 14 MeV neutrons were used and not moderated.

II. Techniques Involving Detection of Prompt Radiation

In the fission process, whether induced by photons or neutrons, prompt energetic γ-rays and neutrons are emitted within 10^{-15} seconds after the interaction. When a pulsed mode interrogation source is used, prompt radiation can also be emitted between irradiation pulses when the fission is induced by delayed neutrons. For thermal neutron induced fission in ^{235}U, 2.5 prompt neutrons and 7 prompt photons are emitted on the average. Prompt neutron and γ-ray yields from photofission reactions are of similar

magnitudes. But only 0.0158 delayed neutrons are emitted following a thermal fission in ^{235}U [13]. So this type of prompt radiation is rare. In photofission reactions, the ratio of prompt to delayed neutrons increases with incident photon energy.

A technique utilizing prompt neutron detection can dramatically reduce the scan time. A shorter scan time means a lower dose delivered to the cargo and higher throughput of the inspection system. However, prompt radiation detection faces measurement challenges arising from the background of the intense interrogating radiation. The magnitude of the radiation emitted during fission is much smaller compared to that of the incident radiation. With recent breakthroughs in fast data acquisition techniques, utilization of prompt radiation has become more feasible.

Detection based on prompt radiation has been successfully performed by researchers at Idaho National Lab (INL) and Idaho Accelerator Center (IAC) [32]. They developed a state-of-art data acquisition system to handle the extremely high event rate during interrogating pulses. The digitizer they developed has a sampling rate of 2 GS/s. Using an ultra fast SiC detector (sub-nanosecond rising time, insensitive to photons) [33], signals from individual prompt neutrons are recorded during each interrogation pulse. Using a fast EJ-200 (BC-408 equivalent) plastic scintillator, both prompt neutrons and prompt γ-rays were measured. Integration of the total counts over time successfully differentiated depleted uranium (DU) from bismuth or when nothing was present in the beam [32].

In addition to the work by INL and IAC described above, prompt neutrons have also been measured as the signature signal for detection of SNM by researchers at Argonne National Laboratory (ANL). They investigated a system called FIGARO (fissile

interrogation using γ-rays from oxygen) [17, 34-35]. In this technique, 6 – 7 MeV γ-rays produced by the $^{19}F(p, \alpha\gamma)^{16}O$ reaction are used as the interrogating radiation. Since the photoneutron emission threshold is less than 6 MeV in nuclear materials while it is greater than 7.5 MeV in common materials, the (γ, n) background is low. This allows counting of prompt neutrons during irradiation. The smaller photofission cross section at 6 -7 MeV, compared to higher energies, is compensated by the much bigger intensity of prompt neutrons compared to delayed neutrons and the very low (γ, n) background. Research has shown that this technique is a robust method for detection of SNM with low false positives. Effort continues to minimize the neutron background, thus increase the system sensitivity.

III. Nuclear Resonance Fluorescence

Nuclear Resonance Fluorescence (NRF) is the process of resonant excitation of certain nuclear levels of a target nucleus by absorption of electromagnetic radiation and subsequent decay of these levels by re-emission [36]. Because of the uniqueness of the resonance energies, these resonance photons can be used as signatures for isotope identification. Thus, NRF is able to measure the isotopic content for any element with an atomic number greater than that of helium. NRF may be useful to identify threats such as conventional explosives, SNM, toxic materials, and chemical weapons. Bertozzi has pursued the application of NRF for homeland security applications [37-38]. His approach involves exposing materials to an intense photon beam with a continuous energy distribution and detecting the emitted resonance photons unique to each isotope.

1.3 Objectives and Significance of This Work

This thesis research addresses the challenges in detection of hidden SNM in cargo containers for homeland security applications. The work focuses on photon interrogation techniques because these are routinely used for radiography and considered acceptable to the public. Specifically, we look at photon induced fission in which the delayed γ-rays are measured, and the Nuclear Resonance Fluorescence (NRF) technique where resonance photons are collected. We are primarily interested in determining the practicality of these two techniques.

This work demonstrated that fissionable materials can be detected by measurement of delayed γ-rays after irradiation by high energy photons. Furthermore, the content can be identified by analysis of the delayed γ-rays energy spectrum based on observed difference in fission product yields of different nuclear materials. Some fission products have half-lives that allow counting to start as late as minutes after the photon irradiation. The count rate of high energy γ-rays (E_γ >3 MeV) at 2 inches away from our 109 g DU sample was measured to be 3×10^3 cps using a 3 inch by 3 inch NaI detector, 40 seconds after a 24 second irradiation. This will greatly simplify the detection system. It also showed that delayed γ-ray counting can be deployed as a secondary examination technique following radiography of the cargo container without extra dose delivered to the cargo.

The practicality of the NRF technique for detection of SNM in homeland security applications was also studied. Monte Carlo simulation was performed using a modified version of MCNP5 code. An experimental study was also performed in this work. Resonant peaks from various samples, including DU, were observed using an HPGe

detector. This provided the first independent verification of this approach. A lanthanum halide ($LaCl_3$) detector was also used in NRF experiments for the first time. The fast decay constant of the scintillator enhanced the throughput rate of the detection system. The energy resolution of $LaCl_3$ detector was proven to be good enough to measure the strong resonances from selected nuclei.

Two digital spectroscopic measurement systems were developed to handle the extremely high count rate during active interrogation. One system is based on a fast digitizer. Signal processing was conducted in software using a deconvolution method. Much less dead time was achieved without much sacrifice of energy resolution. A separate digital system was developed based on a fast ADC and an FPGA chip. Real-time signal processing was implemented on the FPGA chip using a two-fold Moving Window Deconvolution method. The ability of the FPGA chip to process signal in real time greatly reduced the amount of information needed to be transferred between the DAQ system and the PC.

Utilizing the fast digital spectroscopic measurement system based on a digitizer, delayed γ-rays were measured between adjacent interrogation pulses using a $LaCl_3$ detector. Instead of needing a waiting time of several microseconds as previous work [20,22,39], the measurement of delayed γ-rays started only 5 nanoseconds after the irradiation. By acquiring data closer to the end of the irradiation, a larger intensity of the delayed γ-rays was observed. This leads to greater sensitivity of the system and less dose delivered to the cargo in order to get a reliable detection result.

1.4 Overview of Thesis

The thesis is organized into five chapters. The first chapter provides a brief introduction to the nondestructive detection techniques. The techniques being pursued for homeland security applications are reviewed.

Chapter Two presents the photon induced fission experiments performed at Ford Nondestructive Evaluation Facility utilizing a 9 MeV Varian LINAC. Both analytical and Monte Carlo methods were used to estimate the fission reaction rate induced by high energy x-rays in our DU sample. The delayed gamma rays emitted by fission products were measured using an HPGe detector and a NaI detector. Both the energy and count rate of the high energy delayed gamma rays were analyzed and studied as the signature signals for SNM detection.

In Chapter Three, the development of two digital spectroscopic measurement systems is presented. The first system was based on a National Instruments digitizer and the shaping process was performed in software on a PC. The system was implemented in the photofission experiments at the University of Michigan Hospital. In these experiments, delayed gamma rays were measured between interrogation pulses several nanoseconds after each pulse using a fast $LaCl_3$ detector. The fast decay time of the scintillation detector and the short duration of each pulse after shaping gave the spectroscopy system the ability to handle high counting rates up to 10^6 cps. Taking measurements close to the end of the irradiation greatly enhanced the sensitivity of the detection system. A separate system was developed based on an ADC and an FPGA chip. Real-time signal processing was implemented on the FPGA chip. The performance of both systems is evaluated and the comparison with an analog system is shown.

Chapter Four focuses on the NRF experiments conducted at the University of Notre Dame, using a 3 MeV Van de Graaff electron accelerator. System simulation using a modified version of MCNP5 and the experimental setup are described. Measurement results using an HPGe detector and a $LaCl_3$ detector are presented.

Chapter Five presents conclusions and recommendations for further work.

CHAPTER 2

Detection of SNM Based on Delayed Gamma Rays Emitted by Photon Induced Fission Reaction

The detection of special nuclear materials (SNM) at points of commerce has recently emerged as an important application of radiation detection technology. What makes SNM detection particularly challenging is the inability to control the potential source measurement geometry and environment. This problem has drawn serious attention in the field; a variety of both active and passive approaches, using thermal, electromagnetic, and neutron sensors have been suggested. The preceding work describes an active interrogation method utilizing complex hardware to accomplish the detection of SNM [20-24][26]. In this work, a simpler approach is investigated as an interim solution. Using the existing 9 MeV X-ray radiography units deployed for cargo inspection, delayed fission product gamma rays from induced photofission can be seen minutes after probing a small sample of ^{238}U. By acquiring both time and energy information, a relatively large number of fission products can be identified. We suggested that the use of radiographic imaging in combination with an efficient portable scintillator (capable of detecting gamma rays above 3 MeV) may help implement a cost-effective improvement to existing inspection systems.

2.1 Theory

In order to understand the methods proposed in this work, it is important to review the theory behind radiation detection technology. Nuclear fission induced by γ-rays or neutrons is the most important multiplicative process involved in nondestructive active interrogation. The process produces the most easily recognizable signature that can be used to distinguish the nuclear materials from the benign cargo. In addition to thermal or high-energy neutrons, high-energy γ-rays can also excite a nucleus and cause fission, in a process known as photofission. The detection scheme described in this chapter is based on this process. In the photofission process, the excited nucleus splits into two large fragments following the absorption of a high-energy γ-ray. At the same time, two or three prompt neutrons and several γ-rays are emitted. Figure 2.1 shows the time scale of the fission process and the four types of radiation that are widely used as signature signals for detection of SNM in homeland security applications.

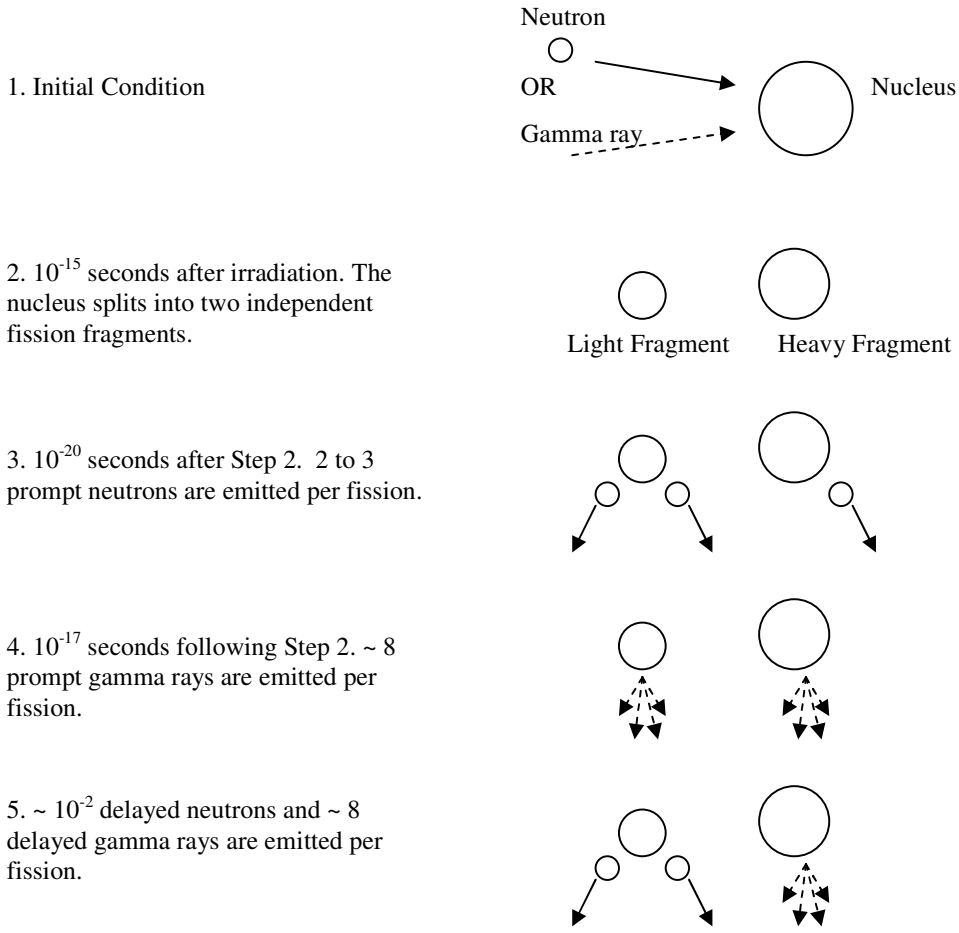

Figure 2.1 Time scale of fission process and four types of radiations emitted [13]

Under the right conditions, prompt neutrons can be used as the signature signal for SNM detection. This is possible when it is easy to distinguish them from the source irradiation and the neutrons produced in surrounding matrix materials. The distinction can be made on the basis of the energy differential between fission neutrons and source neutrons or based on the high multiplicity of the fission neutrons. The yields and energy spectra of the prompt fission neutrons from photofission are not as well known as those from neutron induced or spontaneous fission. The prompt neutron yield observed is typically the sum of the fission neutrons and the photoneutrons from (γ, n) reactions. At

low incident photon energies, large difference of the ratios of prompt neutron yields were reported between ^{235}U and ^{232}Th, ^{235}U and ^{238}U and even between fissile isotopes ^{235}U and ^{239}Pu [39-41]. These observations are very useful when performing isotope identification.

It is important to note here that for practical reasons, it is difficult to use photofission - induced prompt neutrons as signatures in radiation detection. This is because although it is possible to separate the prompt neutrons after a photofission reaction if the energy of the interrogation photons is kept below the (γ, n) reaction threshold, the photofission cross section is small at these energies.

For several reasons, delayed neutrons may be better suited as signatures than prompt neutrons. The advantage of the delayed neutrons over the prompt neutrons is that they can be detected some time after fission reactions. Hence, they can be distinguished from source neutrons and photoneutrons using time discrimination. Additionally, the value and the temporal behavior of the delayed neutron yield vary significantly among different nuclear materials, which make it more easily to distinguish between the nuclear materials. Conventionally, delayed neutrons are registered into six groups based on their decay constants. It is shown in table 2.1 that both the individual group yields and the total yield present significant variance for different isotopes. However, the absolute delayed neutrons yields are very small, ranging from 0.007/fission in ^{239}Pu to about 0.05/fission in ^{238}U.

Table 2.1 Group parameters for delayed neutrons [42]

Group	i	Fractional Group Yield a	Decay Constant λ (sec^{-1})	Group	i	Fractional Group Yield a	Decay Constant λ (sec^{-1})
^{232}Th	1	0.034 ± 0.003	0.0124 ± 0.0003	^{239}U	1	0.038 ± 0.004	0.0129 ± 0.0003
	2	0.150 ± 0.007	0.0334 ± 0.0016		2	0.280 ± 0.006	0.0311 ± 0.0007
	3	0.155 ± 0.031	0.121 ± 0.007		3	0.216 ± 0.027	0.134 ± 0.004
	4	0.446 ± 0.022	0.321 ± 0.016		4	0.328 ± 0.015	0.331 ± 0.018
	5	0.172 ± 0.019	1.21 ± 0.13		5	0.103 ± 0.013	1.26 ± 0.17
	6	0.043 ± 0.009	3.29 ± 0.44		6	0.035 ± 0.007	3.21 ± 0.38
^{233}U	1	0.086 ± 0.004	0.0126 ± 0.0006	^{240}Pu	1	0.028 ± 0.004	0.0129 ± 0.0006
	2	0.274 ± 0.007	0.0334 ± 0.0021		2	0.273 ± 0.006	0.0313 ± 0.0007
	3	0.227 ± 0.052	0.131 ± 0.007		3	0.192 ± 0.078	0.135 ± 0.016
	4	0.317 ± 0.016	0.302 ± 0.036		4	0.350 ± 0.030	0.333 ± 0.046
	5	0.073 ± 0.021	1.27 ± 0.39		5	0.128 ± 0.027	1.36 ± 0.30
	6	0.023 ± 0.010	3.13 ± 1.00		6	0.029 ± 0.009	4.04 ± 1.16
^{235}U	1	0.038 ± 0.004	0.0127 ± 0.0003	^{241}Pu	1	0.010 ± 0.003	0.0128 ± 0.0002
	2	0.213 ± 0.007	0.0317 ± 0.0012		2	0.229 ± 0.006	0.0299 ± 0.0006
	3	0.188 ± 0.024	0.115 ± 0.004		3	0.173 ± 0.025	0.124 ± 0.013
	4	0.407 ± 0.010	0.311 ± 0.012		4	0.390 ± 0.050	0.352 ± 0.018
	5	0.128 ± 0.012	1.40 ± 0.12		5	0.182 ± 0.019	1.61 ± 0.15
	6	0.026 ± 0.004	3.87 ± 0.55		6	0.016 ± 0.005	3.47 ± 1.7
^{238}U	1	0.013 ± 0.001	0.0132 ± 0.0004	^{242}Pu	1	0.004 ± 0.001	0.0128 ± 0.0003
	2	0.137 ± 0.003	0.0321 ± 0.0009		2	0.195 ± 0.032	0.0314 ± 0.0013
	3	0.162 ± 0.030	0.139 ± 0.007		3	0.161 ± 0.048	0.128 ± 0.009
	4	0.388 ± 0.018	0.358 ± 0.021		4	0.412 ± 0.153	0.325 ± 0.020
	5	0.225 ± 0.019	1.41 ± 0.10		5	0.218 ± 0.087	1.35 ± 0.09
	6	0.075 ± 0.007	4.02 ± 0.32		6	0.010 ± 0.003	3.70 ± 0.44

In addition to prompt neutrons and delayed neutrons, gamma-rays emitted during the fission process can also be used as signature signals for SNM detection. However, when a photon source is used as the interrogation source, prompt γ-rays are buried by the much more intense probing radiation. Thus, it is almost impossible to use them for detection in photon interrogation techniques.

Alternatively, using delayed gamma rays instead of prompt gamma rays is more practical for detection. Delayed γ-rays are emitted seconds and minutes after the irradiation and are not affected by the probing radiation. They also may be more useful than the above mentioned delayed neutrons. The total energy carried out by delayed γ-rays per fission is about 6 to 8 MeV. The average energy of the delayed γ-rays is about 1 MeV. Thus, approximately 6 to 8 delayed γ-rays are emitted following each fission

process. This is over 100x times bigger than the yield of delayed neutrons (~0.007 – 0.05 per fission).

It is important to note that unique γ-ray intensity distributions exist for each fissionable isotope [43-44], thus these can be used to distinguish between the nuclear materials. The delayed γ-ray energy spectra are rich and complex, but it is possible to resolve individual lines with high resolution detectors. The relative amplitudes of certain lines (i.e. ^{97}Y and ^{89}Rb) vary significantly from nuclear isotope to isotope. Discrimination ratios of the order of 3 were observed between ^{235}U, ^{239}Pu and ^{238}U [44-45]. Some examples are shown in Table 2.2.

Table 2.2 Intensity ratios of the fission product gamma rays induced by 10 MeV Bremsstrahlung photons and measured between 13 ms and 100 ms after the irradiation

Fission Product	Gamma-ray energy (keV)	Intensity ratios			
		^{239}Pu	^{238}U	^{235}U	^{232}Th
^{138}Cs	1436.0	100.0	100.0	100.0	100.0
^{94}Sr	1428.3	136.4	235.7	186.8	171.3
^{136}I	1313.0	72.7	240.5	123.0	109.3
^{89}Rb	1248.2	13.1	85.4	92.7	228.0
^{90}Kr	1118.7	39.5	110.5	108.5	171.0
^{97}Y	1103.0	113.7	148.1	115.2	68.9
^{89}Rb	1031.9	66.5	116.4	135.9	265.1

Taking into account the information presented above, we devised an experiment with the intent of testing potential improvements in radiation detection technology targeting SNM.

2.2 Experimental Setup

In our experiment, a 9 MeV Varian LINAC was used as the interrogation photon source. The delayed γ-rays were measured minutes after the irradiation using both a NaI scintillator detector and an HPGe detector. A large number of fission products were identified based on energy and time information. The count rate of the high energy delayed γ-rays was also studied as a possible signature signal for SNM detection.

2.2.1 The Depleted Uranium Sample

The nuclear material sample that was used in this photofission experiment was a depleted uranium rod with a length of 9 cm and a diameter of 1 cm. The mass of the sample was measured to be 109 g. The density was calculated to be 14.8 g/cm^3, which is close to the density of uranium oxide (UO_2). Using a GM tube, the dose rate at 10 cm away from the sample was measured to be 0.1 mCi. The energy spectrum of the γ-rays naturally emitted by this DU rod measured by an HPGe detector is shown below in Figure 2.2.

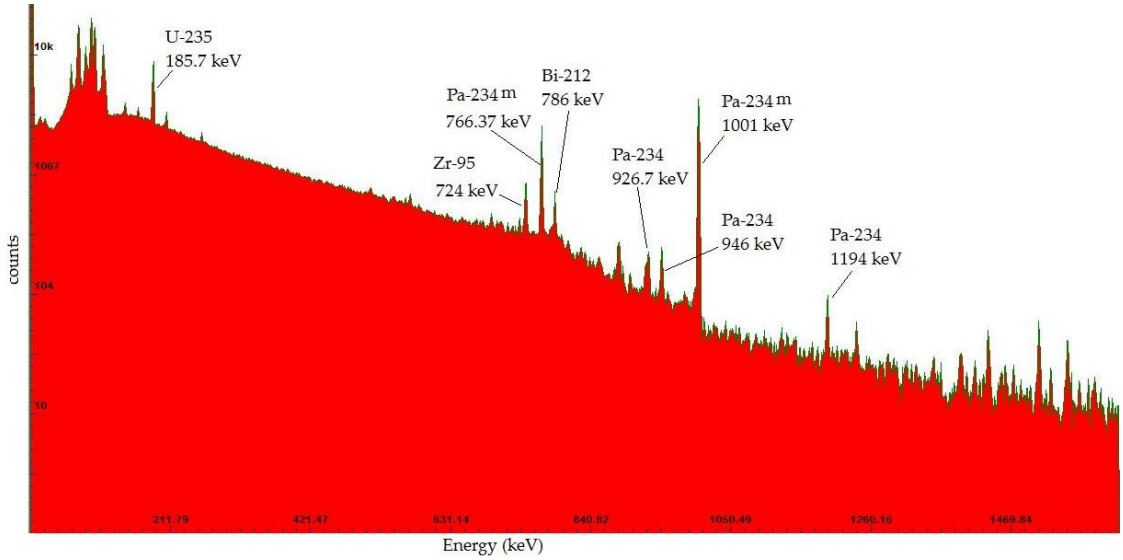

Figure 2.2 The energy spectrum of the γ-rays naturally emitted by the DU sample

2.2.2 Detectors Used in this Experiment

In this photofission experiment, both time and energy information were used to identify various fission products. Since the energy spectrum of the delayed γ-rays is quite rich and complicated, detectors with excellent energy resolution were required. An HPGe detector was used to extract energy information. The efficiency of this detector is a function of energy, so calibration is required before measurements. In addition to the difference in yields from isotope to isotope, the time behavior of the count rate of high energy delayed γ-rays is also an important signature for SNM detection and identification. Scintillator detectors with high detection efficiency but moderate energy resolution are suitable for this kind of application, because of their relatively low cost and sturdiness.

The HPGe detector used in this experiment has a size of 3” by 3”. It features a pop-top configuration and requires liquid nitrogen cooling. The crystal is fully depleted at

negative 3000 V. The result of the energy calibration using several radioactive isotopes is shown in Table 2.3. The energy resolution of this detector (~1% at 662 keV) is poor by HPGe standards, probably because of the long shelf time. But the resolution will be seen to be adequate to identify specific gamma ray peaks.

Table 2.3 Result of Energy Calibration of the HPGe Detector

Isotope	Gamma Energy (keV)	MCA Channel	Resolution (keV)
^{60}Co	1173.2	350.44	8.117
	1332.5	398.30	8.431
^{22}Na	511	150.74	5.981
	1274.6	379.41	7.741
^{54}Mn	834.83	247.73	5.891
^{137}Cs	661.64	195.81	5.145

The intrinsic detection efficiency of this detector was measured at several energies, using radioactive isotope sources. The results are shown below in Table 2.4.

Table 2.4 Intrinsic Peak Efficiency of the HPGe detector

Isotope	Gamma Energy (keV)	Intrinsic Peak Efficiency
^{22}Na	511	0.0356
	1274.6	0.0066
^{60}Co	1173.2	0.0074
	1332.5	0.0066
^{54}Mn	834.83	0.0138
^{137}Cs	661.64	0.0132
^{133}Ba	81	0.0668
	276.4	0.0220
	302.85	0.0258
	356	0.0220
	383.85	0.0298

A 3” by 3” NaI detector was also used in this experiment. The energy resolution of this detector is not fine enough to resolve the individual lines of delayed γ-rays. Therefore, the detector was used in the study of high energy delayed γ-rays count rate as a signature signal for SNM detection, where energy resolution is not an essential requirement. The result of the energy calibration is shown below in Figure 2.3. The detector functions normally and the response is quite linear from 100 keV up to 1.4 MeV.

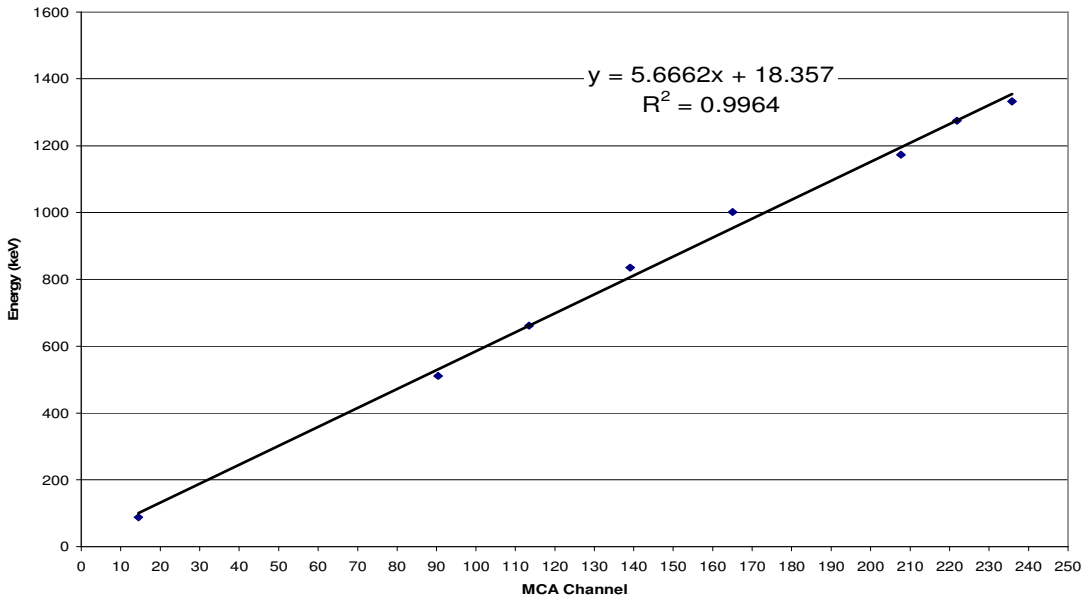

Figure 2.3 Energy Calibration of the NaI detector

2.2.3 LINAC and the Experimental Hall

The first photofission experiment was conducted at the Ford Non-Destructive Evaluation Facility in Livonia, MI. The facility is equipped with one CT unit and one real-time x-ray radiography system that was used in this experiment. It is a Varian Linatron 3000 unit with a 30 degree collimator built-in, shown in Figure 2.4.

Figure 2.4 The LINAC Used in this Experiment – Varian Linatron 3000

The radiography system together with the CT unit is located in an experimental hall built to contain all the radiation inside it such that the external dose rate is below the non-occupational limit of 1 mSv/yr. The drawing of this experimental hall is shown in Figure 2.5 [46].

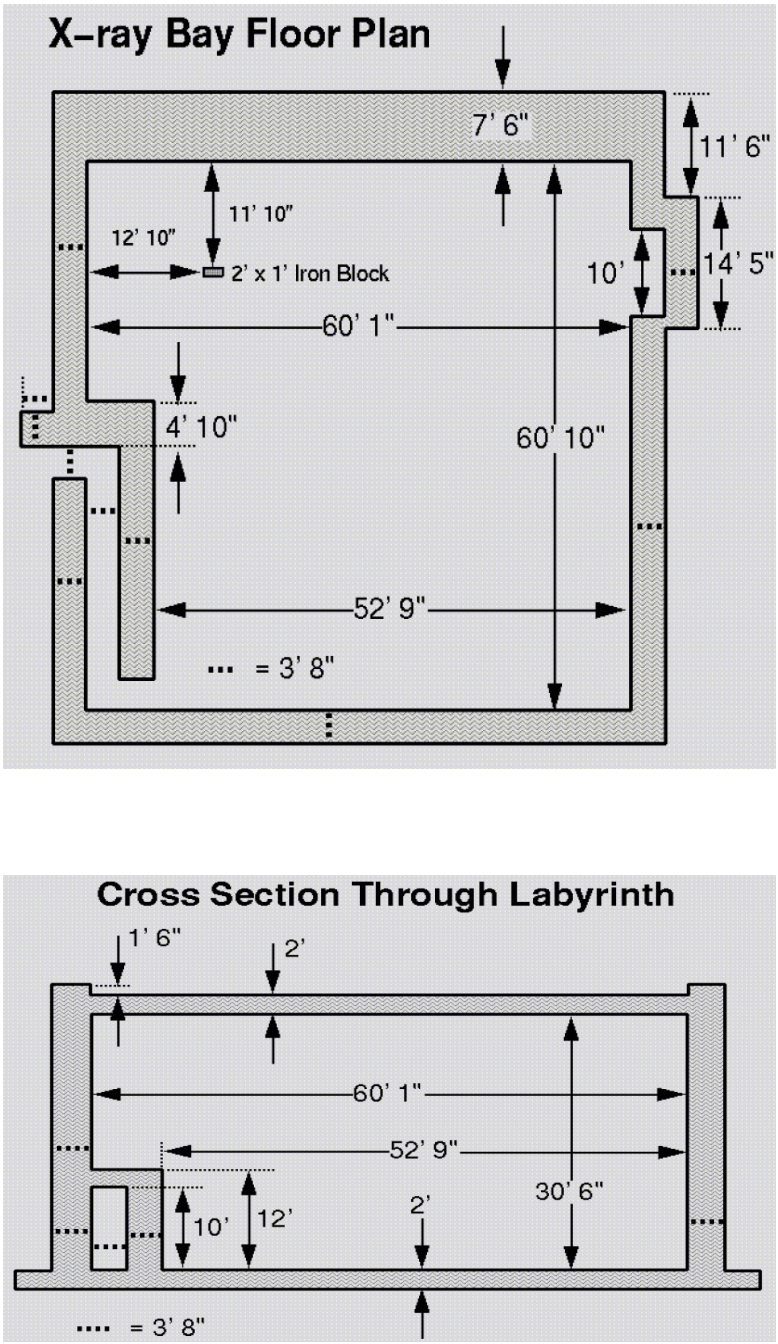

Figure 2.5 The Schematic Drawing of the Experimental Hall

In this experiment, the samples were irradiated inside the experimental hall and then taken into a counting room to be measured by the HPGe and NaI detectors. In each irradiation, the sample was located on the beam axis 25" away from the bremsstrahlung converter.

2.3 Predicted Photofission Reaction Rate

The expected photofission reaction rate in our ^{238}U cylindrical rod was estimated using an experimental measurement of the dose rate produced by Ford's 9-MeV LINAC and a simulation of the x-ray spectrum produced per 9 MeV electron using MCNP5 [47].

The calculated energy spectrum of the x-rays emerging from this LINAC is shown in Figure 2.6, which comes from an MCNP simulation, assuming no shielding around the target head. The material used as the bremsstrahlung converter is tungsten.

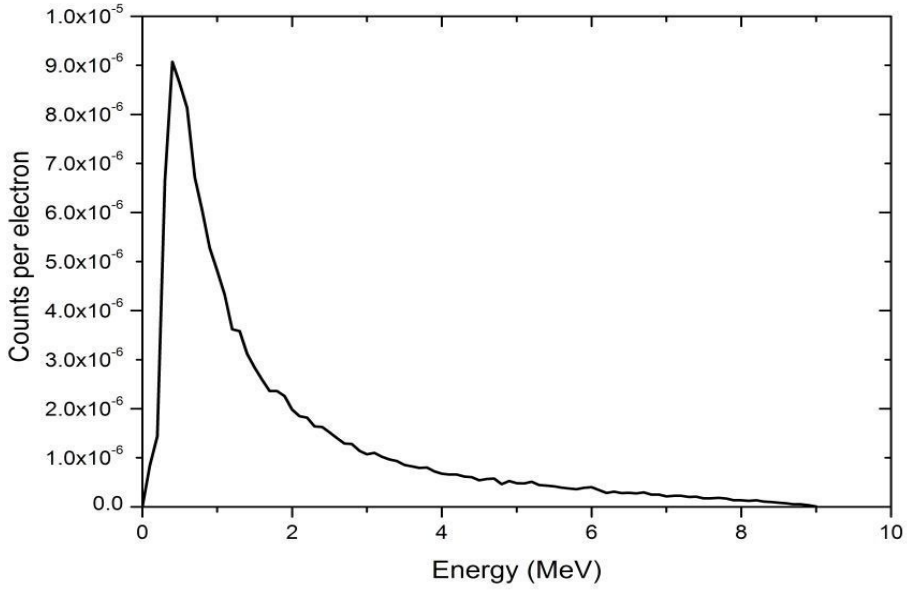

Figure 2.6 Calculated x-ray spectrum

In the simulation, a cell filled with dry air at STP was located 25 inches away from the bremsstrahlung converter on the beam axis. The x-ray energy deposited in this cell by each 9 MeV source electron was calculated to be 1.44×10^{-2} eV/cm^3. According to the definition of the exposure unit *roentgen* (R), the exposure caused by each source electron at this location is 2.03×10^{-13} R.

At the same position, the dose rate was measured, using a calibrated ion chamber, to be 1.56 Gy/s (177.27 R/s). The ratio of dose rate to the exposure caused by each source electron gives the effective current of the LINAC to be 139 μA (the LINAC works in pulse mode, with a duty cycle of 300 Hz and pulse duration of 5 μs). This is larger than the 50 μA reported on a similar machine [46]. Shielding around the target head was not included in the simulation and could account for some of this difference. These scattered photons should not be a significant factor when the sample is centered downstream in the beam. Since we are only interested in order-of-magnitude estimates, this level of agreement is acceptable.

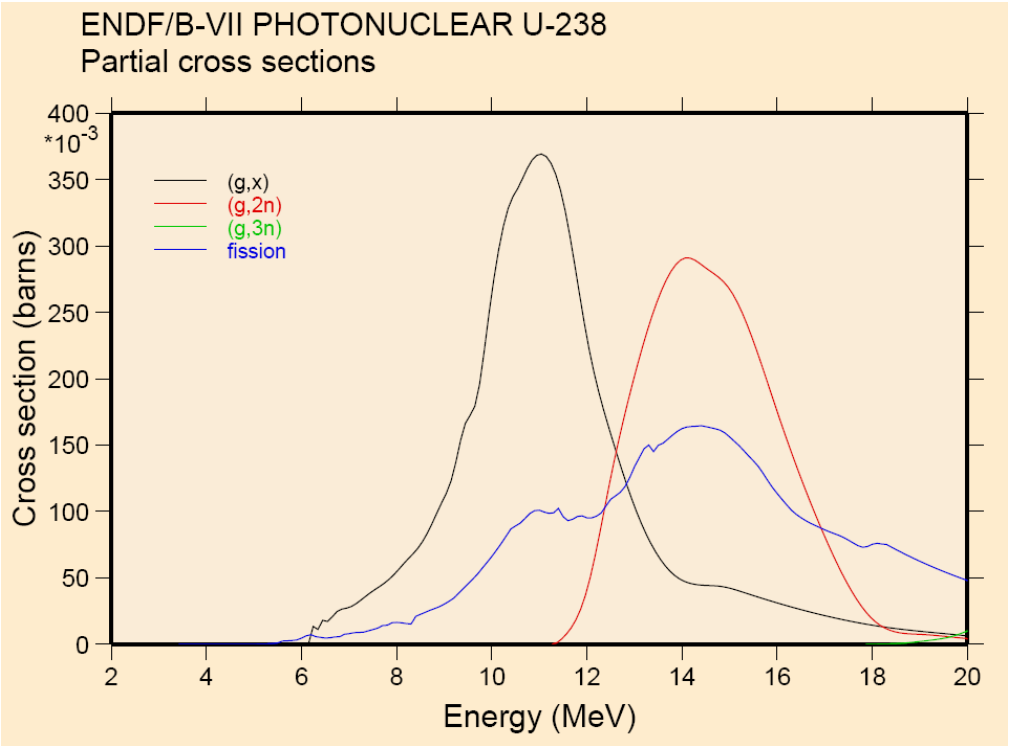

Figure 2.7 Partial photonuclear cross section for ^{238}U (photofission cross section shown as the blue curve) [48]

The energy dependent ^{238}U photofission cross section is shown in Figure 2.7. By integrating the product of the interrogating x-ray spectrum with the ^{238}U photofission cross section, and multiplying by the number of exposed ^{238}U nuclei, the expected photofission reaction rate from our sample, induced by Ford's LINAC, was estimated to be ~10^6-10^7 reactions per second.

2.4 Photon Irradiation and Energy Spectrum Analysis

The first part of our experiment was to induce fission in the sample by photon irradiation. The sample was placed on the axis of the x-ray beam at a distance of 63.5 cm (25") from the bremsstrahlung target. To remove any thermal neutrons that may have

originated from moderation of photoneutrons in surrounding materials, the sample was wrapped in a thick Cd sheet, with an opening facing the beam. The first experiment that was performed was a 5-minute irradiation of an Al sample to verify that no photoactivation was taking place in this common material. Since the photoneutron threshold is 13 MeV, the negligible induced activity dose rate of 50 μR/h was not unexpected. The second experiment performed was a 5-minute irradiation of a Pb sample (with photoneutron thresholds of 7-8 MeV) that yielded a similar negligible dose rate. The third run was a 12-second irradiation on our ^{238}U sample. The uranium rod was placed perpendicular to the axis of the beam, presenting a maximum thickness of 1 cm. In this case, a dose rate of 1.6 mR/h was induced with only a 12-second irradiation. An HPGe detector recorded the gamma ray spectrum from the photoactivation of the ^{238}U several minutes (386 seconds) later in a single measurement of 423 seconds. The 386 seconds delay included sample transportation time and sample cooling time. The isotopes that could be identified in the gamma spectrum are listed in Table 2.5 below. Note that the isotopes observed in this experiment have moderate to long half lives, since the activity of the short-lived fission products decreased to a very low level before the measurement actually began. Comparing to the results shown in Table 2.2, which was measured between 13 ms and 100 ms after the irradiation, we are missing the short-lived ^{97}Y (HL = 3.75 s) and ^{90}Kr (HL = 32.32 s). Later, we will show that ^{90}Kr was observed in the following experiment, in Table 2.7.

Table 2.5 Observed Photofission Products from ^{238}U Irradiation

Isotope	Half Life (min)
^{89}Rb	15.2
^{94}Sr	1.25
^{94}Y	18.7
^{104}Tc	18.3
^{131}Sb	23.03
^{132}Sb	2.8
^{132m}Sb	4.1
^{133}Sb	2.5
^{134}Te	41.8
^{135}I	394.2
^{136}I	1.39
^{138}Xe	14.1
^{138}Cs	2.9
^{142}Ba	10.6
^{145}Ce	3.01

From the net counts of gamma rays emitted by selected isotopes, the photofission reaction rate was estimated as described below.

Assuming N_{pp} is the number of atoms of this isotope produced during each pulse, and that the atoms appear instantaneously at the beginning of the pulse (Since the isotopes are produced during the first 5 μs of the ~3 ms pulse, this is a reasonable approximation), the number of counts under the photopeak contributed by the i^{th} pulse is given by:

$$C_i = \varepsilon \eta N_{pp} (e^{-\lambda(t_i-(i-1)\tau)}) e^{-\lambda t_w} (1 - e^{-\lambda t_c})$$

where τ is the period of the pulse (1/300 s), η is the branching ratio of the measured photo peak, ε is the absolute peak efficiency of the HPGe detector, λ is the

decay constant of this isotope, t_i is the length of the irradiation, t_w is the time delay between irradiation and counting, and t_c is the counting time. Performing the finite sum over the number of pulses yields:

$$C = \sum_{i=1}^{t_i/\tau} C_i = \varepsilon\eta N_{pp}\left(\frac{(1-e^{-\lambda t_i})e^{-\lambda t_w}(1-e^{-\lambda t_c})}{e^{\lambda\tau}-1}\right)$$

The photofission rate R is given by:

$$R = \frac{N_{pp}}{Y\tau}$$

where Y is the yield fraction of this isotope from a photofission. Solving this latter equation for N_{pp} and substituting into the previous expression yields the desired result:

$$R \cong \frac{C}{\eta\varepsilon\tau Y}\left(\frac{e^{\lambda\tau}-1}{(1-e^{-\lambda t_i})\cdot e^{-\lambda t_w}(1-e^{-\lambda t_c})}\right)$$

Because ^{238}U photofission yields are not complete, the values were approximated by the neutron-induced fission product yields in the calculation of reaction rate.

The photofission rates inferred from several observed isotopes are shown in Table 2.6. The agreement between the measurement results and the 10^6-10^7 s^{-1} reaction rate predicted above by the MCNP simulation is acceptable, since we are interested in ascertaining the practicality of this approach.

Table 2.6 Measured ^{238}U Photofission Reaction Rate

Property	710 keV (^{93}Sr)	974 keV (^{132}Sb)	696 keV (^{132m}Sb)	696 keV (^{132}Sb)	1248 keV (^{89}Rb)	1096 keV (^{133}Sb)	817 keV (^{133}Sb)
Half Life(min)	7.4	4.2	2.8	4.2	15.2	2.5	2.5
Branch ratio	0.206	0.989	0.86	0.989	0.426	0.32	0.138
Abs. Peak Eff.	0.006	0.005	0.0065	0.0065	0.003	0.003	0.006
Measured counts	2447	5476	7218	7218	2390	1904	1733
Reaction rate × Yield (/sec)	6.178E+05	3.817E+05	6.252E+05	3.870E+05	7.566E+05	1.115E+06	1.176E+06
Cumulative Yield	0.045	0.0131	0.0189	0.0131	0.0292	0.0243	0.0243
reaction rate (gammas/sec)	1.373E+07	2.914E+07	3.308E+07	2.954E+07	2.591E+07	4.587E+07	4.840E+07

Spectra taken at various times can be very helpful when trying to identify fission products, given that the half lives of possible isotopes are well known. In the second irradiation, the sample was exposed to the beam for 24 seconds. After a 37-second transport delay, the exposed ^{238}U sample was placed on the 3” by 3” coaxial HPGe detector. A maximum counting rate of 3000 counts per second was measured. Instead of a single long spectroscopic measurement, a sequence of 3-second measurements were taken. Figure 2.8 shows three consecutive spectra from this sequence of measurements.

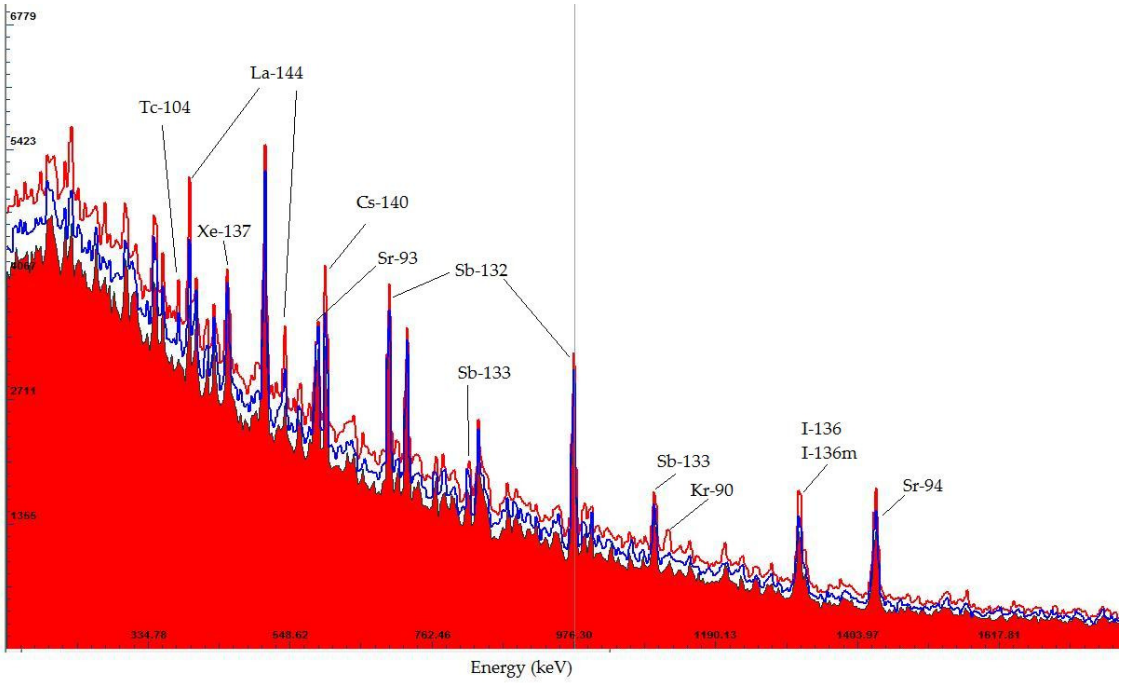

Figure 2.8 Spectra generated in the sequence of 3-second measurements

Using the time information gained by this method, and because the series of measurements started earlier than the previous measurement, some additional fission products were observed, shown in Table 2.7. Most of them have relatively short half lives.

Table 2.7 Additional Measured Fission Products from ^{238}U Photofission

Isotope	Half Life (min)
^{90}Kr	0.54
^{93}Sr	7.42
^{104}Tc	18.3
^{136}I	1.39
^{136m}I	0.78
^{137}Xe	3.82
^{139}Xe	0.66
^{140}Cs	1.06
^{144}La	0.68

2.5 Estimated Production Rate of High Energy Gamma Rays

An estimation of the production rate of high energy (> 3 MeV) gamma rays was also calculated. These are particularly interesting because in this high energy region, natural background is negligible. These gamma rays can more readily penetrate most shield materials that could be used to conceal the nuclear material. Without data on fission product yields from ^{238}U photofission, we used fission product yields from neutron-induced fission from LBL Nuclear Science Division's "Isotope Explorer", 2003. (For photofission, it is the ^{238}U nucleus that fissions, whereas the ^{239}U nucleus fissions in the neutron induced case). There were 253 fission products found with cumulative yields greater than 0.1 % per fission, and with half-lives less than 10 minutes. Of those, there were 59 nuclides that produced reportable γ-ray intensities at energies above 3 MeV. The most intense of these emitters are listed in Table 2.8 [49].

Table 2.8 Neutron-induced fission products of ^{238}U that emit high-energy gamma rays

Nuclide	Half-life (sec)	> 4 MeV gamma rays per fission	> 3 MeV gamma rays per fission	Cumulative Yield per fission
^{85}Se	39	0	0.0012	0.005
^{87}Br	55.9	0.0034	0.0056	0.0155
^{88}Br	16.4	0.0037	0.006	0.0149
^{89}Br	4.4	0.0021	0.0029	0.015
^{89}Kr	189	0.0004	0.0018	0.0281
^{90}Br	1.9	0.00057	0.0014	0.0104
^{90m}Rb	258	0.00035	0.002	0.00688
^{91}Kr	8.6	0.000035	0.0015	0.0252
^{91}Rb	58	0.0035	0.0115	0.038
^{92}Rb	4.5	0.00084	0.0091	0.0357
^{93}Rb	5.9	0.00075	0.007	0.034
^{94}Rb	2.7	0.00036	0.0024	0.0276
^{95}Rb	0.38	0.000053	0.0021	0.0151
^{95}Sr	25.1	0.00042	0.0025	0.0428
^{97}Y	3.8	0	0.017	0.0493
^{106}Tc	36	0	0.004	0.0245
^{128}In	0.8	0.0008	0.0024	0.0057
^{136}Te	17.5	0	0.0022	0.0144
^{140}Cs	63.6	0	0.003	0.0447
^{141}Cs	24.9	0	0.0016	0.0385
^{142}Cs	1.8	0.00058	0.0015	0.0288

Using the calculated ^{238}U photofission rate above and the yields of those neutron-induced fission products having gamma energies above 3 MeV, one can estimate the production rate (i.e., saturated activity) of high energy (>3 MeV) gamma rays using $A_{j>3MeV} = R * \sum_{i=1}^{N} \sum_{j>3MeV}^{\infty} Y_i * f_{ij}$, where R is the reaction rate, Y_i is the yield of isotope i, and f_{ij} is the branching ratio of isotope i to produce energy j. From these values, we predict a

saturated activity of 7×10^4 gammas per second for our sample or 600 delayed high-energy gamma rays per second per gram of sample exposed. This equals to 3.82 high-energy gammas per second per square centimeter at 5 m from a 20 kg chunk of DU. An emission rate approaching this value can be achieved with an exposure time of a few effective half-lives.

2.6 Count Rate of High Energy Gamma Rays

In their work, researchers from LBNL proposed a method to detect hidden SNM that can provide much higher sensitivity than passive methods and methods based on delayed neutron detection [31]. The method is based on the relatively high intensity of γ-rays with energy greater than 3 MeV emitted by short-lived fission fragments. These delayed γ-rays have yields that are roughly an order of magnitude bigger than the yields of delayed neutrons. Because of their relatively high energies, they are more likely to penetrate thick hydrogenous materials with a possibility 10^2 ~ 10^3 times bigger than that for delayed neutrons. Thus, this method is 10^3 ~ 10^4 times more sensitive than the methods based on delayed neutrons detection. Instead of studying yields of individual fission products as presented in previous section, they asserted that high count rate of high energy delayed γ-rays is an important signature of SNM.

The time dependence of the emission of these delayed γ-rays also provides unique signatures for different isotopes. The delayed γ-rays decay much slower compared to delayed neutrons. Delayed γ-ray activities from ^{235}U and ^{239}Pu have been studied. The temporal behavior varies from isotope to isotope, but not as significantly as is the case for

delayed neutrons. The ratio of the delayed γ-rays intensity at early times to that at later times can also be used as signature for isotope identification [50].

The work described in this section follows the approach used at LBNL. Instead of using thermal neutrons as interrogating radiation, high energy x-rays were used to induce fission in a DU sample. Both HPGe and NaI detectors were used in our experiments, because it would be far easier to use a scintillator in the envisioned practical setting. The goal of our work was to see whether the enhanced efficiency at higher energies of a NaI detector could be useful despite the loss of energy resolution.

In order to study the detection technique based on high energy gamma counting, we performed a series of experiments using a ^{238}U sample. The ^{238}U sample was first exposed for 24 seconds. After a 37-second transport delay, the exposed ^{238}U sample was placed on our 3 inch by 3 inch coaxial HPGe. A maximum counting rate of 3000 counts per second was measured. A sequence of 3-second measurements followed, and yielded an average half-life of ~80 seconds, shown in Figure 2.9.

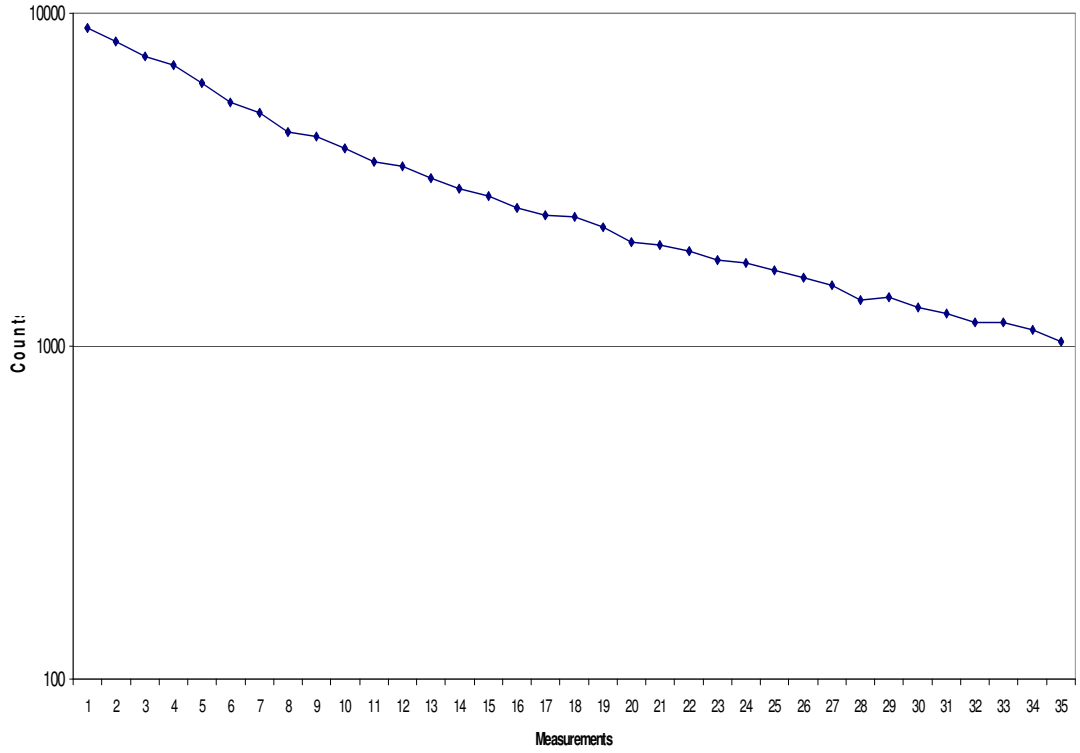

Figure 2.9 Delayed Gamma Ray (E > 3MeV) Count Rate of as a Function of Time Measured by the HPGe Detector

After ensuring the sample had decayed to background levels, the ^{238}U sample was again exposed for 24 seconds. After a 40-second transport delay, the sample was placed on a 5.08 cm (2") tall spacer above a standard 7.62 cm (3") by 7.62 cm (3") NaI(Tl)/PMT detector. A maximum counting rate of 3376 counts per second was observed. The average half-life was determined to be 75 seconds, shown in Figure 2.10. After scaling for distance, one can expect a counting rate of 12.5 cps from the high-energy gamma rays at 1 m from the same sample, using the same detector and after the same irradiation. For comparison, under the same conditions, the background (DU rod before irradiation plus ambient background) was measured to be 0.7 cps.

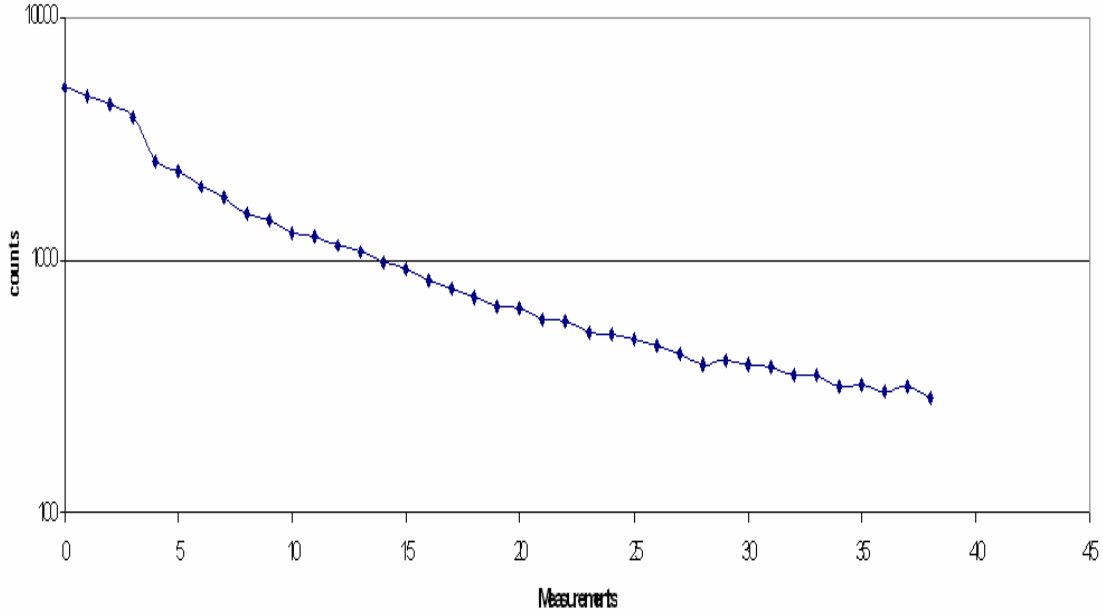

Figure 2.10 Delayed Gamma Ray (E > 3MeV) Count Rate of as a Function of Time Measured by NaI Detector

The decay constants of the high-energy gamma-ray count rate measured in these experiments are much longer than those from ^{235}U and ^{239}Pu reported in Norman and Prussin's paper (~25 s). This difference might stem from the difference in the starting point of measurements (the measurements at LLNL started 3 s after the end of irradiation) or the difference between the nature of photon induced fission and neutron induced fission.

No distinct structure was observed in the spectra above 3 MeV, even from the HPGe detector. The spectra acquired by the NaI(Tl) and HPGe detectors are compared in Figure 2.11. Lacking a calibration source near this energy, we extrapolated our energy calibrations to estimate the 3 MeV lower setpoint. For the HPGe detector, spectra are

shown for both before and after irradiation. The pre-irradiation count rates are scaled up by a factor of 20 in order to be visible on the same graph with the post-irradiation spectrum. The difference in the two spectra clearly indicates the occurrence of photofission, as predicted.

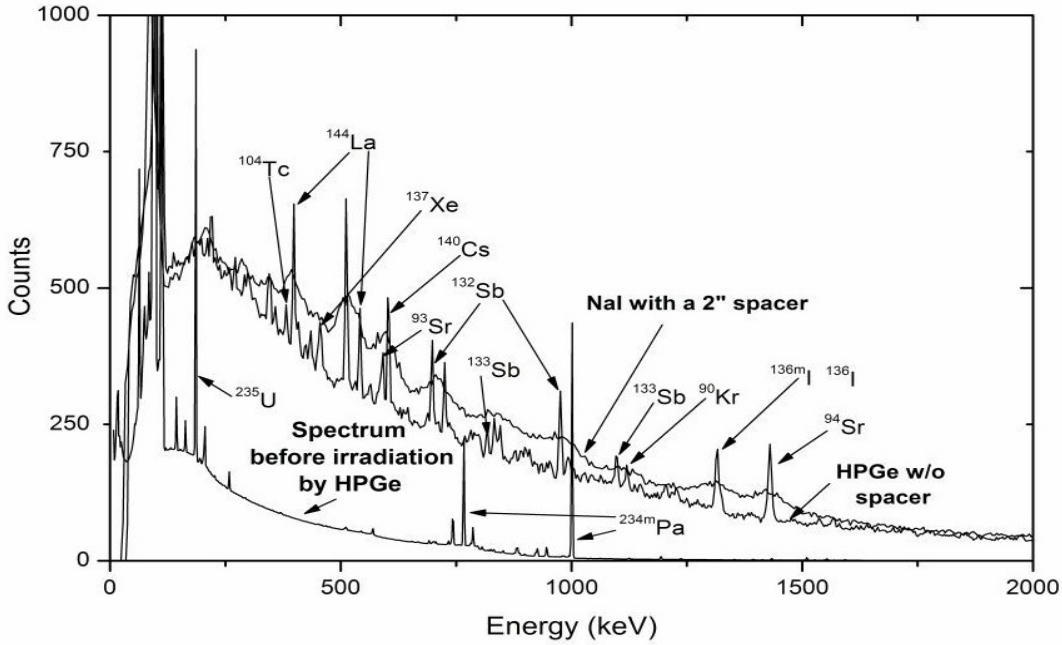

Figure 2.11 Comparison between spectra taken by HPGe and NaI(Tl) detectors

The relative number of NaI(Tl) counts is less than what might be expected on the basis of intrinsic efficiency because of the increased counting distance. Because of the small energy separation between photopeaks, the spectrum from NaI(Tl) does not provide particularly useful information on specific fission products. For the proposed application, however, the spectrum is not required. Furthermore, since there are no identifiable energy peaks shown above 3 MeV even on the HPGe-measured spectrum, the NaI(Tl) detector

may be preferable due to its higher detection efficiency, portability, and relatively low cost.

An efficiency-corrected ratio of the 186 keV to the 1001 keV counts gives a ^{235}U fraction of 0.07%. Because the 186 keV line undergoes significant self-absorption, the enrichment could actually be higher. This leads us to believe that the sample is depleted uranium.

2.7 Delayed Gamma Rays Measured Between Interrogation Pulses

The rate of delayed gamma rays emitted by photofission products is time-dependent ($\sim t^{-1.2}$) and decreases rapidly after the irradiation. In order to increase the detection sensitivity, measurements of delayed gamma rays should start as close as possible to the end of the irradiation that induces fission in the sample. Instead of measuring the delayed gamma rays after the irradiation (as presented in previous sections) the detection sensitivity can be dramatically increased by performing a measurement after each accelerator pulse.

The LINAC used in this study was the same one as described in section 2.2.3 at the Ford NDE facility located in Livonia, MI. The detector used in this series of measurements was a 90% efficient HPGe detector (ORTEC GEM90). Both customized and commercial electronics were tested in the experiments. The experimental setup and measurement system are shown below in Figure 2.12.

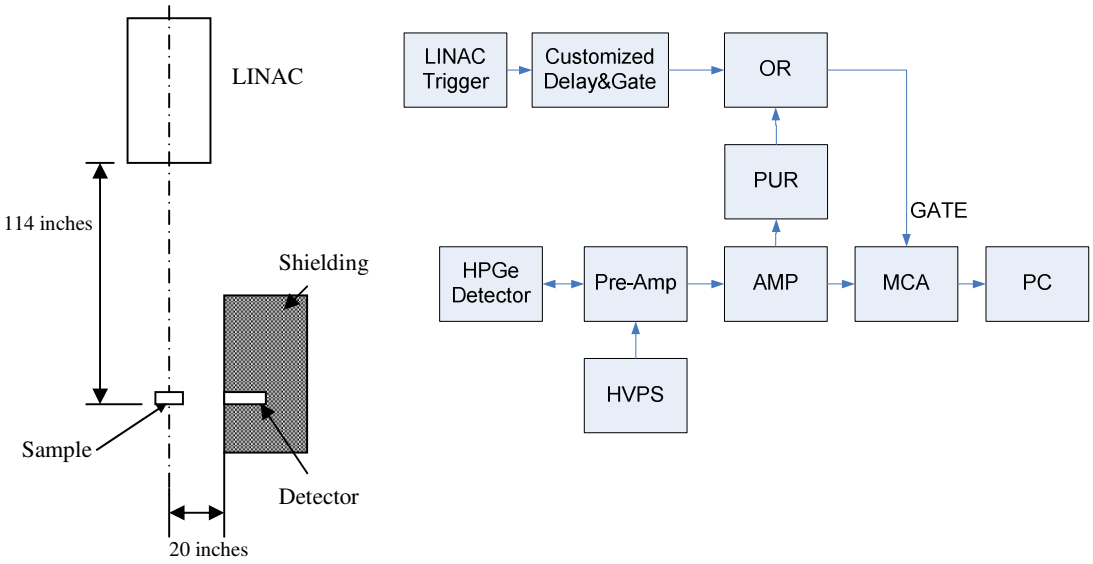

Figure 2.12 Experimental setup and system schematic

In these experiments, the LINAC was running at 50 Hz. The time duration between two adjacent pulses is thus 20 ms. The width of each pulse is 5 μs. The MCA used in this study (ORTEC 926) has a GATE input. Based on the polarity of the GATE signal, the input signals can be rejected (high) or allowed (low) into the MCA. A customized delay and gate circuit was built. It can generate pulses with variable lengths and delays that are synchronized to an input trigger signal. During the measurements, both the pile-up rejection (PUR) output from the amplifier and the output from the customized delay and gate circuit were used to generate the GATE input to the MCA through an 'OR' logic unit. By doing this, we can adjust the starting point and duration of the measurements while keeping the spectroscopy system constant. Further study showed that within 6 ms after the LINAC trigger signal, the PUR output of the amplifier was always active. This implies that the high count rate in this time period prevented the amplifier from functioning properly in our setup. Thus, all the measurements following

started 6 ms after the trigger signal and lasted 14 ms until the next pulse arrived. The timeline for these measurements is shown below in Figure 2.13.

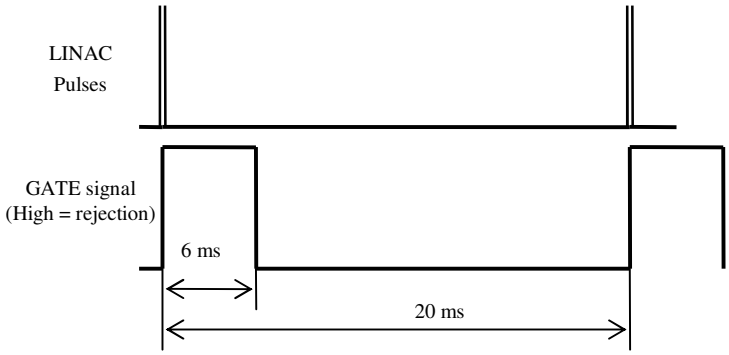

Figure 2.13 Timeline of the measurement

Two spectra were taken with the same irradiation and geometry, one with a DU sample in the beam and one without. The active background acquired when the beam was on but no sample was present, is shown below in Figure 2.14. The spectrum is fairly rich, even when nothing is present in the beam. The resolution of the detector degrades because of the high count rate. It's almost impossible to identify the lines solely based on the energy information.

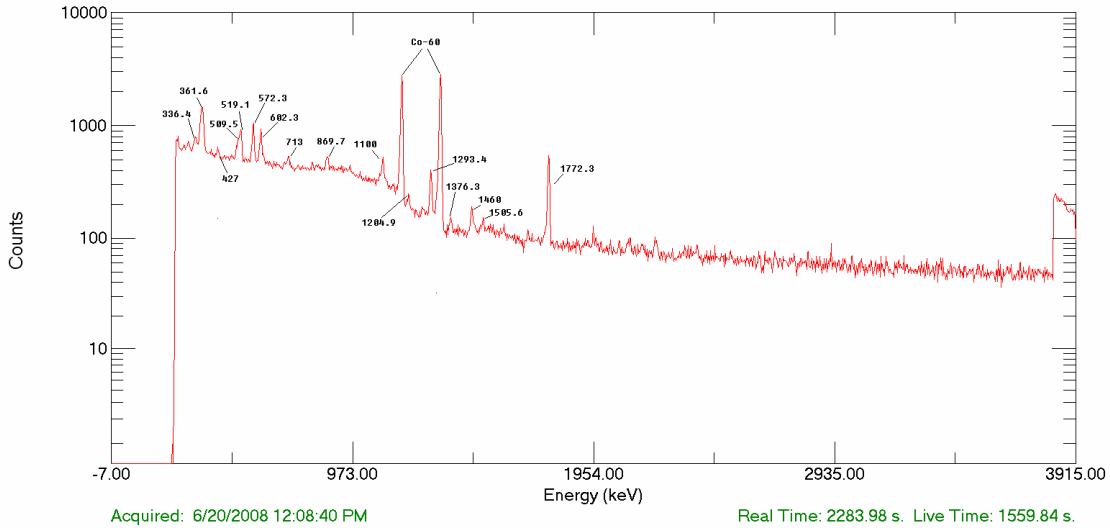

Figure 2.14 Active background measured with the HPGe detector (Energies are in keV)

The DU sample used in this experiment was a 3 inch by 3 inch by 1 inch block. Using the same method described in section 2.3, the induced fission rate in this sample was estimated to be 1.3×10^{5} reactions per second. The floor design of the experimental hall makes it impossible for us to put the detector and shielding closer than 114 inches to the LINAC head. This distance greatly decreased the photon flux at the sample position and hence greatly decreased the photofission reaction rate. Further, in order to keep the detector from getting saturated by the direct beam and the scattered radiation, a 1 inch thick Pb plate was placed in front of the detector. This lowered the detection efficiency of the delayed gamma rays. The spectrum taken with the DU sample in the beam is shown below in Figure 2.15. No major difference was observed except the expected 1.001 MeV peak from U-238 decay. However, a closer look in the energy range of 1.3 MeV to 1.6 MeV clearly shows the presence of fission products: Cs-138 and Sr-94, shown in Figure 2.16. Similar results have been reported by Hollas [39]. The two peaks are very close to each other. The total net count rate under the peaks is 0.33 cps. Comparing to Table 2.2, the less intense peaks are missing in the spectrum because of the low detection efficiency in this experimental setup. The I-136 peak at 1313 keV has similar intensity as the 1428 keV Sr-94, but it is buried by the nearby 1333 keV peak from the Co-60 calibration source.

The background counting rate produced by the tail of the pulse, when combined with the fast decay fission products and de-excitation radiation emitted by the excited nuclei, can easily saturate the electronics system even at several milliseconds after the irradiation pulse. This study showed that the closest we could get to the end of the pulse

and have the detector function normally was 6 ms. But in Chapter 3, we will present approaches that allow data acquisition to occur much closer to the end of the pulse.

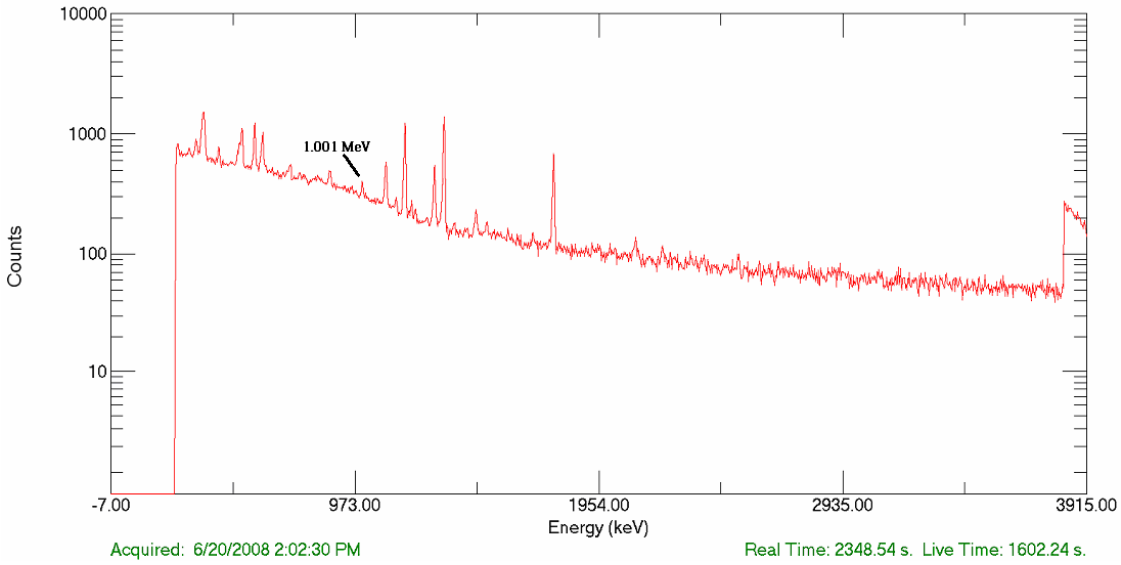

Figure 2.15 A delayed gamma spectrum measured in between interrogation pulses

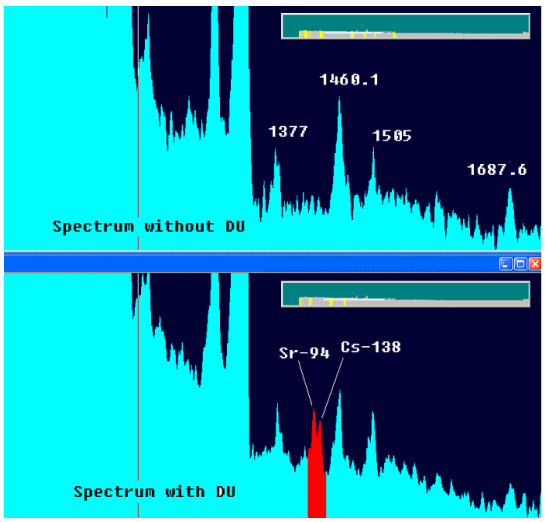

Figure 2.16 Comparison of spectrum taken with and without DU sample (Energies in keV)

2.8 Conclusions, Limitation and Further Work

In this work, detection techniques based on photofission were studied. Photofission in ^{238}U was observed. It was shown that delayed gamma rays from fission products can be observed well after the photon irradiation, thereby avoiding complications of trying to observe fission product emissions between beam pulses with a heavily shielded detector. Both the energy distribution and temporal behavior of the delayed gamma rays were proven to be appropriate signature signals for SNM detection.

Delayed gamma rays emitted by fission products were also measured using an HPGe detector between interrogation pulses. The tremendous count rate during the interrogation pulses could easily paralyze the detector even heavily shielded. Study showed that the detector couldn't function properly until 6 ms after the pulse. Thus, a very low repetition rate (50 Hz) was chosen during the experiments. Further, the floor design of the experimental hall limited the minimum distance between the DU sample and the LINAC head to 114". These two factors, being low repetition rate and long distance between LINAC head and DU sample, greatly decreased the photofission rate induced in the sample. As a result, not many delayed gamma peaks were observed from the measurement. However, fission products Cs-138 and Sr-94 were identified, which was confirmed by other researchers' work. It is believed that a shorter source-to-sample distance will greatly increase the photofission rate and provide more information on the fast decay delayed gamma rays.

Table 2.9 summarizes the isotopes that were observed in all of our photofission experiments described in this Chapter. Compared to Table 2.2, isotopes with moderate to long half-lives were all observed in our measurements. The only exception is ^{90}Y, which

has a fairly short half-life (3.75 s). The last experiment was designed to measure relatively short-lived photofission products, where data was taken between LINAC pulses. However, the detection efficiency was limited by the geometrical configuration of the room. Thus only the most intense fission products (e.g., ^{94}Sr) were observed. Some of the intense fission products are missing due to the degraded energy resolution at high count rate (i.e. ^{136}I).

Table 2.9 Observed U-238 Photofission Products by Delayed Gamma Rays

Isotope	**Main Emission Energy (keV)**	**$T_{1/2}$ (min)**	**Experimental methods**		
			Long Delay (Section 2.4)	**Short Delay (Section 2.4)**	**Measured Between Pulses (Section 2.7)**
^{89}Rb	1031.9	15.2	x	x	
^{89}Rb	1248.2	15.2	x	x	
^{94}Sr	1428.3	1.25	x	x	
^{94}Y	918.4	18.7	x	x	
^{104}Tc	358.0	18.3	x	x	
^{131}Sb	933.1	23.03	x	x	
^{132}Sb	973.9	2.8	x	x	
^{132m}Sb	973.9	4.1	x	x	
^{132m}Sb	696.8	4.1	x	x	
^{133}Sb	1096.22	2.5	x	x	
^{134}Te	767.2	41.8	x	x	
^{135}I	1260.4	394.2	x	x	
^{136}I	1313.0	1.39	x	x	
^{138}Xe	434.56	14.1	x	x	
^{138}Cs	1436.0	2.9	x	x	x
^{142}Ba	1204.3	10.6	x	x	
^{145}Ce	724.3	3.01	x	x	
^{90}Kr	1118.7	0.54		x	
^{93}Sr	590.2	7.42		x	
^{104}Tc	358.0	18.3		x	
^{136}I	1313.0	1.39		x	
^{136m}I	1313.0	0.78		x	
^{137}Xe	455.5	3.82		x	
^{139}Xe	218.6	0.66		x	
^{140}Cs	602.4	1.06		x	
^{144}La	541.2	0.68		x	
^{94}Sr	1428.3	1.25			x

No significant induced activity on Al, Pb, or Fe samples was observed. However, not all common materials that might be expected in practice have been thoroughly explored. Possible activation or fission from photoneutrons released from materials such as deuterium (2.22 MeV threshold) or carbon (4.95 MeV threshold for ^{13}C) has not been considered. Since these accelerators are routinely being used in the field for inspection, it is assumed that these are not significant. Another area requiring further examination is whether the count rates are adequate for practical settings and whether it would be more advantageous to look for specific radioisotopes or specific energy windows. Manipulating the time evolution of the fission product activity using multiple exposures could be examined. Finally, in Chapter 3, we introduce a faster readout system that can handle the high count rates that are present between interrogating pulses, tested a system on the photofission problem (cf. Section 3.2.4), and further development is a logical next step to gain more fission product data. Of course, the extension of this work to fissile isotopes is of contemporary interest.

CHAPTER 3

Development of Digital Spectroscopic Measurement Systems

3.1 Introduction

Accelerators are widely used as photon and/or neutron sources in active interrogation applications. Most of these machines work in pulse mode, producing pulses that are microseconds long with repetition rates of several hundred Hz. On the other hand, conventional analog spectroscopic measurement systems usually have dead times of the order of microseconds following each detected event. If the interesting events happen shortly after the pulsed radiation, conventional detection systems will probably miss most of them, owing to the long dead time following each measured event, as shown in Figure 3.1. Because of this, current systems usually start measurements following a certain delay time. For example, French Atomic Energy Commission researchers used high-energy photon interrogation to stimulate photofission and measured the delayed neutron and gamma-ray events after 60 s waiting time [51-52]. Researchers at Idaho National Laboratory, LANL, and Applied Research and Applications Corporation (ARACOR) identified shielded SNM by studying delayed neutron emission from photofission after waiting 2 ms following each pulse [20-22]. This was also shown in Section 2.7 where 6 ms was the minimum delay that we could tolerate. Because the intensity of the signature signals falls rapidly after the interrogation pulse, it is beneficial

to start the measurement as soon as possible following an irradiation pulse. When measuring signature signals during an irradiation beam, a long dead time puts a limit on the maximum counting rate that can be processed by conventional systems. For example, NRF scattering experiments are restricted to low current mode accelerators because of the extremely high event rates [53].

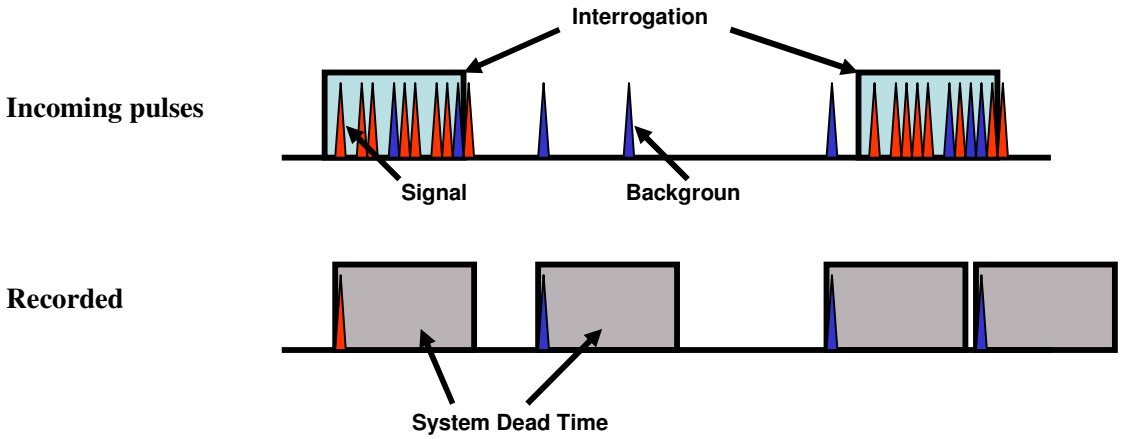

Figure 3.1 Signal Losses Due To System Dead Time

Thus, spectroscopic measurement systems that can handle higher count rates without sacrificing energy resolution are highly desirable for active interrogation studies. In the present work, two digital spectroscopy systems are presented. Their ability to deal with high rate events is demonstrated with photofission and NRF experiments.

In the first system, the signal from a PMT is directly digitized and then processed on a PC, using a deconvolution method. By bypassing the preamplifier, this system can handle extremely high count rates with only a minor sacrifice in energy resolution (5%

energy resolution at 1.33 MeV for a $LaCl_3$ detector at a count rate of 10^6 cps with no dead time, as compared with 10% energy resolution and 90% dead time achieved with an analog system under the same conditions). Using this system, delayed gamma rays from photofission products can be measured between interrogation pulses using a $LaCl_3$ detector for the first time. This dramatically increases the sensitivity of the photofission technique and decreases the required detection time. This could never be done with an analog spectroscopic system because of its long dead time (of the order of microseconds). A second system was developed which uses a fast ADC (125 MSPS) and an FPGA. In addition to the merits of the first system, real-time digital signal processing (DSP) is implemented on the FPGA chip. An energy spectrum is generated simultaneously during the measurement and stored in the memory available on the FPGA board. This reduces the amount of data which needs to be transferred to the PC, thus eliminating the requirement of a fast interface between the spectroscopic system and the PC.

3.2 Digitize and Transfer Approach

The ultimate goal is to record spectral measurements from a fast scintillator mounted on a PMT during the interrogation pulse from a pulse mode LINAC or shortly thereafter. The simplest approach is to digitize the signal at its source and transfer it to the PC for signal processing.

After being triggered by a signal from a LINAC X-ray pulse, a fast digitizer recorded the output signal from the PMT directly. The digitized waveform was transferred to a PC through the PCI interface, and signal processing was performed by the PC during the quiescent time between interrogation pulses.

3.2.1 Overview of the Hardware

The digitizer tested in this system is a commercially available product from National Instruments (NI). Hardware specifications are listed in Table 3.1, and the card is shown in Figure 3.2.

Table 3.1 Specifications of the NI PCI-5124

Terms	Specifications
Number of Channels	2
Sampling rate	200 MHz
Resolution	12-bit
Onboard Memory	8 MB
Interface	PCI Bus
Triggering	Either input channel, external

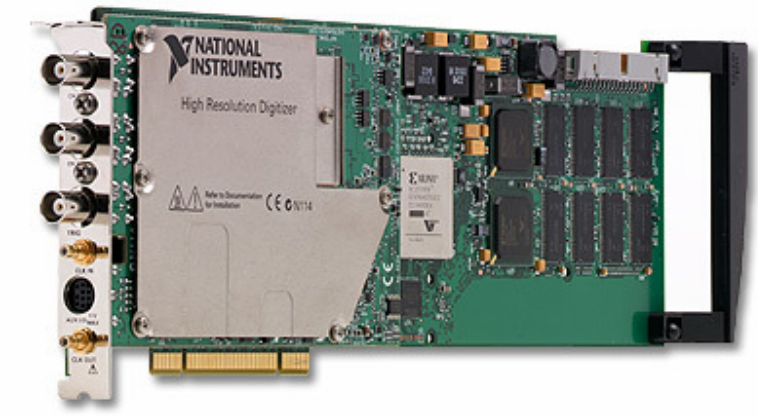

Figure 3.2 National Instruments Digitizer PCI-5124

Most inorganic scintillation detectors have decay times ranging from several tens of nanoseconds to several hundred nanoseconds. In our case, a fast $LaCl_3$ detector (28 ns decay time) was used together with this spectroscopic system. The 200 MHz sampling rate is fast enough to capture the waveform, as shown in Figure 3.3. The input impedance of the digitizer is 50 Ω. The $LaCl_3$ detector has an energy resolution of 2.9% at 1.33 MeV, as measured by an analog spectroscopic system at 1000 cps. A 12-bit resolution is enough to accurately reflect this kind of performance (1/4069 = 0.02%). Owing to the lack of signal processing capability in the digitizer, the entire waveform needs to be transferred to a PC for subsequent processing.

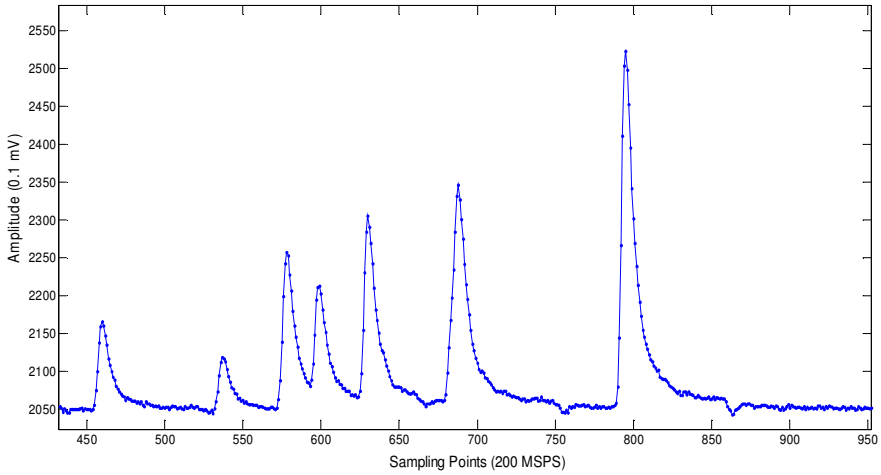

Figure 3.3 Digitized output signal from a PMT connected to a $LaCl_3$ scintillator.

The interface between the digitizer and the PC is the PCI bus. With a maximum transfer rate of 33 MHz and a capacity of 32-bits, the PCI bus (132 MB/s) cannot keep up with the data flow at the input channels. In addition, the latency during the writing to the PC hard drive further decreases the data transfer rate. National Instruments provides a

fast onboard acquisition memory for temporary data storage, but the size of this memory limits the maximum continuous acquisition time.

A LabVIEW program was developed to operate the digitizer and control data transfer between the DAQ card and the PC. The user interface is shown below in Figure 3.4. Through this interface, various parameters can be set, including sampling rate, triggering source and mode, length of the data recorded, input impedance, input range, etc. The program is based on the set of commands from National Instruments Virtual Instruments called NI-SCOPE.

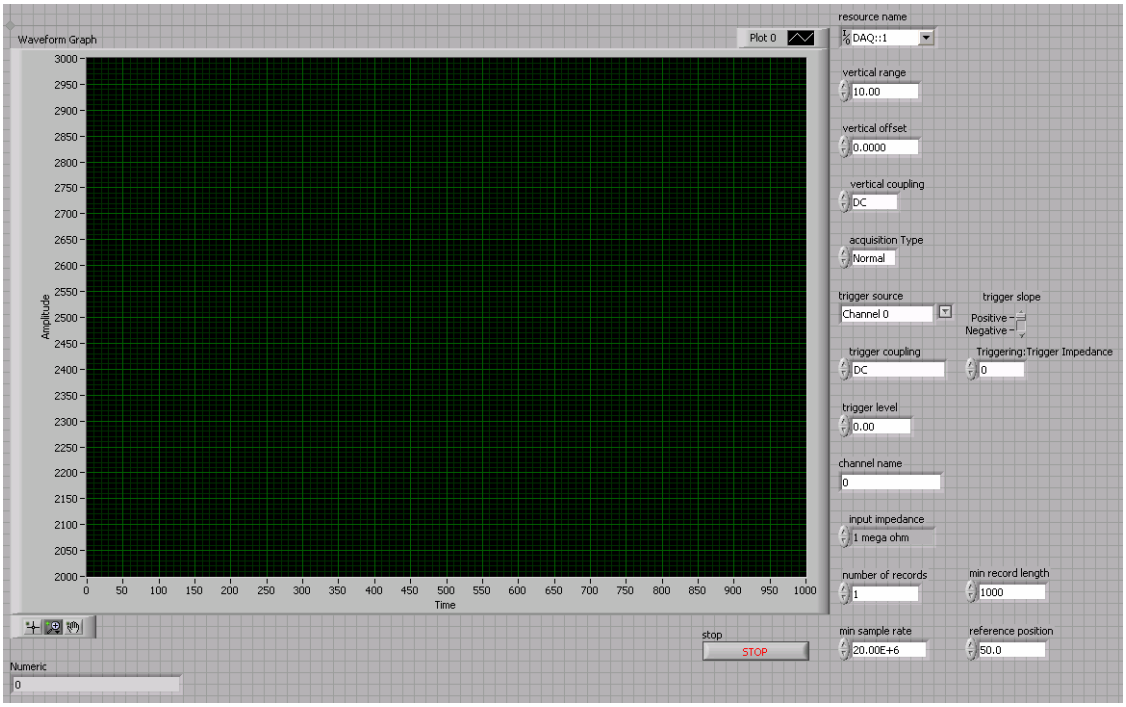

Figure 3.4 User Interface of the LabVIEW program

3.2.2 Deconvolution Shaping Method

In the absence of noise, the signal recorded by a system s(t) is the convolution of the input signal i(t) and the system response function h(t), or

$$s(t) = i(t) * h(t) \ .$$

In the frequency domain this is conventionally written as:

$$S(\omega) = I(\omega)H(\omega)$$

In a radiation detection system consisting of a scintillator detector and PMT, the input signal can be considered as a series of sharp spikes whose heights represent the energy deposited in the detector. The system response function is the impulse response of the combination of the detector and the PMT. By fitting the recorded signal s(t), we can find the system response function h(t). This system response function was used as the core function for the deconvolution shaping method, shown in Figure 3.5.

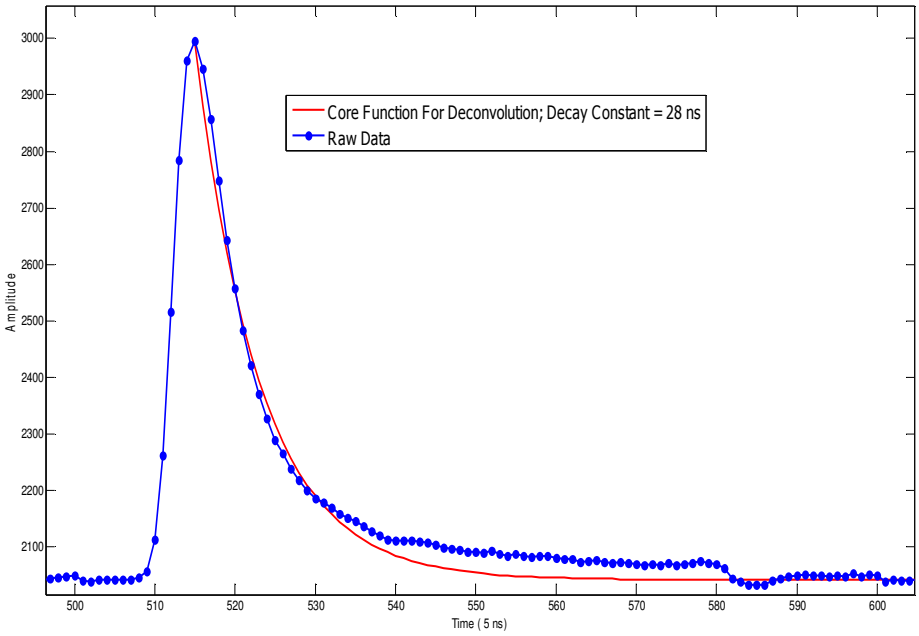

Figure 3.5 The Core Function Used in the Deconvolution Shaping Method.

H(ω) is a filter in the frequency domain for deconvolution, such that:

$$i(t) = F^{-1}\{S(\omega)/H(\omega)\} .$$

After deconvolution, the duration of each pulse is much shorter, so that subsequent analysis can resolve individual pulses arriving at much higher count rates. Because this is a linear process, the energy information is preserved. Signals before and after deconvolution are shown in Figure 3.6. The spectrum was measured at an average counting rate of 5×10^6 cps.

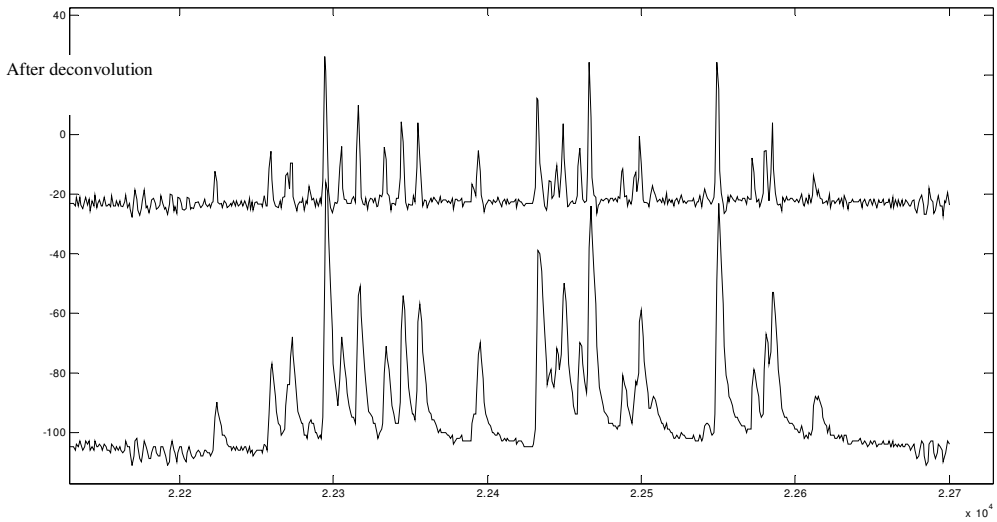

Figure 3.6 The signal recorded by a $LaCl_3$ detector during a 5 μs LINAC pulse before and after deconvolution

The analysis above assumes that noise is negligible; however, noise can be a limiting factor in practice. Since the deconvolution filter is a high-pass filter in the frequency domain, it can be sensitive to noise. By comparing the digital system to a conventional analog system, the impact of noise can be evaluated.

3.2.3 System Performance with noise

The system has been tested in our lab using a Co-60 source and a 1.5" by 1.5" $LaCl_3$ detector. For comparison, we also used an analog spectroscopic measurement system consisting of a pre-amplifier and shaping amplifier followed by an AMPTEK P180 pocket MCA (with a dead time of 2 μs after each event). By changing the distance between the source and the detector, varying event rates were input to the system.

Spectra generated by the digital and analog systems at both 10^3 cps and 10^6 cps are displayed in Figure 3.7. At the lower count rate (1 kHz), the energy resolution of the

digital system is comparable to the analog system. At the high count rate (1 MHz), the analog system has 90% dead time and only 10% energy resolution at 1.33 MeV due to the pile-up of adjacent pulses. (We did not have pile-up rejection with the conventional system). For comparison, the digital system had an energy resolution of 5% at 1.33 MeV with no loss of measured count rate.

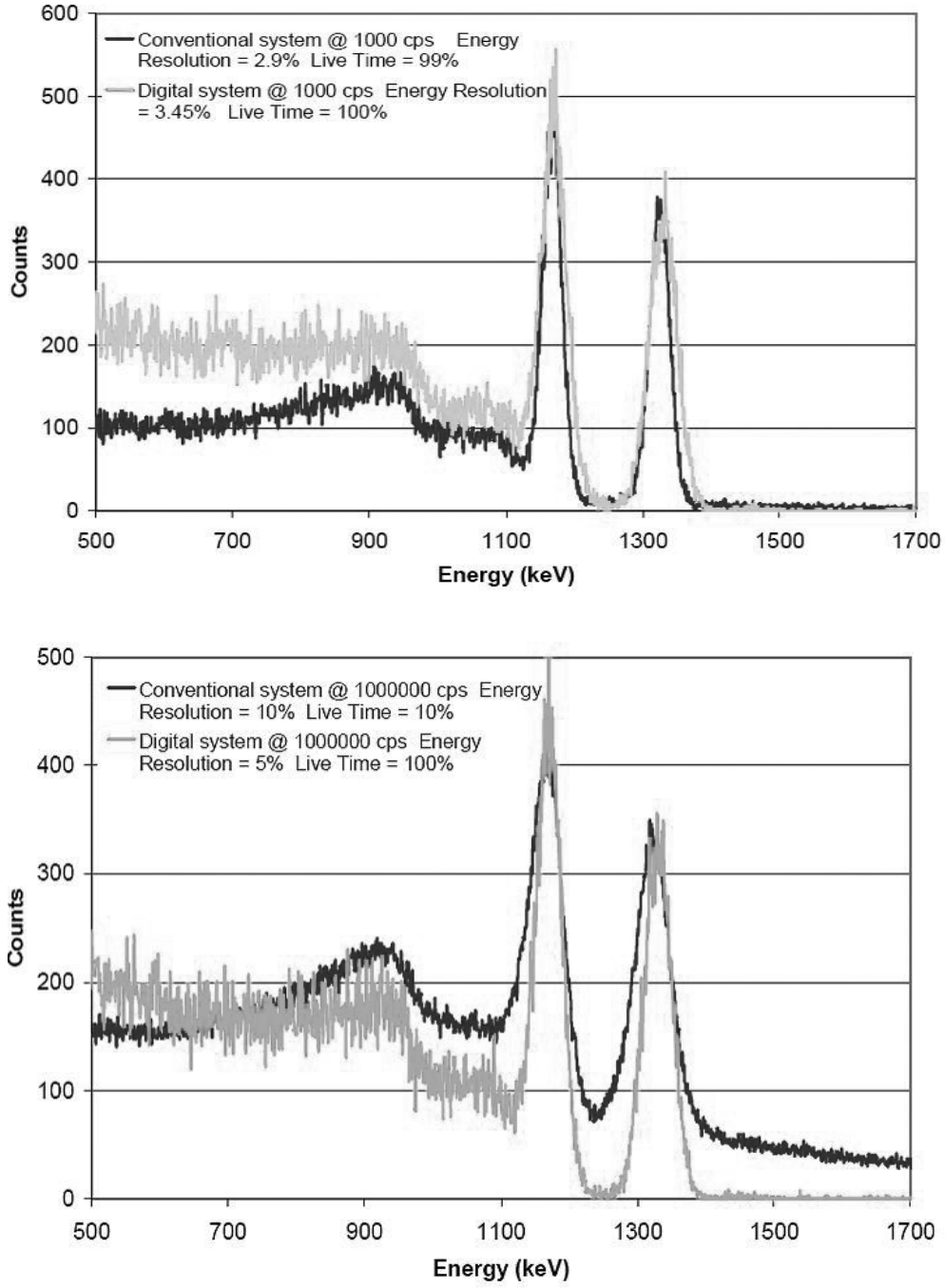

Figure 3.7 Comparison between the Co-60 spectra from the digital system and a conventional analog system at both low and high count rate

By bypassing the pre-amplifier and amplifier, very short shaping times were achieved. Using a standard deconvolution method on the digitized waveforms, overlapping pulses were resolvable. Thus, this system handles high count rates, but with a slight loss of energy resolution. Bundled with a $LaCl_3$ detector (28 ns decay time), the system has virtually no dead time at 10^6 cps. The energy resolution does degrade to 5% compared with 2.9% at 1000 cps for 1.33 MeV gamma rays, but as shown below, this tradeoff can be quite acceptable.

3.2.4 Implementation in Photofission Experiments

This system was used in photofission experiments using a medical 6 MeV radiation therapy machine. To our knowledge, this is the first fission product spectrum acquired between interrogation pulses using fast scintillation detectors. This greatly improves the sensitivity of the detection system.

This system was used together with a fast $LaCl_3$ scintillator detector (1.5" by 1.5" Saint-Gobain Brillance 350 detector). These experiments were conducted using the radiation oncology therapy LINAC in the hospital of the University of Michigan. The specifications of the LINAC are listed in Table 3.2. In these experiments, the LINAC was running at 6 MeV to minimize the production of photoneutrons. Also, 6 MeV LINAC's are much more commonly used at seaports than 12 MeV machines. The same uranium sample used in previous photofission experiments as described in Chapter 2 was used in these experiments as well. It is a depleted uranium fuel rod, with a length of 9 cm and a diameter of 1 cm. The density was calculated to be 14.8 g/cm^3.

Table 3.2 Specification of the Therapy LINAC

Available End Point Energies	6 MeV and 12 MeV
Duration of Radiation Pulses	5 μs
Repetition Rate	60 Hz to 360 Hz

In Chapter 2, the experimental results showed that even minutes after the irradiation, high-energy gamma rays emitted by fission products can still be used as signature signals for identification of SNM. In contrast, in photofission reactions the intensity of the delayed radiation (gamma rays and neutrons) emitted by fission fragments drops quickly as time goes on. Thus, to achieve maximum sensitivity, measurements should be started as quickly as possible following the end of the irradiation.

In these photofission experiments, delayed gamma rays were measured between adjacent LINAC pulses for 5 μs immediately following the irradiation. A schematic of the experiments is shown in Figure 3.8. The X-ray beam was collimated down to the size of the sample using the built-in MLC (Multiple Leaves Collimator). The $LaCl_3$ detector was shielded in all directions using 4 inch thick lead bricks except the forward direction, where a window was opened and covered by a 1 inch thick lead plate. The detector was positioned outside of the X-ray beam and pointed at the DU sample. The measurement was synchronized to the LINAC pulses, where the DAQ card was triggered by the rising edge of the gate signal (negative pulses) generated by the electrons when they hit the bremsstrahlung target. Thanks to the short dead time of the digital spectroscopy system and the fast decay constant of the $LaCl_3$ scintillator detector, the whole DAQ system was fast enough to measure the energy spectrum of the delayed gamma rays at a very high event rate (~ 10^7 cps).

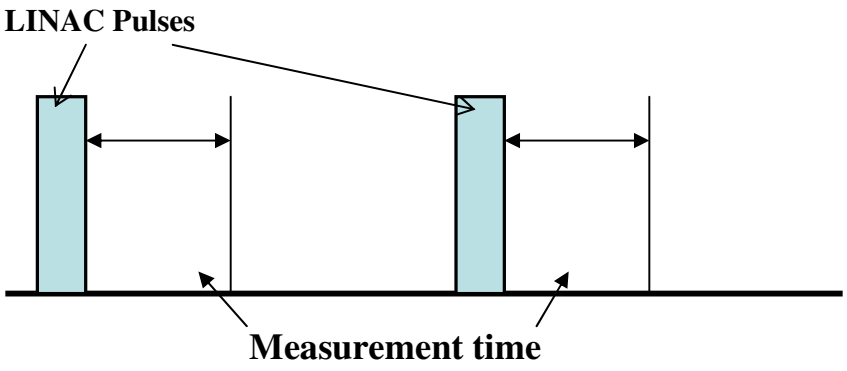

Figure 3.8 Detection scheme of the photofission experiments

In spite of the fact that the DU sample is fairly small (~100 g) and the fact that the end-point energy of the LINAC (6 MeV) is barely above the photofission threshold of U-238 (5.08 MeV) [54], a huge difference was still observed when the DU sample was present. However, the energy resolution of the $LaCl_3$ detector (3.8% at 662 keV) was not good enough to separate the individual peaks that were observed previously using an HPGe detector. The spectra are shown below in Figure 3.9.

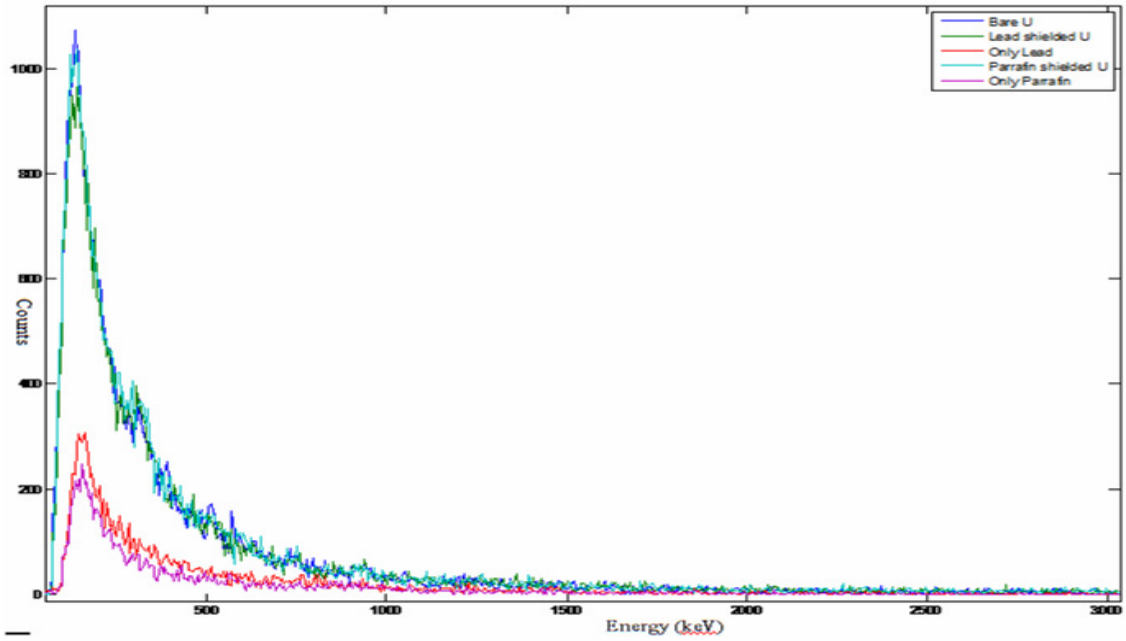

Figure 3.9 Delayed gamma-ray spectra measured between LINAC pulses immediately following the irradiation.

From these spectra, it can be seen that even with half-inch lead shielding around the DU sample, delayed gamma rays from the fission fragments were still observable and could be used as signature signals for detection of SNM. The capability of the combined digital spectroscopy system and fast scintillator to handle signals at high event rates allows measurements to start right after the irradiation pulses for maximization of system sensitivity.

This digital system worked well with a pulsed mode LINAC. However, the system throughput was limited by the data transfer rate to the PC and the modest onboard acquisition memory. The data transfer rate of a 32 bit 33 MHz PCI bus is 132 MB/s. The data input rate is 400 MB/s (2 Bytes per sample at 200 MSPS). Obviously, the PCI interface is not fast enough to achieve real-time data transferring. The fast onboard

memory operates synchronously with the digitizer. However, the memory size places a limit on the maximum length of each record. The maximum number of samples that an 8 MB onboard memory can hold is 4M, which then allows a maximum measurement time of 20 ms. If digital shaping and signal processing could be implemented at the front end, then only the essential information needs to be transferred, and a real-time energy spectrum could be produced from a larger set of data.

3.3 FPGA for Fast Pulse Processing

Not long ago, real-time digital signal processing could only be implemented on Digital Signal Processors (DSP). FPGA chips did not have the resources to implement complicated computation tasks like multiplication and division. In the middle 90's, a digital spectroscopic measurement system usually consisted of several DSP chips and a flash ADC, working at around 20 MHz [55]. However, FPGA's are well suited for this kind of application because of their distributed construction. Various tasks can be implemented on a single FPGA chip, running simultaneously without interfering with one another. Such a parallelism gives FPGA's the ability to handle much higher computational workloads than serial microprocessors. The results presented in this section show that nowadays a single, low-cost FPGA is powerful enough to drive an entire digital spectroscopic system.

This digital system was designed based on a fast ADC and an FPGA. The fast ADC continuously digitizes the input signal, and real-time signal processing as described below is implemented on the FPGA chip. Energy spectra are generated and stored in the memory available on the FPGA board and later transferred to a PC for display and

analysis via the RS232 interface. Since signal processing is done in real time on the FPGA chip, the amount of data which need to be transferred between the DAQ system and the PC is much less than in the previous design, and a high-speed interface is not required.

A trapezoidal shaping method and a two-fold Moving Window Deconvolution (MWD) algorithm were implemented on the FPGA chip for real-time DSP. The parameters can be adjusted to achieve a balance between speed and energy resolution.

3.3.1 Digital Spectroscopic Measurement System Design

Based on the hardware components presented in the previous section, a digital spectroscopic measurement system was developed. The top-level system schematic is shown in Figure 3.10 below.

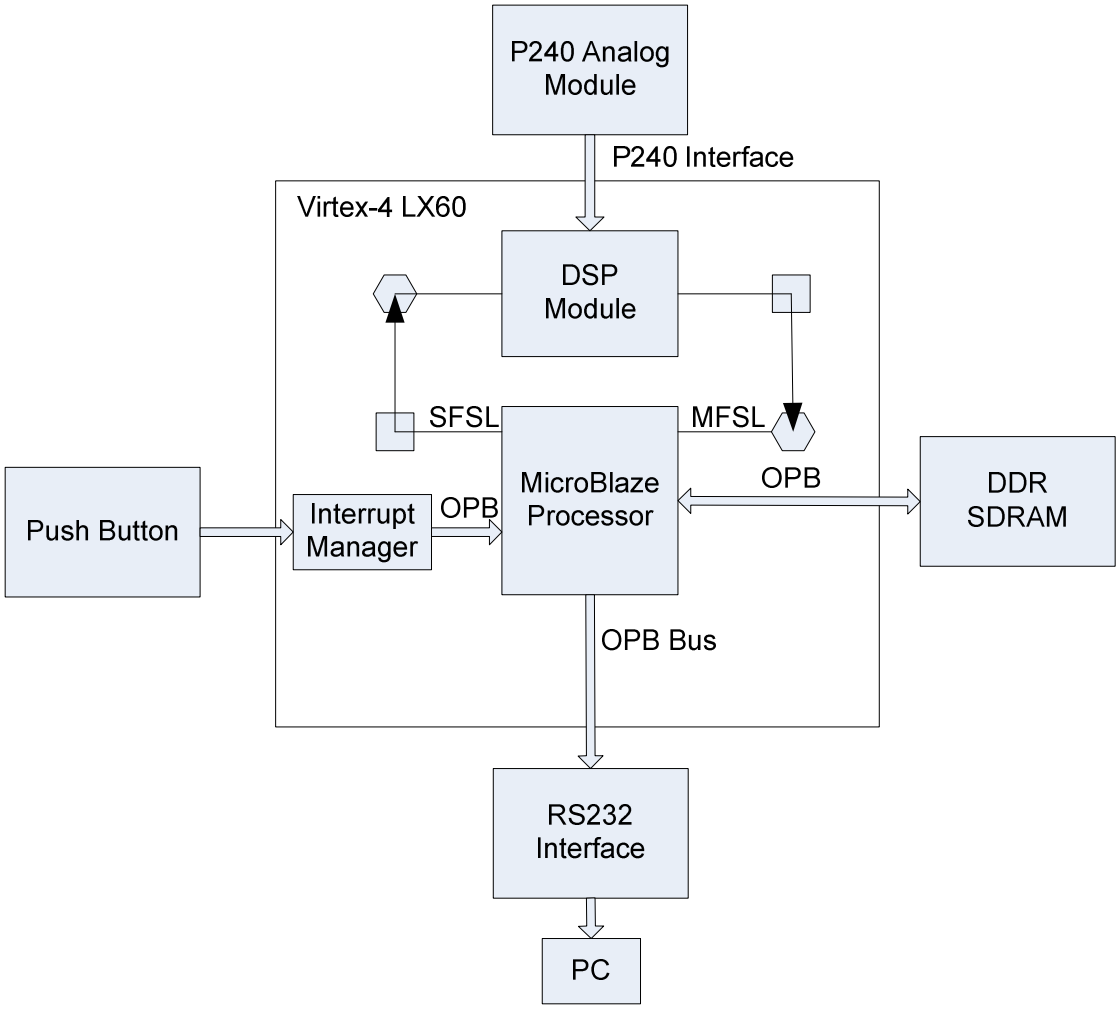

Figure 3.10 Top-level System Schematic

Incoming analog signals were fed into one of the two analog input channels provided on the P240 Analog Module. After digitization, signals were passed to the Virtex-4 LX60 FPGA chip through the P240 interface. The ADC sampling rate was determined by the output clock frequency from the ICS 8442 clock synthesizer on the Virtex-4 LX60 development board. A DSP module was developed in Matlab and Simulink using the Xilinx System Generator. The design was then converted to an FPGA implementation. Digitized signals were processed within this DSP module. On the

Virtex-4 LX60 FPGA, a MicroBlaze processor was implemented. This processor communicated with the DSP module through the FSL (Fast Simplex Link) bus. After digital shaping, energy information was extracted from the signals and stored in the DDR SDRAM. The MicroBlaze processor controlled the RS232 interface through the OPB (On-chip Peripheral Bus) bus. Energy spectra can be transferred to a PC through the RS232 interface, upon a user's request.

In the next sections, two real-time shaping methods and their implementation on the FPGA chip will be described.

3.3.2 Trapezoidal Shaping Method and its Implementation

Four fundamental considerations affect the choice of a pulse-shaping network in a nuclear spectroscopic measurement system, as pointed out by Goulding [56]:

1) Signal to noise ratio.
2) Maximum counting-rate.
3) Sensitivity to rise-time variance of the input signal.
4) Suitability of the output signal for feeding the MCA

The relative weights of these factors are determined by the needs of the application.

In his theory of optimal pulse shaping in high resolution spectroscopy, Goulding pointed out that noise occurring in a typical spectroscopy system utilizing a charge sensitive preamplifier can be attributed to two sources: the step noise and the delta noise.

Step noise refers to noise arising from the current flowing in the input circuit of the preamplifier. This includes gate-current of an FET, the leakage current in a detector, etc. The charge due to these noise sources is integrated by the input circuit capacitance

and appears as a voltage step at the input to the preamplifier. Delta noise is due to the current flow through the input and amplifying elements. It produces a short current "delta pulse" in the output circuit. For example, the major types of noise associated with a semiconductor detector are Johnson noise in the parallel resistor, Johnson noise in the series resistor and the shot noise in the sensitive region caused by the leakage current. The equivalent current sources of the shot noise induced by the detector leakage current and the Johnson noise in the parallel resistor are parallel to the detector capacitor. The charges generated by these two types of noise will produce a voltage step at the input to the preamplifier. They fall in the category of step noise. On the other hand, the Johnson noise in the series resistor is considered as delta noise.

Goulding proposed an index to measure the step noise [56]. Since the arriving rate of the step noise pulses n_{step} is independent of the shaping system, it is not included in this index:

$$< N_s^2 >= \frac{1}{S^2}\int_0^\infty [R(t)]^2 dt ,$$

where S is the amplitude of the response to a unit step noise input and R(t) is defined as the system response at the measurement time T_m due to the step noise occurring at time t before the measurement time.

A similar index can be derived for delta noise. The duration of each delta noise pulse is Δt. Δt is very short compared with the time constant of the shaping system. A delta function can be considered as a positive step function followed by a negative step function Δt later. The amplitude of both step functions is $1/\Delta t$. From the definition above, the response of this delta function occurring t prior to the measurement time T_m is:

$$\frac{1}{\Delta t}[R(t) - R(t - \Delta t)] = R'(t), \quad \text{when } \Delta t \to 0 .$$

Hence, an expression for the delta noise can be written as:

$$< N_d^{\,2} >= \frac{1}{S^2}\int_0^\infty [R'(t)]^2 dt$$

In order to minimize the ballistic deficit, a time-invariant trapezoidal pulse shaper was chosen. For such a shaper, we have:

$$< N_s^{\,2} >= \frac{1}{S^2}\int_0^\infty [R(t)]^2 dt = \tau_2 + \frac{\tau_1 + \tau_3}{3}$$

and

$$< N_d^{\,2} >= \frac{1}{S^2}\int_0^\infty [R'(t)]^2 dt = \frac{1}{\tau_1} + \frac{1}{\tau_3} .$$

where τ_1 is the rise time, τ_2 is the duration of the flat top and τ_3 is the fall time, as shown in Figure 3.11.

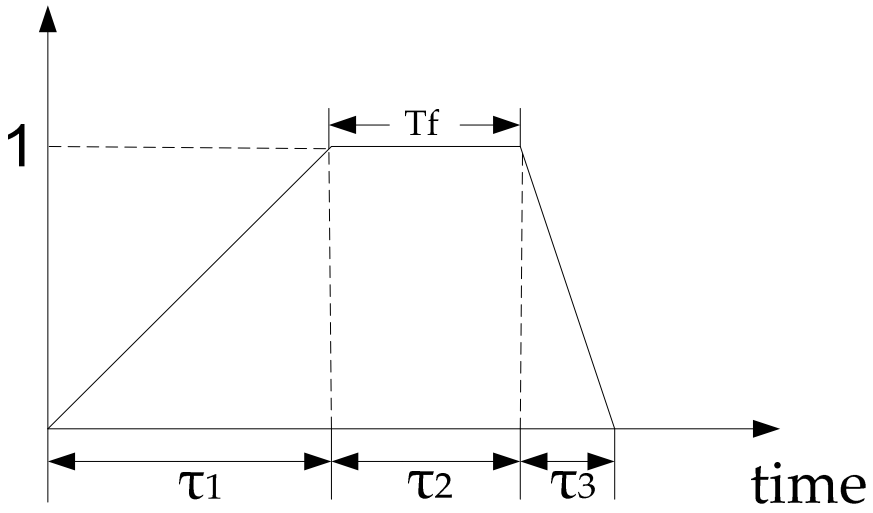

Figure 3.11 Time-invariant Trapezoidal Shaper

To minimize the sensitivity of the amplitude to detector signal rise time (ballistic deficit), a minimum flat top duration T_f is required. To handle a certain counting rate, a maximum duration T_s has to be set. Given these two requirements, it can be concluded that the best shaping performance is obtained when

$$\tau_1 = \tau_3 = \frac{1}{2}(T_s - T_f).$$

This is the reason why we usually use a symmetric trapezoidal shaper. Jordanov [57-58] described a way to develop a trapezoidal shaper that is suitable for real-time signal processing.

The convolution of an exponential input signal with a rectangular function is shown below in Figure 3.12. The resulting function can be written as:

$$p(t) = \int_0^t e^{(t'-t)/\tau} dt' = \tau(1 - e^{-t/\tau}), \quad 0 \le t \le T_2$$

$$p(t) = \int_0^{T_2} e^{(t'-t)/\tau} dt' = \tau e^{-t/\tau}(e^{T_2/\tau} - 1), \quad t > T_2$$

Similarly, the convolution of an exponential input signal with a truncated ramp function is shown in Figure 3.13. The result takes the form:

$$r(t) = \int_0^t t' e^{(t'-t)/\tau} dt' = \tau t - \tau^2(1 - e^{-t/\tau}), \quad 0 \le t \le T_1$$

And

$$r(t) = \int_0^{T_1} t' e^{(t'-t)/\tau} dt' = \tau e^{-t/\tau}(\tau + e^{T_1/\tau}(T_1 - \tau)), \quad t > T_1$$

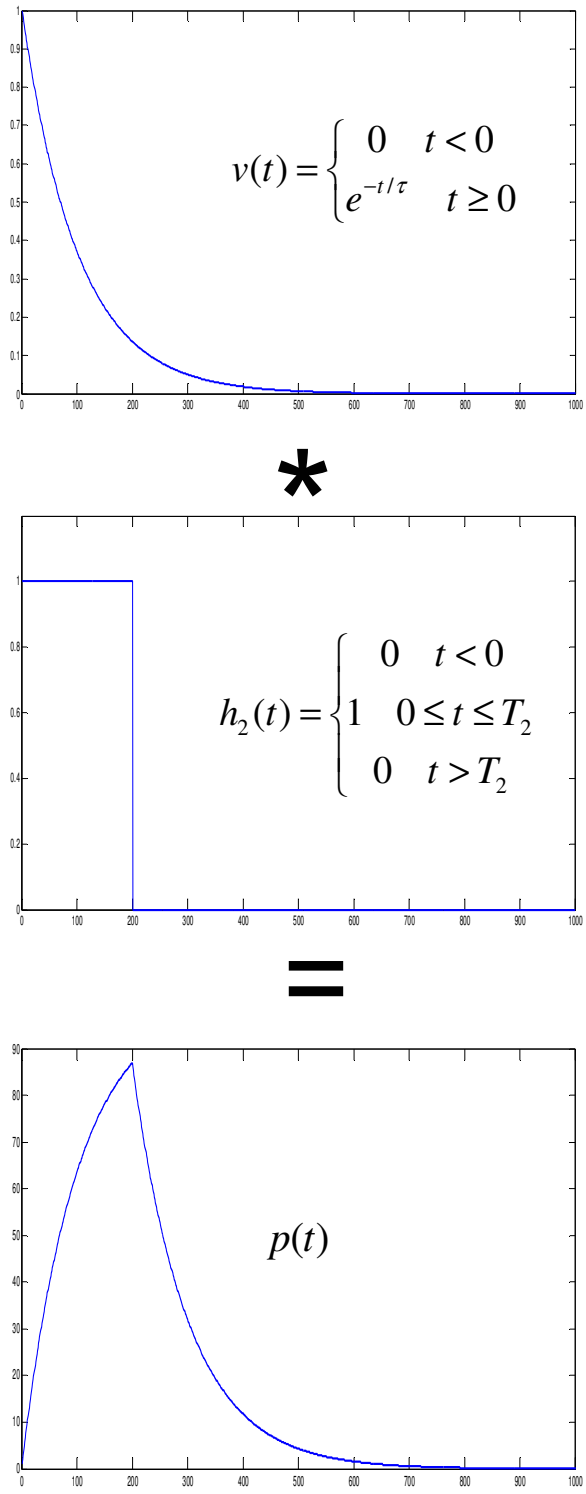

Figure 3.12 Convolution of an exponential signal v(t) with a rectangular function $h_2(t)$ produces p(t)

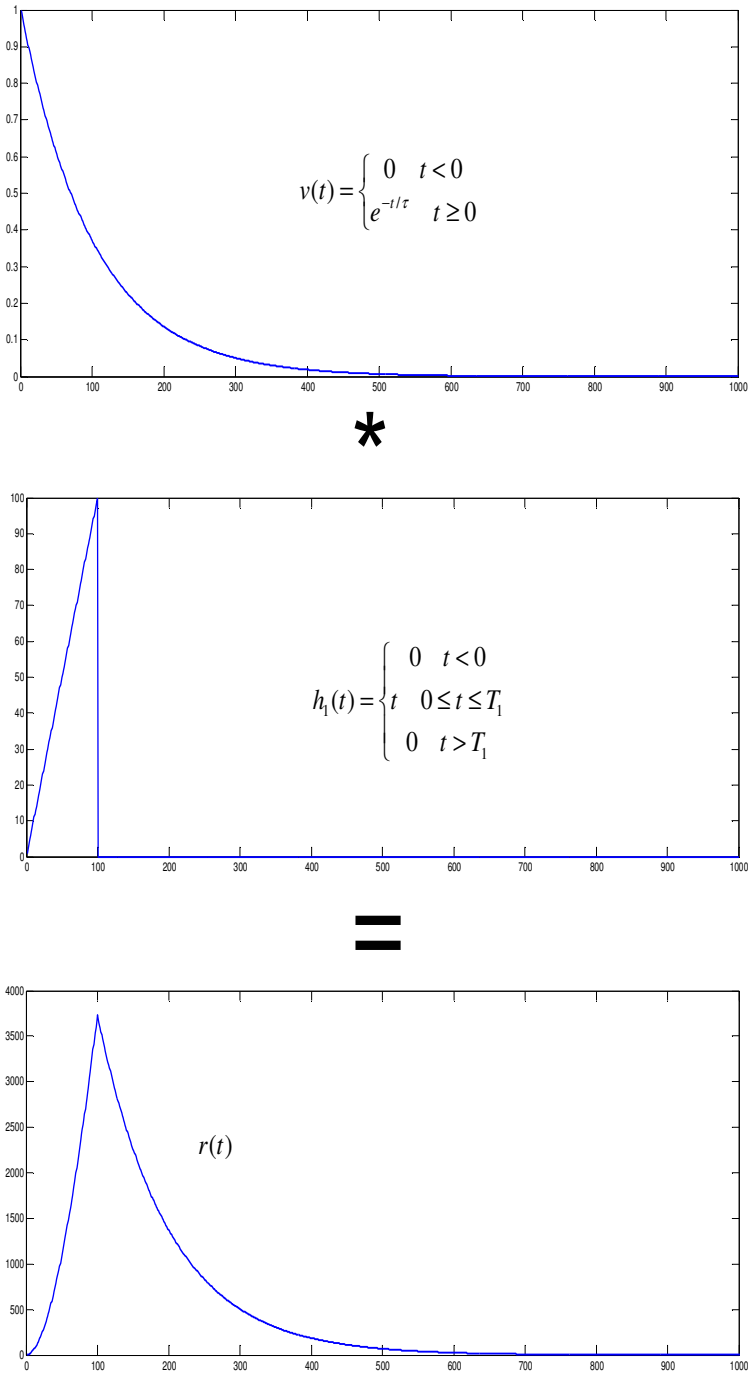

Figure 3.13 Convolution of an exponential signal v(t) with a truncated ramp function $h_1(t)$ produces r(t)

Under the condition $T_1 \le T_2$, consider a function defined as:

$$f(t) = r(t) + \tau p(t) + ap(t-T_1) - r(t-T_2),$$

where r(t) and p(t) are as described above.

When $0 \le t < T_1$

$$\begin{aligned} f(t) &= r(t) + \tau p(t) + ap(t-T_1) - r(t-T_2) \\ &= \tau t \end{aligned}$$

When $T_1 \le t < T_2$

$$\begin{aligned} f(t) &= r(t) + \tau p(t) + ap(t-T_1) - r(t-T_2) \\ &= \tau^2 + a\tau + \tau e^{-(t-T1)/\tau}(T_1 - \tau - a) \end{aligned}$$

When $t \ge T_2$

$$\begin{aligned} f(t) &= r(t) + \tau p(t) + ap(t-T_1) - r(t-T_2) \\ &= \tau^2 e^{-t/\tau}(e^{T_2/\tau} - 1) + \tau e^{-t/\tau}(\tau + e^{T_1/\tau}(T_1 - \tau)) + a\tau(1 - e^{-(t-T_1)/\tau}) \end{aligned}$$

If the value of the parameter a is set as $a = T_1 - \tau$,

$$f(t) = \begin{cases} \tau t & 0 \le t < T_1 \\ \tau T_1 & T_1 \le t < T \\ T_1\tau - \tau(t - T_2) & t \ge T_2 \end{cases}$$

Further, at time $T_3 = T_1 + T_2$, $f(t) = 0$. This is a symmetric trapezoidal function.

The impulse response of this shaper can be developed from f(t) based on the distributive rule of convolutions:

$$\begin{aligned} f(t) &= r(t) + \tau p(t) + ap(t-T_1) - r(t-T_2) \\ &\Leftrightarrow h(t) = h_1(t) + \tau h_2(t) + (T_1 - \tau)h_2(t-T_1) - h_1(t-T_2) \end{aligned}$$

where $h_1(t)$ and $h_2(t)$ are the truncated ramp function and rectangular function separately.

Convolution of an exponential input signal with such a shaper is shown in Figure 3.14.

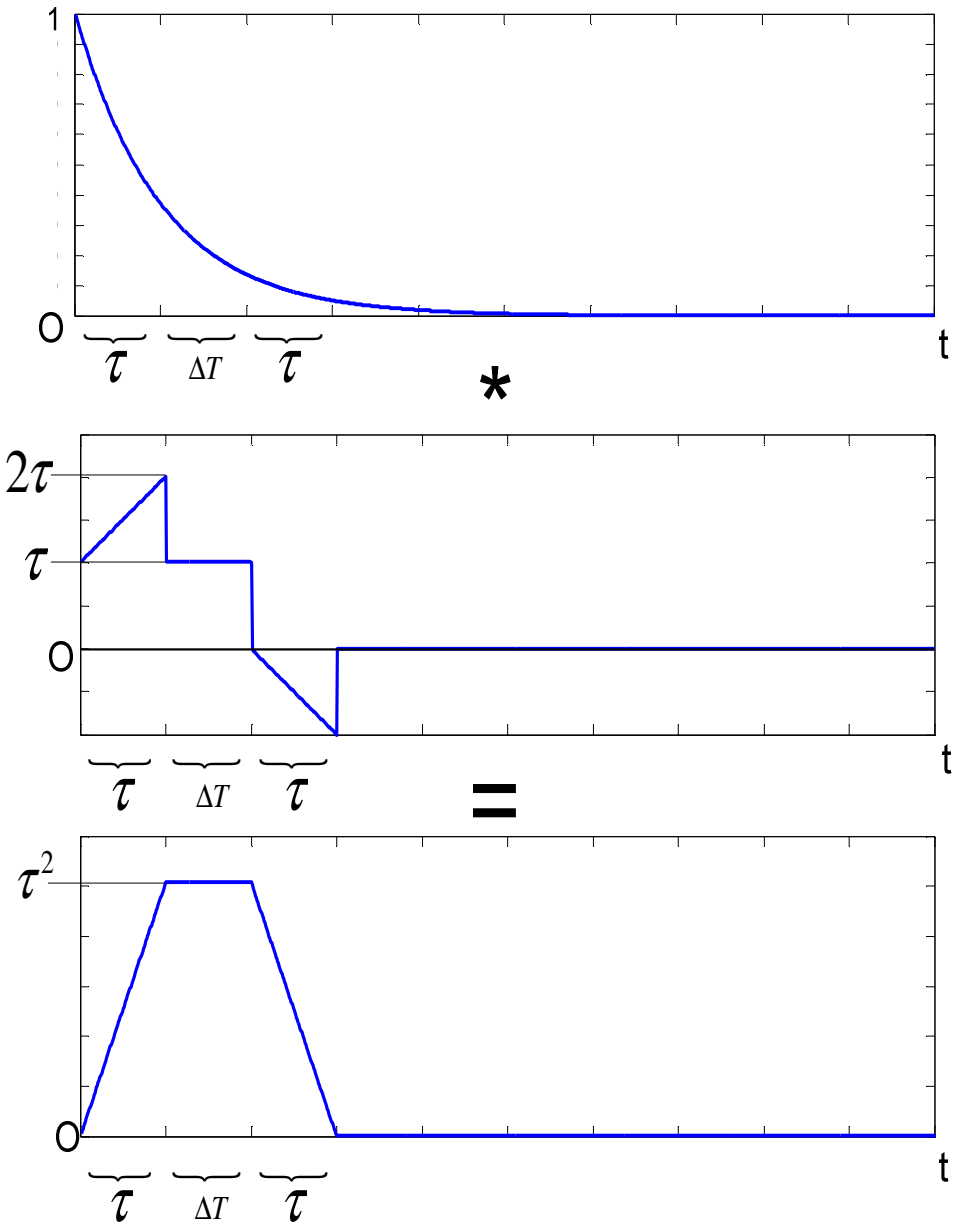

Figure 3.14 Convolution of an exponential input signal with the trapezoidal shaper

In order to implement this shaper with hardware in real time, a discrete recursive algorithm is needed. Suppose the input signal is v(n) and the decay time constant of the

digitized input exponential decay signal is M, the response of the system can be written in discrete time domain as:

$$s(n) = r(n) + Mp(n) + (k - M)\,p(n-k) - r(n-l)$$

where l is the width of the rectangular function and k is the length of the truncated ramp function. The duration of the flat top of the trapezoidal function after shaping is l-k.

Given the definition of $d^{k,l}(n)$ as

$$d^{k,l}(j) = v(j) - v(j-k) - v(j-l) + v(j-k-l),$$

the recursive form of the response function is given by

$$s(n) = s(n-1) + p'(n) + d^{k,l}(n)M \quad n \geq 0,$$

where

$$p'(n) = p'(n-1) + d^{k,l}(n) \quad n \geq 0.$$

This is the shaping algorithm used in this section. A block diagram of this shaping system is shown below in Figure 3.15. Standard signal processing blocks were used in this design, including delay pipelines, accumulators, multipliers and adders.

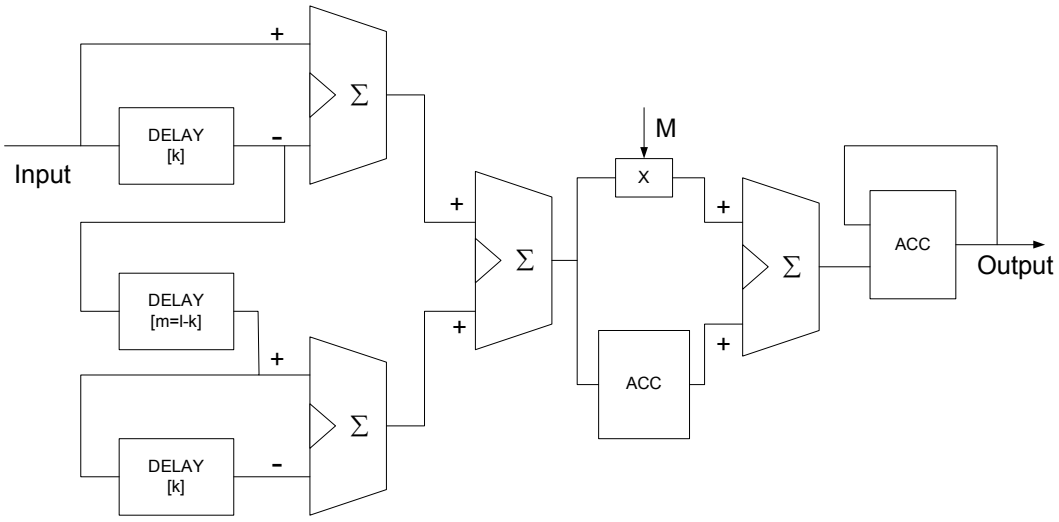

Figure 3.15 Block Diagram of Real-time Digital Trapezoidal Shaper

Such a trapezoidal shaper was implemented on the Virtex-4 LX60 FPGA. The shaper was first designed and simulated in Matlab/Simulink using Xilinx Blockset. Xilinx Blockset is a set of common signal processing modules. It was developed by Xilinx Corporation in order to utilize Simulink as a complete FPGA design tool from modeling to final implementation on hardware. Using the Xilinx System Generator software, a design based on Xilinx Blockset can be transformed into synthesizable, area-efficient VHDL code. Using Xilinx Blockset, it is also possible to import Matlab functions to create control circuits and to import an existing design written in HDL. The System Generator also provides a shared memory interface, so that signal processing designs based on Xilinx Blockset can be automatically converted into DSP co-processors with appropriate bus interface logic and software drivers to be used together with the Xilinx MicroBlaze processor. This feature is utilized in our design of a spectroscopic measurement system.

Some components from the Xilinx Blockset that were employed in this design are listed in Table A2.1 in Appendix 2.

The schematic of the design in Matlab/Simulink is shown below in Figure 3.16.

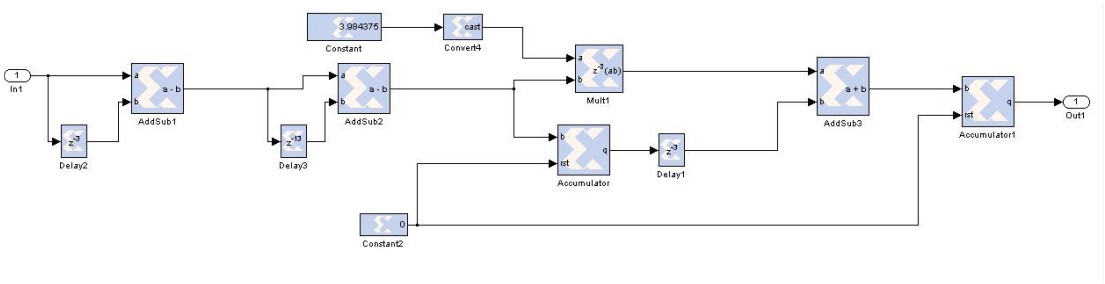

Figure 3.16 Trapezoidal Shaper Design in Matlab/Simulink

The shaper has been simulated in Matlab/Simulink. The input signal for this simulation was the direct output signal from a PMT coupled to a 1.5" by 1.5" $LaCl_3$ crystal, captured by an oscilloscope. The decay constant of this signal was determined to be 28 ns. The simulation result is shown below in Figure 3.17. The signal is so fast that the sampling rate of the ADS5500 ADC chip (125 MHz maximum, or sampling time Δt = 8 ns) on the P240 Analog Module is not fast enough to accurately reconstruct it. Artifacts can be observed in the signal before and after shaping.

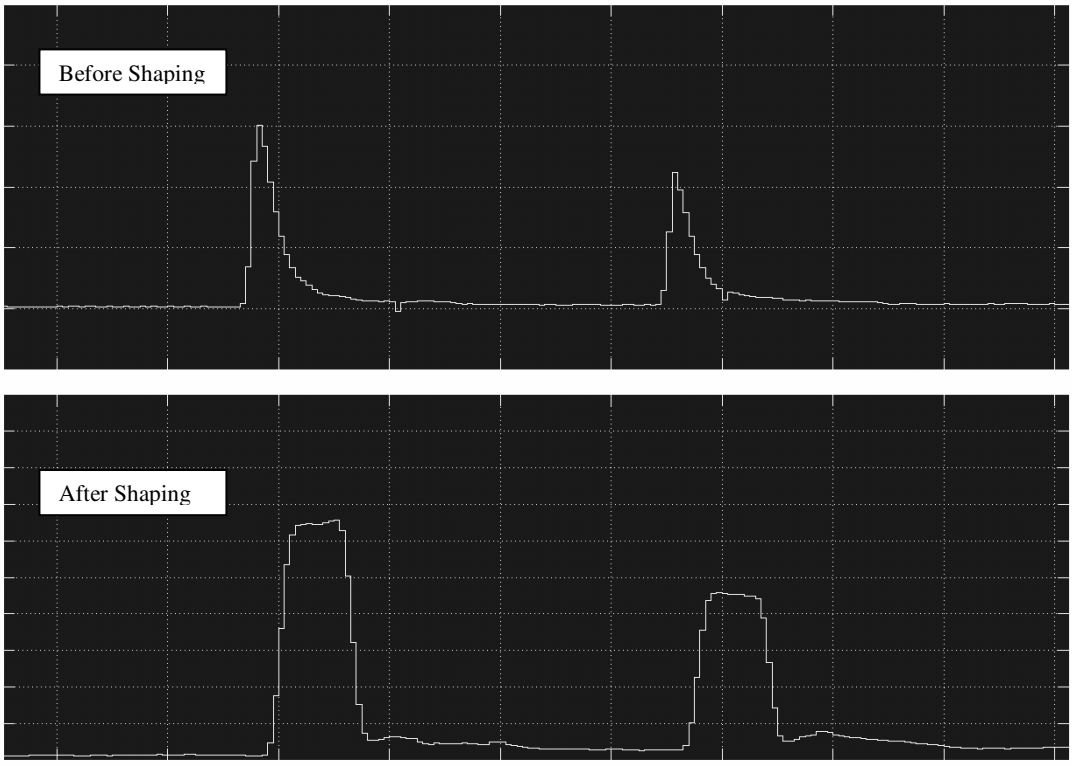

Figure 3.17 Simulation Result of the Trapezoidal Shaper Working on the Output Signal from a $LaCl_3$ Detector.

Another simulation of this trapezoidal shaper was conducted using the output signal from an HPGe detector as input. The HPGe detector is integrated with a pre-amplifier. The decay constant of the pre-amplifier output was measured to be 39.6 μs. Result of this simulation is shown below in Figure 3.18.

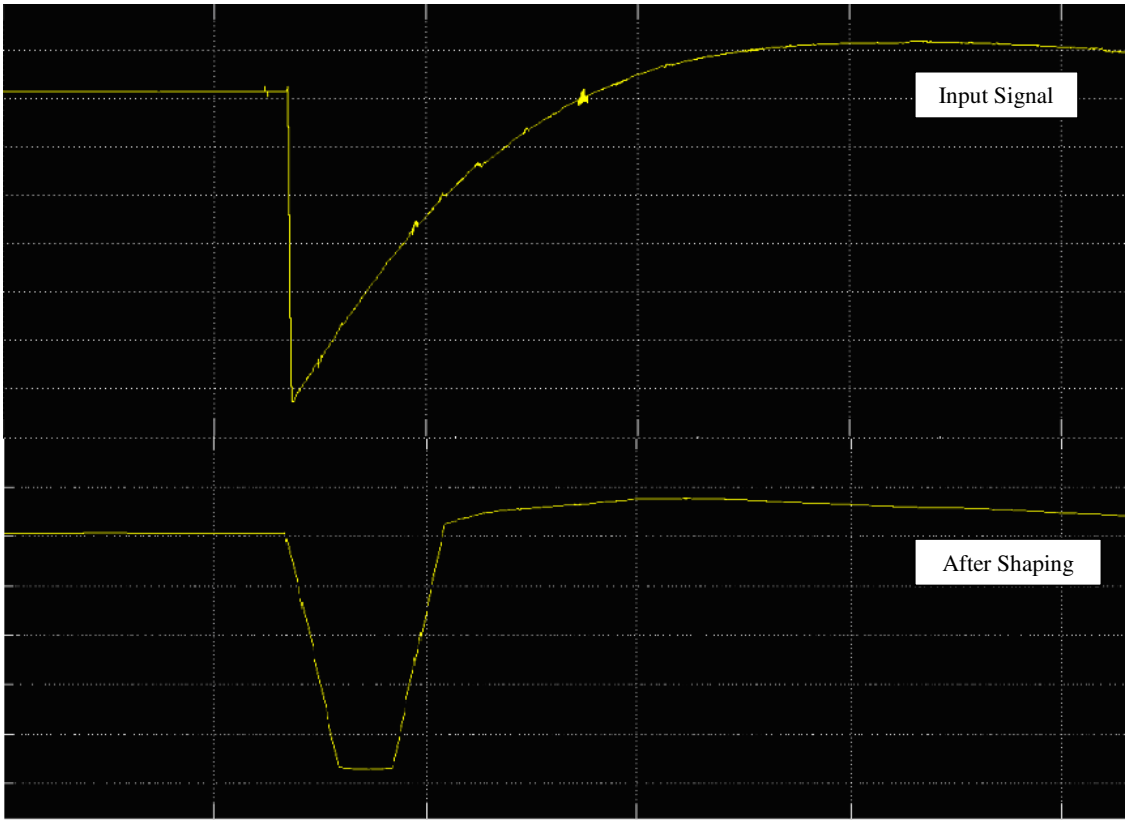

Figure 3.18 Simulation Result of Trapezoidal Shaper Working on the Output Signal from an HPGe Detector.

3.3.3 Moving Window Deconvolution Method and its Implementation.

A new signal processing method was introduced by A. Georgiev in 1993 [59] and discussed by M. Lauer [60]. The output function of this so called 'Moving Window Deconvolution' method contains at any time the total amount of charge induced in a defined window preceding that particular time point. This real-time signal shaping method was implemented on a Xilinx Virtex4 FPGA chip.

The output signal from a preamplifier connected to a radiation detector can be considered as the convolution between the charge distribution function $g(t)$ and the impulse response function of the preamplifier $f(t)$:

$$x(t) = g(t) * f(t) = \int_{-\infty}^{\infty} g(\tau) f(t-\tau) d\tau .$$

In a discrete system this can be written as:

$$x[n] = \sum_{j=-\infty}^{\infty} g[j] f[n-j] .$$

The analog part of any system should be time-invariant and causal. Preamplifier systems fall into this category. Given this, the formula above can be simplified as following:

$$x[n] = \sum_{j=-\infty}^{n} g[j] f[n-j] .$$

The number of items in this summation can be further reduced. A notable point in radiation detectors is that the charge collection is time limited. Hence, the charge distribution function should be time limited and must not extend the maximum charge collection time. Assuming that the charge collection is completed inside a time window with of length M, the above summation can be reduced to M items:

$$x[n] = \sum_{j=n-M}^{n} g[j] f[n-j] .$$

Consider a resistor feedback preamplifier where the ideal impulse response function can be described as a single exponential decay function:

$$f[n] = e^{-\alpha n} ,$$

where α is the exponential decay constant.

The total amount of charge inside a window of length M preceding a time point n can be written as[1]:

$$G[n] = \sum_{j=n-M}^{n} g[j] = x[n] - x[n-M] + \alpha \sum_{j=n-M}^{n-1} x[j], \text{ if } 0 < \alpha << 1$$

This is the output function of the Moving Window Deconvolution shaping method. The response of a pure RC circuit when the input is a burst of charge ($g(t) = \delta(t)$) is an ideal exponential decay signal. The result of MWD imposed on such a signal is shown below in Figure 3.19.

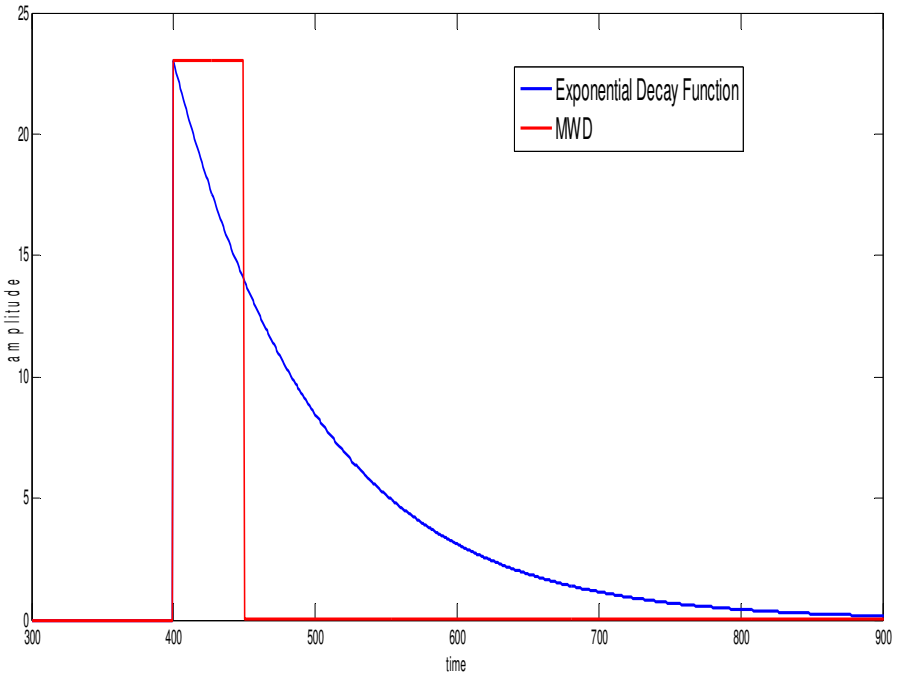

Figure 3.19 Moving Window Deconvolution of an Exponential Decay Function

[1] Refer to [60] for detailed derivation

For double-exponential decaying signals, where the two decay constants differ by a large factor, the MWD method also works. First, we choose a narrow window in which to do the deconvolution. The window is so narrow that the change of the component with the long decay constant can be neglected. In the next step, a similar deconvolution is conducted to compensate the slowly decaying component. The result of this process is shown in Figure 3.20 below.

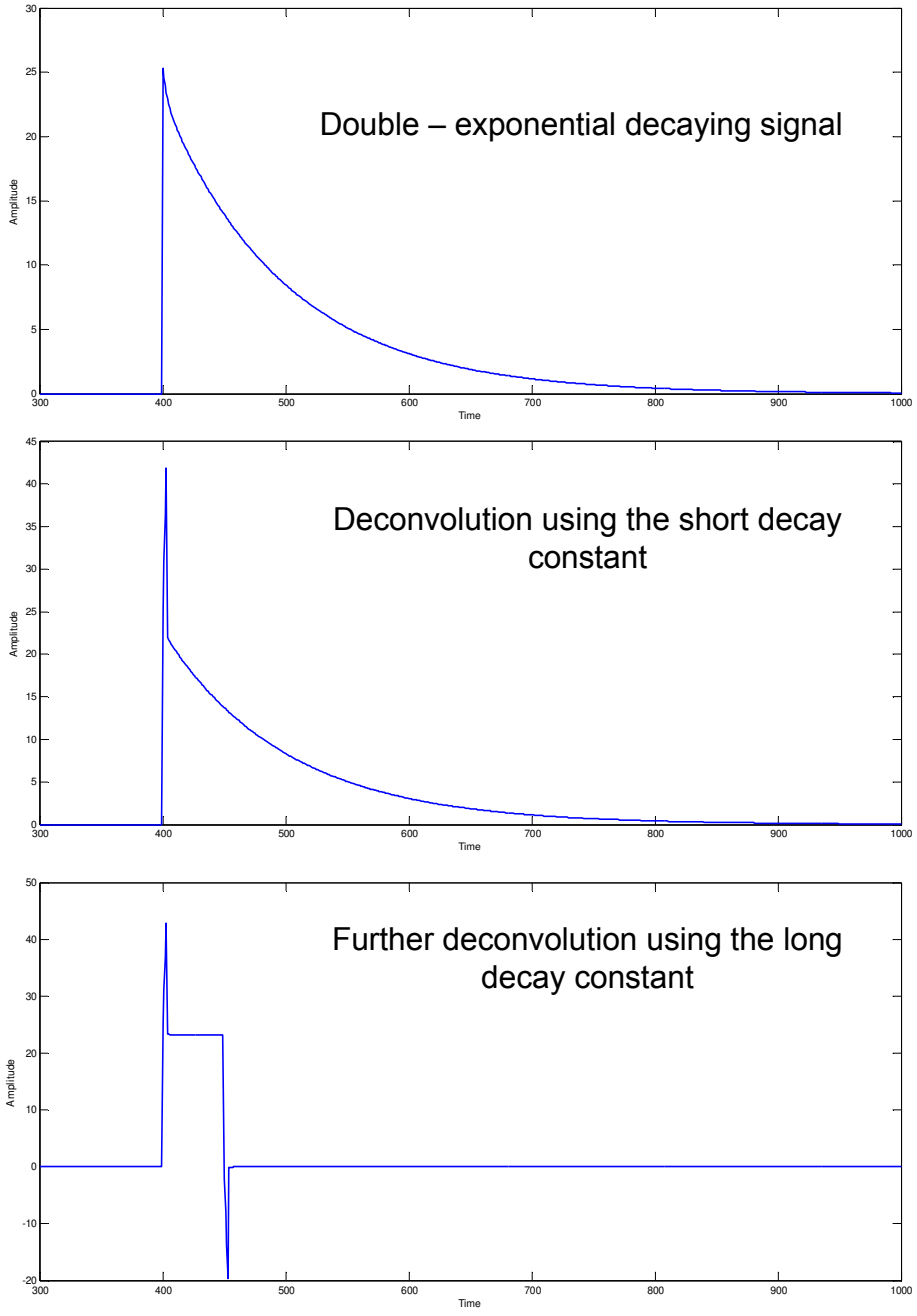

Figure 3.20 Two-fold Moving Window Deconvolution of Double – exponential Decaying signal

Following a similar design workflow as described in the previous section for the trapezoidal shaper, a two-fold MWD shaper was designed and simulated in

Matlab/Simulink using Xilinx Blockset and Xilinx System Generator software. The schematic of one stage of the two-fold MWD design is shown below in Figure 3.21.

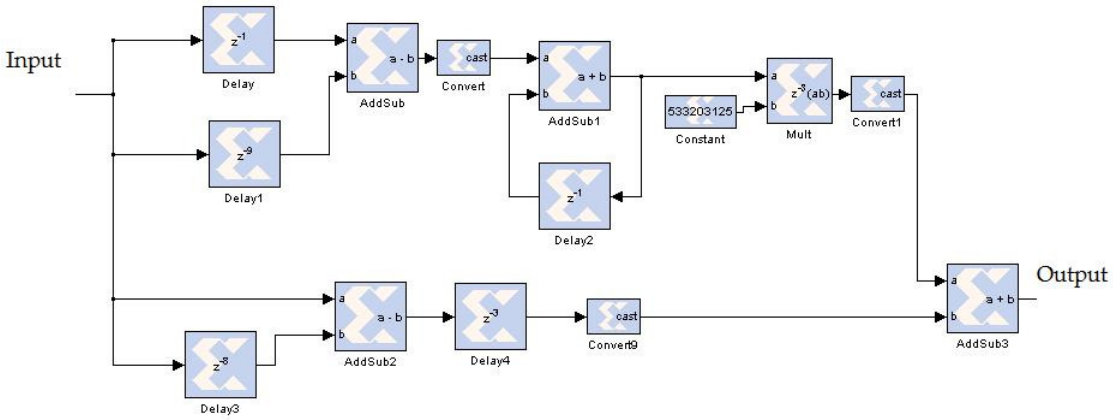

Figure 3.21 Design of MWD shaper in Matlab/Simulink

Simulation of this two-fold MWD shaper was conducted using the output signal from a PMT coupled with a $LaCl_3$ scintillator detector as input signal. The output signal from the PMT has two decaying components. The fast one is the main decaying component of the crystal, which has a decay constant of 28 ns. A much slower decaying component was also observed. The source of this slow component is not clear. Distortion caused by front end electronics is one possible origin. The simulation result is shown in Figure 3.22.

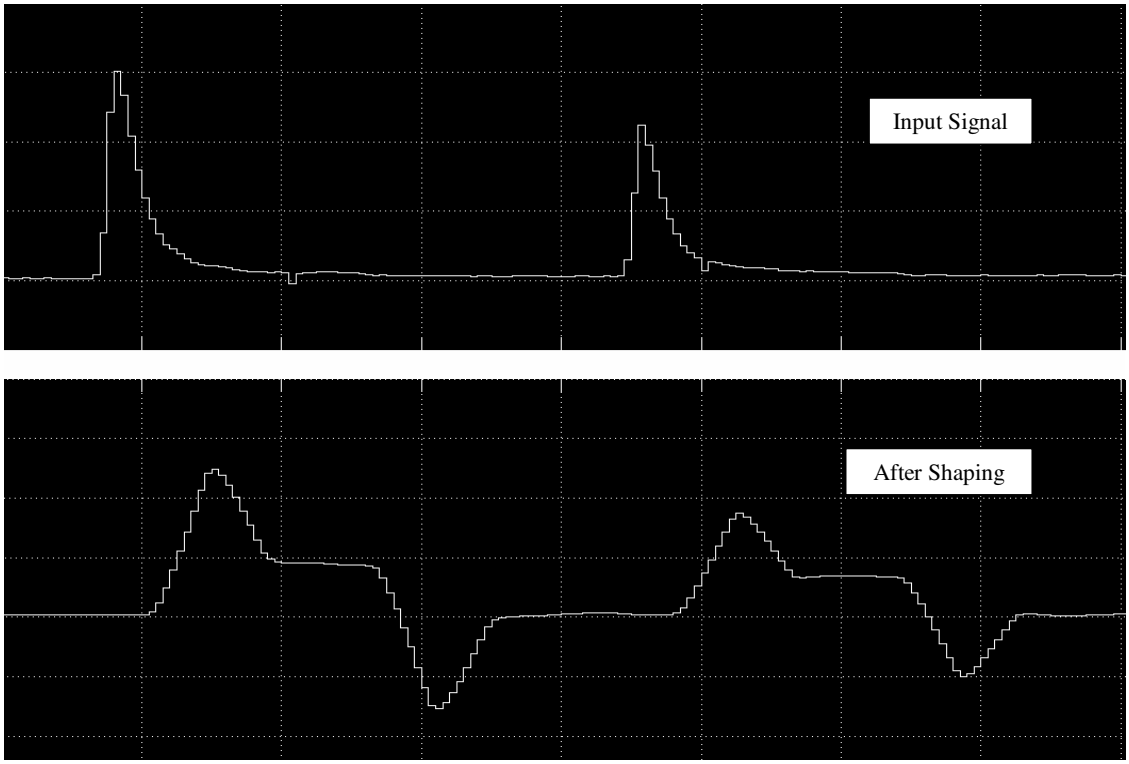

Figure 3.22 Simulation Result of the Two-fold MWD shaper

3.3.4 System Performance

The digital spectroscopy measurement system designed using the Xilinx Virtex4 FPGA chip was tested in the lab using a Co-60 source and a 1.5" by 1.5" $LaCl_3$ scintillator detector. The output from the PMT was directly fed into the P240 Analog Module. Both the trapezoidal shaping method and the moving window deconvolution method were implemented and tested on this system. They have been compared with an analog system consisting of ORTEC 113 Scintillation Preamplifier, ORTEC 472 Amplifier and AMPTEK MCA-8000A multi-channel analyzer. The system has a dead time of 2 μs after each event.

By changing the distance between the Co-60 source and the $LaCl_3$ detector, various count rates can be obtained. The system was tested under conditions where the analog system has virtually no dead time and when it has 50% dead time (equivalent to a count rate of 5×10^6 cps). The results of the comparison between the analog system and the system based on an FPGA utilizing the Trapezoidal and MWD shaping methods are shown below in Figure 3.23 and Figure 3.24, respectively. It can be observed that at low count rates the digital spectroscopy system based on an FPGA chip competes very well with the analog system in terms of energy resolution; at high count rates, the digital system experienced much less dead time and pile-up and very little degradation of the energy resolution. Since the primary goal for this system is to increase the throughput, this loss of resolution was deemed to be reasonable.

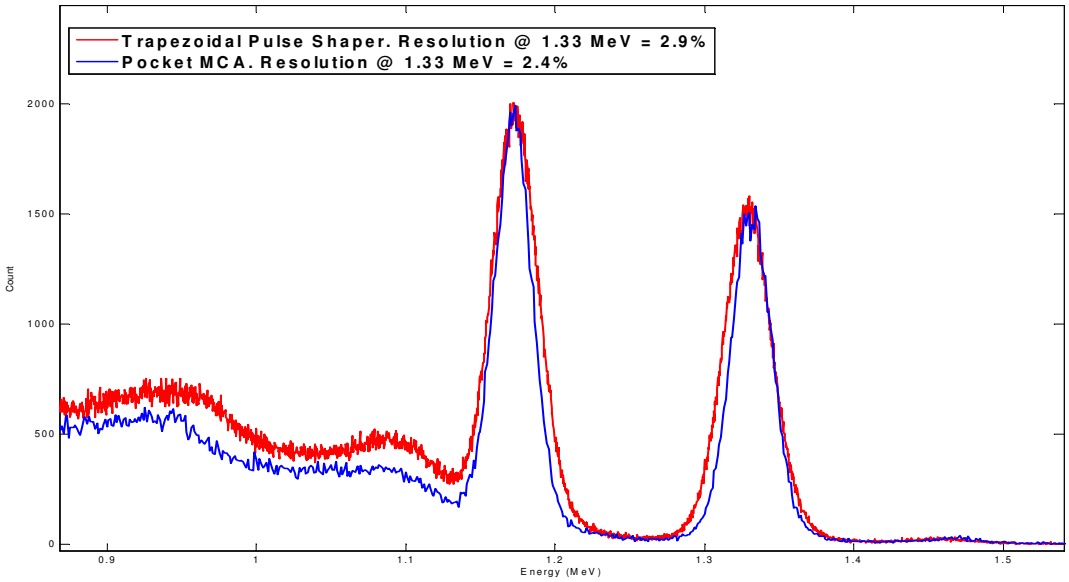

1) Comparison between the spectra taken by the analog system (blue) and the digital system utilizing trapezoidal shaping method at low count rate

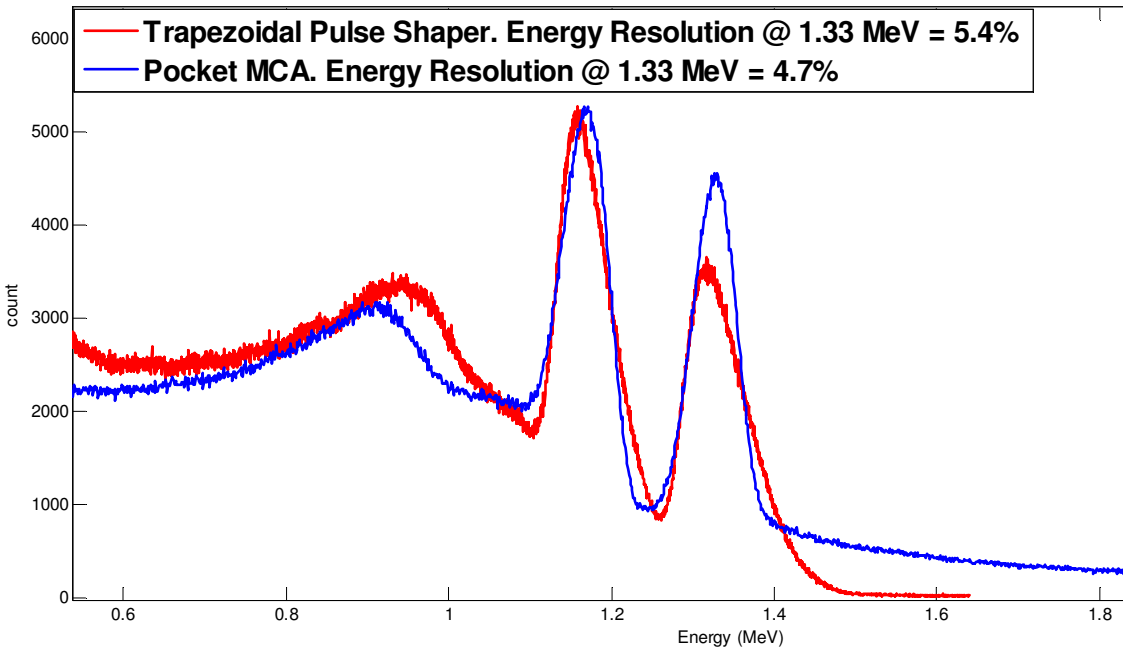

2) Comparison between the spectra taken by the analog system (blue) and the digital system utilizing trapezoidal shaping method at high count rate

Figure 3.23 Comparison between the analog system and the digital system based on an FPGA utilizing the trapezoidal shaping method at both low count rate and high count rate

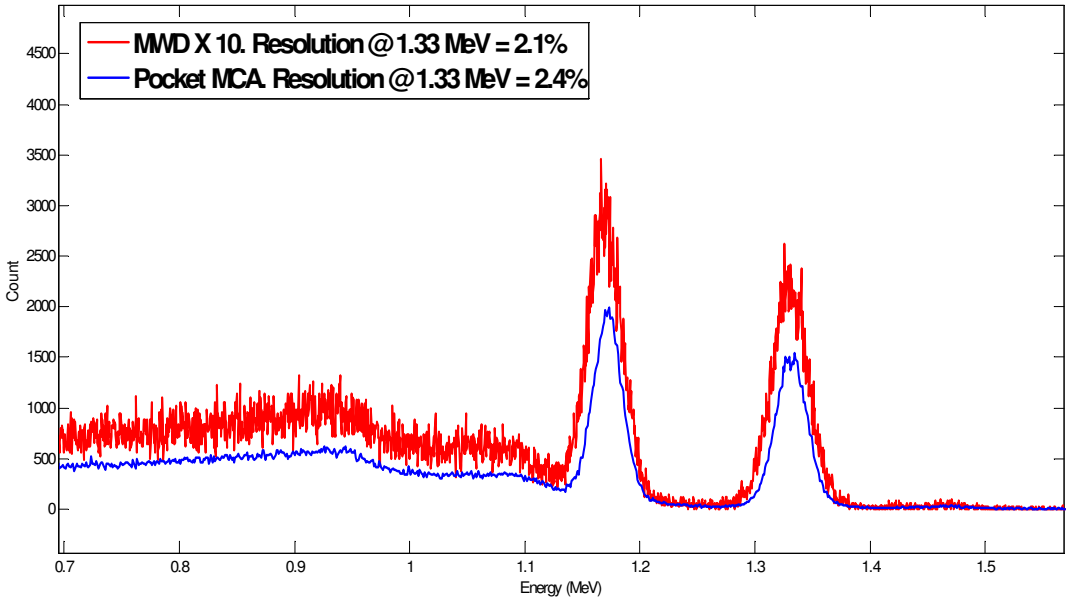

1) Comparison between the spectra taken by the analog system (blue) and the digital system utilizing MWD shaping method at low count rate

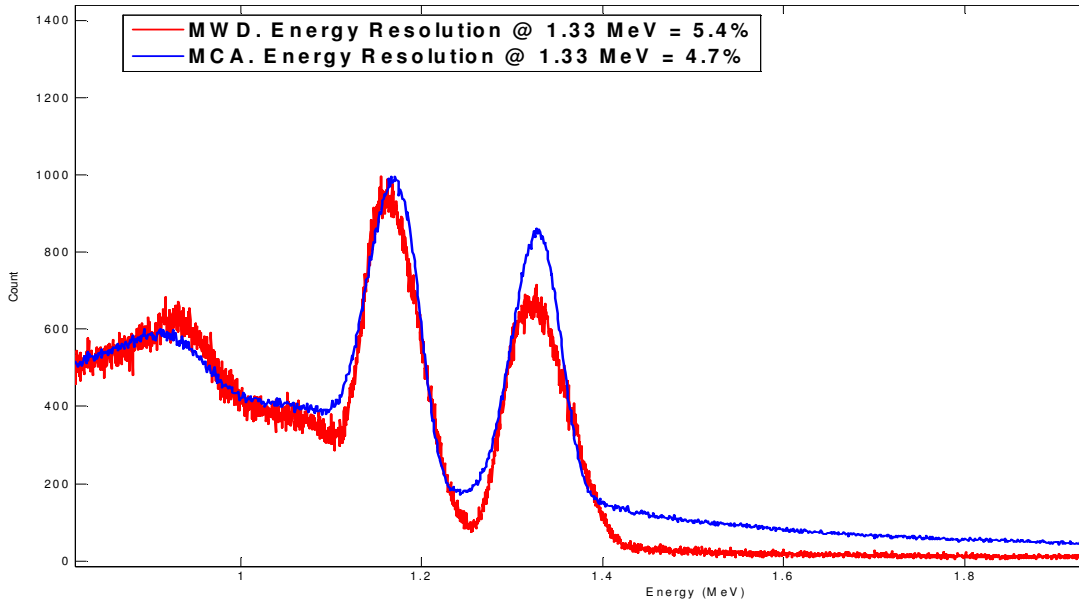

2) Comparison between the spectra taken by the analog system (blue) and the digital system utilizing MWD shaping method at high count rate

Figure 3.24 Comparison between the analog system and the digital system based on an FPGA utilizing the MWD shaping method at both low count rate and high count rate.

3.4 Conclusion and Future Work

In this chapter, the development of two digital spectroscopy systems was discussed. The first system is based on a National Instruments Data Acquisition card – PCI – 5124. It has very high sampling rate (200 MSPS) and excellent resolution (12-bit). The system was designed to work together with a pulse mode LINAC. Data acquisition is synchronized with the accelerator pulses by connecting the trigger input on the DAQ board and the output gate signal generated in the LINAC when electrons hit the target. Together with a fast scintillator detector, radiation energy applied with a high event rate ($\sim 10^6$) can be measured without experiencing significant dead time and degradation of energy resolution. The deconvolution method used during signal processing is not a causal process, thus it is not possible to implement this shaping method in real time. The deconvolution filter is a high-pass filter, which will make the system more sensitive to electronic noise. The raw waveform will be stored in the flash memory on the DAQ board and then processed by the host PC during the quiescent time period between LINAC pulses. Thus, the maximum duration of the measurement is limited by the size of the onboard flash memory. In our case, this number is 5 μs with a sampling rate of 200 MSPS and a resolution of 12 bits.

The second digital spectroscopy system was developed based on a fast ADC chip and an FPGA chip. The input signal was digitized and then processed by the FPGA using either the trapezoidal shaping method or the MWD shaping method. These two shaping methods were both implemented on the FPGA in such a way that the signal processing could be done in real time. The spectrum formed was stored in the local flash memory.

Thus the requirement of a fast data-transfer interface between the DAQ system and the host PC was eliminated.

System performance of these two digital spectroscopy measurement systems has been evaluated and compared with that of a traditional analog spectroscopy system. At low count rate, the digital systems yield energy resolution almost as good as that from the analog system; at high count rates, the digital systems have much less dead time without degradation in energy resolution.

The first system, based on a NI DAQ board, was used in a series of photofission experiments. Bundled with a fast scintillator detector, the spectroscopy system was fast enough to handle input signals with an event rate of roughly 10^7 cps. The spectrum measurement was synchronized with the end of the LINAC pulses. Energy spectra of delayed gamma rays emitted by fission fragments were measured between adjacent LINAC pulses right after the irradiation pulses for maximum system sensitivity. Data from this system were presented in Section 3.2.4.

The second system based on FPGA and ADC chips was implemented in NRF experiments, where a DC mode Van de Graaff accelerator was used as the interrogation source. Performance and measurement results are shown in Chapter 4.

For comparison, the performance of the two digital systems and the analog system is listed here in Table 3.3.

Table 3.3 Comparison of system performance

Digitize-and-Transfer System Used for Photofission Experiments:

Systems	**Low Count Rate Resolution ($\frac{\Delta E}{E}$) at 1333 keV**	**High Count Rate Resolution ($\frac{\Delta E}{E}$) at 1333 keV**	**Dead time at High Count Rate**
Analog System	2.9 %	10 %	90 %
Digitizer based system	3.45 %	5 %	10 %

FPGA-based System Used for NRF Experiments:

Systems	**Low Count Rate Resolution ($\frac{\Delta E}{E}$) at 1333 keV**	**High Count Rate Resolution ($\frac{\Delta E}{E}$) at 1333 keV**	**Dead time at High Count Rate**
Analog System	2.4 %	4.7 %	50 %
FPGA based system (Trapezoidal)	2.9 %	5.4 %	0
FPGA based system (MWD)	2.1 %	5.4 %	0

By eliminating the pre-amplifier and digitizing the output from the PMT directly, these digital spectroscopy measurement systems can achieve a much smaller dead time when used together with scintillator detectors, compared with traditional analog systems. The flexibility to set shaping parameters by software provides a fast and cost-friendly way to obtain optimal balance between through-put rate and energy resolution. The improved signal processing capability of the FPGA chips makes it possible to build a very compact self-contained spectroscopy measurement system.

Subsequent to our published work on this topic, the advantage of acquiring data between pulses was recognized by Reddy et al. [61]. They modified the preamplifier on their HPGe detector and acquired spectra between pulses. In the spectra they show, the ^{238}U target was photoactivated using the beam generated by a 16 MeV pulse mode LINAC. The accelerator was operated at 30 Hz with 85 nC of electron charge per pulse and the total irradiation time was about 60 minutes. Spectrum of delayed gamma rays was acquired between LINAC pulses. The data recorded within 13 ms after

bremsstrahlung pulses was removed. They have also measured the delay gamma spectrum for another 60 minutes starting 1 second after the last bremsstrahlung pulse. Because of the much higher beam energy, they were able to induce much higher fission reaction rate in their sample than we were able to in our work shown in Chapter 2. However, they didn't show the spectra in the energy range we worked in (below 2 MeV). The spectra they presented are shown in Figure 3.25 below:

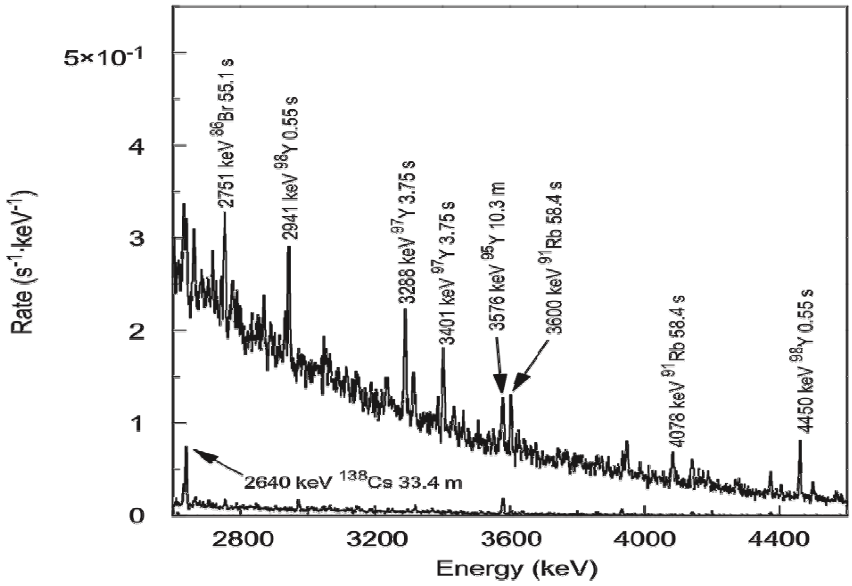

Figure 3.25 Delayed gamma ray spectra measured between bremsstrahlung pulses (upper spectrum) and after the irradiation (lower spectrum)

CHAPTER 4

Nuclear Resonance Fluorescence Technology in Homeland Security Applications

4.1 Introduction

In homeland security applications, detection systems should be able to not only detect the presence of SNM but also identify the specific materials. This can be done with the photofission technique based on differences in fission product yields [44-45, 62], or possibly on differences in the time dependence of delayed neutrons and gamma-rays [39, 51-52, 63]. However, these approaches either require complicated spectrum analysis, or dual or multiple beam energies, and the accuracy can easily be affected by attenuation due to surrounding materials.

Conventional atomic X-ray imaging systems provide gross sensitivity to atomic number. These systems are based on the principle that materials preferentially attenuate or scatter photons with specific energies determined by atomic composition. The binding energy of the most tightly-bound K shell electrons is on the order of 100 keV. The energies of the X-rays have to be small enough to investigate the atomic structure. However, X-rays with such low energies suffer high attenuation and cannot penetrate objects with high density. This limits the X-ray fluorescence technique to surface surveys [64]. Increasing the energy of the interrogation X-rays will make them more

penetrating, but the attenuation coefficients are simply a function of electron density at these energies, and the gross sensitivity to atomic number is lost.

Nuclear Resonance Fluorescence (NRF) can be considered to be the nuclear analog of the atomic X-ray fluorescence process [36]. NRF is the process of resonance excitation of certain nuclear levels by absorption of photons and subsequent decay of these levels by re-emission of equivalent radiation. Because the energy level structure is unique for each isotope, the resonant energies can be used as fingerprints for isotope identification. Thus, the energy spectrum of the resonantly scattered photons can be used to identify the detailed isotope content of materials of interest. Since every nuclear isotope with an atomic number bigger than two has energy levels that can be excited by photon absorption, detection systems based on NRF interaction are not limited to SNM, finding wide application in material characterization, waste management, and other areas in addition to homeland security. Compared with atomic fluorescence, NRF photons have much higher energies. These multi-MeV photons are highly penetrating and easy to detect.

In a detection system based on NRF, interrogation photons are used to induce resonance excitations in nuclei, and the de-excitation photons are measured to generate an energy spectrum. The two most commonly used detection schemes are the scattering method and the self-absorption method. In the scattering method, materials of interest are placed in an X-ray beam, and detectors are located out of the beam using a backscattering geometry as shown in Figure 4.1. All but the resonantly scattered photons at this angle are expected to have low energies, owing to the nature of Compton scattering. Thus, resonant photons can be discriminated on the basis of energy. In the

self-absorption method, the X-ray beam goes through the object, after which it strikes a sample containing isotopes of interest. A transmission detector is located downstream in the beam line to monitor the flux of the off-resonance photons. A radiation detector, called the "notch detector" is located out of the beam and is pointed at a sample of the isotope of interest in a backscattering geometry, measuring the resonant photons scattered by this sample. The system setup is shown in Figure 4.2 below. The count rate under the resonant peaks registered in the notch detector is proportional to the flux of the resonant photons hitting the sample. Whenever a preferential attenuation of resonant photons is observed, the conclusion can be drawn that isotopes of interest are present in the object. This is registered as a disparity between the flux of off-resonant photons and that of resonant photons registered in the transmission detector and the notch detector separately.

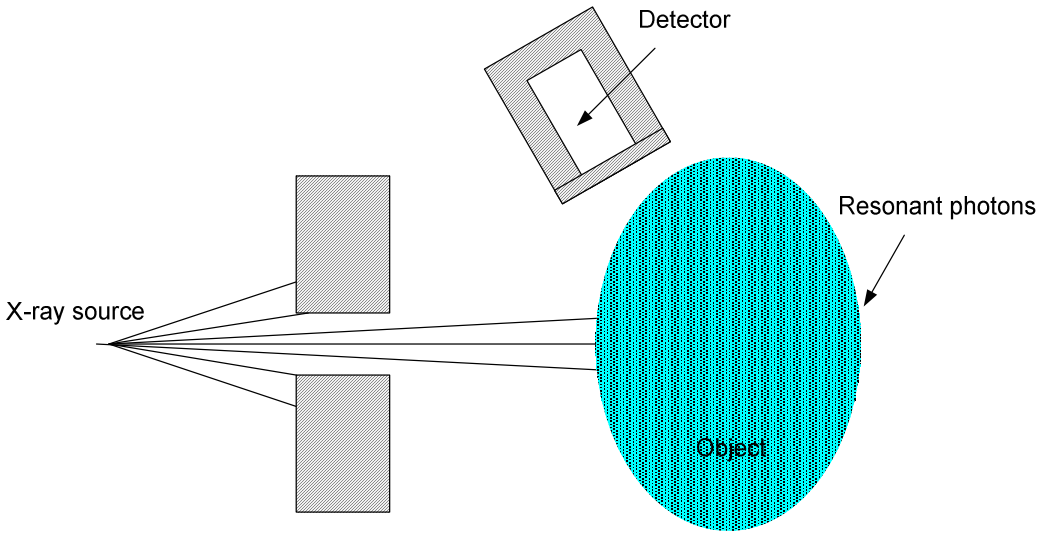

Figure 4.1 Scattering detection method using NRF

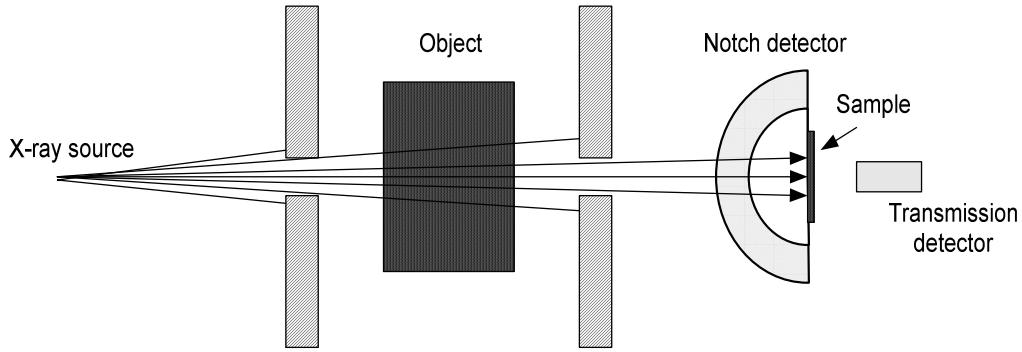

Figure 4.2 Self-absorption detection method using NRF

One feature of NRF that makes it a powerful tool for isotope identification is the sharp profile of the NRF cross section. The width of the cross section is typically of the order of 100 meV, while the peak value is 100's of barns for strongly resonant levels. The resonance will spread over an energy range of several eV owing to Doppler shifts caused by thermal motion of the nuclei, as shown later in section 4.2.3. Thus, the peak value of the cross section will be reduced to a few barns. This is usually comparable to or larger than the cross section for photo-atomic reactions. Such a distinctive resonance makes it easy to detect even a small quantity of material of interest. On the other hand, this feature also puts constraints on the implementation of the NRF technique. First, in most nuclear transitions the gamma-ray lines are very narrow (meV), and the recoil energy loss effectively separates the absorption and emission lines. Thus, the resonance condition, i.e. the required overlap between the emission and absorption lines, is hard to fulfill when the isotope used as the source of the radiation is the same as that in the scattering or absorbing materials. Since the failure to observe resonance in the first NRF experiment by Kuhn in 1929 [65], many unsuccessful attempts to find wide gamma ray lines occurred during a time period of twenty years [66-69]. Another approach, fulfilling the

resonance condition by creation of a special source (compensating recoil energy loss using a centrifuge method) was taken by Moon. He successfully observed the resonance level at 411 keV in ^{198}Hg using a ^{198}Ag source [70].

Bremsstrahlung x-rays have become a widely used excitation photon source since their discovery. Schiff first proposed using electron bremsstrahlung to detect NRF in 1946 [71], 5 years before Moon's NRF experiment. The continuous energy distribution of bremsstrahlung sources overcomes all problems caused by recoil energy loss. However, the resonance spread (on order of eV) is about one millionth of the energy spread of a bremsstrahlung source. This means that less than one-millionth of the total photon flux contributes during the excitation process when a bremsstrahlung source is used. The rest generates unwanted background and noise. The source has to be strong enough to provide significant flux in a very narrow energy range. Detectors used to measure the resonant photons have to have high energy resolution. The resonant photons are almost mono-energetic, with an energy spread (eV) thousands of times smaller than the best energy resolution that modern radiation detectors can provide (keV). These resonant photons sit on a continuous background, so the better the energy resolution of the detector, the better the signal-to-noise ratio. HPGe detectors provide the best energy resolution among commonly available radiation detectors. HPGe detectors with high detection efficiency are currently the best detectors for NRF experiments. In contrast, recently developed lanthanum halide scintillation detectors offer good energy resolution and a fast decay constant. The fast primary decay allows the application of these detectors at an event rate much higher than HPGe detectors can handle. And the energy resolution is sufficient to detect strong resonances from certain isotopes.

NRF has become a popular technique to investigate composite nuclei, because both the excitation and de-excitation processes in this method only involve the electromagnetic interaction, which is the best understood interaction in nuclear physics [71-72]. This method is capable of extracting information about excited states in nuclei, including their energies, lifetimes, and also angular momenta [73-77]. Hence, the technique has found favor among physicists studying nuclear excited states.

Excited nuclear energy levels are unique to each isotope. Energies of gamma rays emitted from these levels are often used for isotope identification. NRF seems to be an ideal tool for this with the ability to distinguish the isotope content of materials. However, despite the obvious advantage, no one has applied it in homeland security applications until recently, because of the difficulty of fulfilling the resonance condition and of obtaining reasonable signal to noise ratio in the field. Bertozzi [37-38] proposed a novel approach for applying NRF to the detection of concealed or illicit materials. His method involves exposing materials to a bremsstrahlung x-ray beam and detecting the resonantly-scattered photons, which have an energy spectrum unique to each isotope. The LINAC used in this method can produce bremsstrahlung x-rays with energies ranging from 2 MeV to 8 MeV. These interrogating photons are highly penetrating and have the potential to investigate the whole body of a cargo container. In Bertozzi's proposed design, scattered photons are measured using a segmented and collimated HPGe detector array. The intersection of the field of view of each detector with the beam forms one voxel of the total image. A complete scan could produce a map of isotope content in the entire cargo. Following this, Warren at PNNL measured NRF from ^{235}U sample [78]. Researchers at LLNL studied the performance of detection systems based on NRF to

detect specific isotopes [79]. They presented false positive/negative error rates, dose delivered to the cargo, and also the detection sensitivity of these systems. The results show a strong relationship between system performance and the properties of the interrogation photon sources. Photon sources with high intensity and a narrow energy spread show a clear advantage over traditional bremsstrahlung sources. Laser sources based on Thomson-upscattering (Inverse Compton scattering) were the most promising candidates. This class of source is available, but usually on a scale so large that they are impractical to deploy at ports [80-81]. As a result, a group at LLNL is proposing an implementation of this source type on a smaller scale [82], so that it can be deployed at seaports for homeland security purposes. Detection systems for this kind of source based on NRF techniques are also under development at LLNL [83-85].

In the present work, we have investigated detection methods based on NRF techniques. We used the 3 MeV Van de Graaff electron accelerator at the Radiation Laboratory of the University of Notre Dame as the photon source. This work showed that a newly-available fast lanthanum halide scintillation detector has an energy resolution sufficient to observe strong resonances in light materials. Their fast decay constant makes it possible to perform NRF experiments at a higher beam current, which reduces the detection time. HPGe detectors provide much better energy resolution, thus NRF spectra with good SNR (Signal to Noise Ratio). Resonance peaks were observed from various samples, including depleted uranium. These experiments and results are described later in this chapter after a discussion of the NRF physics.

4.2 Nuclear Resonance Fluorescence Cross Section

In this section, general considerations related to NRF cross sections are discussed. The formulas derived here help to understand the nature of the interaction and can be used in the estimation of interaction rates as performed in later sections. The resonance cross section is related to the width of the excited energy levels, the spin of the initial and final levels, and the excitation energy. A very narrow cross section will be broadened owing to the Doppler Effect caused by thermal motion. However, the integrated cross section remains intact. Angular distribution of the resonant photons is determined by the spin of the initial and final states.

4.2.1 Breit-Wigner Formula

The shape of the NRF cross section can be best described using the Breit-Wigner Formula [86]. For a photon of energy E, the NRF cross section, i.e. the probability to excite a nucleus from a ground state with total angular momentum J_0 to an excited state with energy E_r and total angular momentum J_1, and then de-excite to a final state with total angular momentum J_f can be written as:

$$\sigma_1^0(E) = \pi\lambda\!\!\!^{-2}\,\frac{2J_1+1}{2(2J_0+1)}\,\frac{\Gamma_0\Gamma_1}{(E-E_r)^2+\frac{1}{4}\Gamma^2}$$

where Γ is the total width of the excited state, i.e. the sum of partial widths for all possible transitions to lower states, Γ_0 is the partial width for transition from the excited state directly to the ground state, and Γ_1 is the partial width for transition to the final state. $\lambda\!\!\!^{-}$ is the wavelength of the resonant photon divided by 2π. The levels are shown in Figure 4.3.

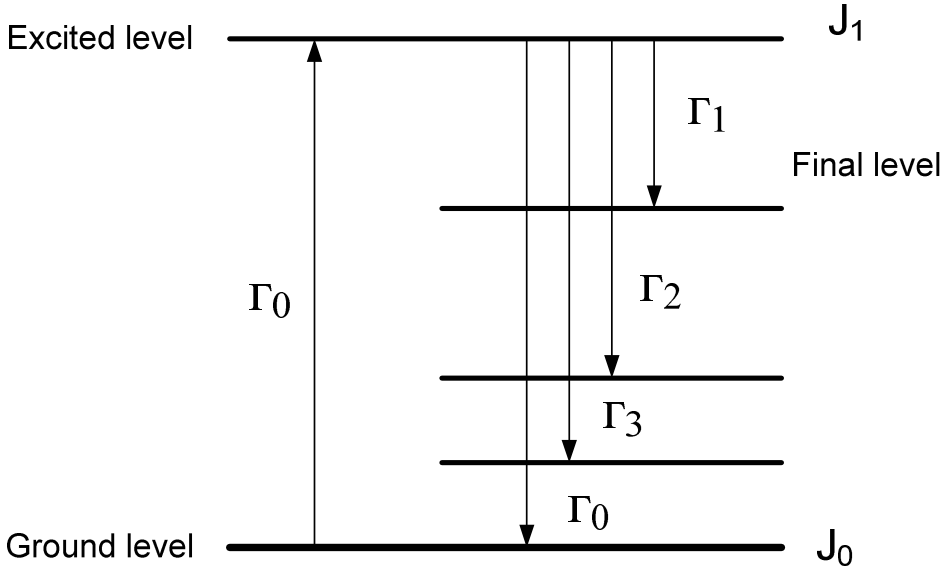

Figure 4.3 Gamma transitions inside a nucleus

Summing over all the possible transitions down from the excited level, we obtain the NRF absorption cross section for a photon with energy of E to excite level E_r

$$\sigma_{abs}^{0} = \sum_i \sigma_i^0(E) = \pi\lambda\!\!\!^{-2} \frac{2J_1+1}{2(2J_0+1)} \frac{\Gamma_0\Gamma}{(E-E_r)^2 + \frac{1}{4}\Gamma^2}.$$

In cases of pure resonance, where the only possible transition for the excited level is de-excitation to the ground level, γ_0 equals to γ, and the formula above can be re-written as

$$\sigma_{abs}^{0} = \pi\lambda\!\!\!^{-2} \frac{2J_1+1}{2(2J_0+1)} \frac{\Gamma^2}{(E-E_r)^2 + \frac{1}{4}\Gamma^2}.$$

4.2.2 Angular Distribution

The angular distribution of the resonant photons depends on the spin of the initial and final levels of the transition. The distribution can be described using the angular correlation function $W(\Theta)$ of the scattered photons with respect to the incident photon beam.

The angular distribution of photons scattered off an even-even nucleus through pure dipole transitions ($0 \rightarrow 1 \rightarrow 0$) is given as [87-88]

$$W(\Theta) = \frac{3}{4}(1 + \cos^2 \Theta)$$

For a purely quadrupole transition ($0 \rightarrow 2 \rightarrow 0$), the angular distribution can be written as

$$W(\Theta) = \frac{5}{4}(1 - 3\cos^2 \Theta + 4\cos^4 \Theta)$$

These distributions are shown in Figure 4.4. As shown in the figure, the optimal angles to measure resonantly scattered photons are different for purely dipolar (90 degrees relative to the beam axis) and quadrupolar transitions (127 degrees relative to the beam axis). Although the distribution reaches maximum on the beam axis, the resonance photons would be buried by the much stronger interrogating beam.

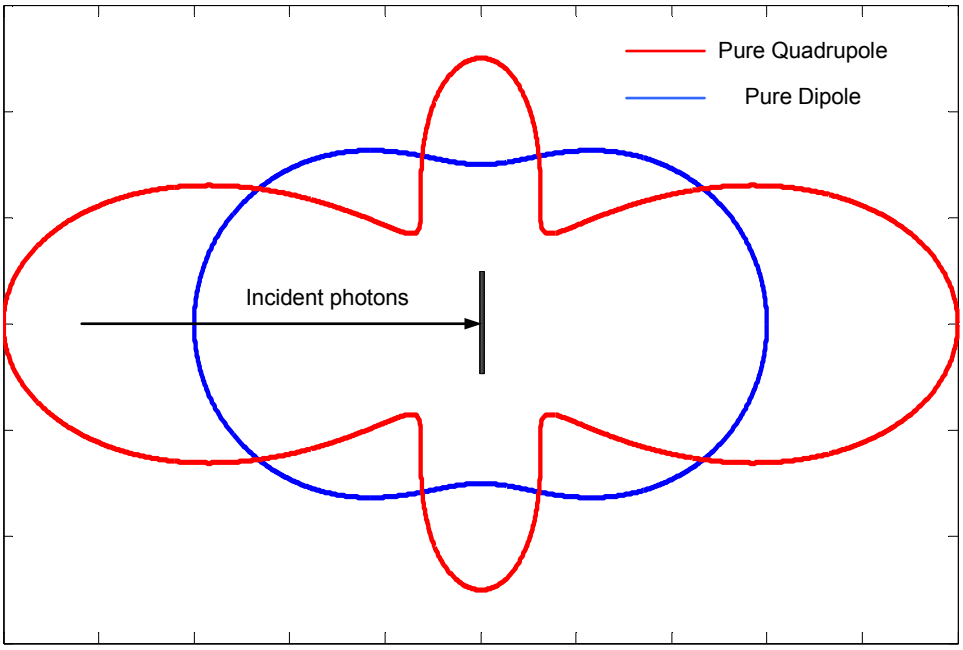

Figure 4.4 Angular distributions of resonant photons from purely dipolar and purely quadrupolar transitions

For nuclei with odd atomic mass numbers, the resonant scattering is almost isotropic [87-88].

In homeland security applications, which is primarily concerned with finding odd A nuclei, the angular distribution of resonant photons won't play a role as important as in physics experiments. But if it comes to an accurate assay, of, say, $^{238}U/^{235}U$ ratio, this distribution will have to be taken into account.

4.2.3 Doppler Effect[2]

The energy of an incident photon interacting with a nucleus varies according to the relative movement of the two. If the energy of the photon is E for a nucleus at rest,

[2] The derivation in this section follows work presented in [71] and [89]

the apparent energy to a nucleus moving towards the photon source with a velocity v is larger than E and can be written as

$$E' = E(1 + v/c)/\sqrt{1-(v/c)^2} \approx E(1 + v/c),$$

where c is the speed of light.

If the velocities of the nuclei in the material follow the Maxwell distribution function, the probability for a nucleus to have a velocity component v in the direction of the source is

$$w(v)dv = (M/2\pi kT)^{1/2} \exp(-Mv^2/2kT)dv,$$

where M is the mass of the nucleus, k is Boltzmann's constant, and T is the absolute temperature of the material.

Since the photon energy seen by a nucleus and the velocity of the nucleus have a one-to-one relationship, we can put

$$w(v)dv = w(E')dE'$$

and

$$dv = \frac{c}{E}dE'.$$

Combining these, the distribution of energies seen by the nuclei in a material for a photon with energy of E is

$$w(E')dE' = w(v)dv = (M/2\pi kT)^{1/2} \exp(-M(E'-E)^2 c^2/(2kTE^2))\frac{c}{E}dE'.$$

The Doppler width is defined as

$$\Delta = (E/c)(2kT/M)^{1/2}.$$

The above formula can then be re-written as

$$w(E')dE' = w(v)dv = (1/\Delta\pi^{1/2})\exp(-(E'-E)^2/\Delta^2)dE'.$$

In the previous section, the pure resonance NRF absorption cross section for a photon with energy E was derived as

$$\sigma_{abs}^0(E) = \sum_i \sigma_i^0(E) = \pi\lambda\!\!\!^{-2}\frac{2J_1+1}{2(2J_0+1)}\frac{\Gamma^2}{(E-E_r)^2+\frac{1}{4}\Gamma^2}.$$

The maximum of this cross section is reached when E equals E_r, giving a value

$$\sigma_{\max}^0 = \pi\lambda\!\!\!^{-2}\frac{2(2J_1+1)}{2J_0+1}.$$

Thus, the absorption cross section can be rewritten as

$$\sigma_{abs}^0(E) = \sigma_{\max}^0 \big/ \{[2(E-E_r)/\Gamma]^2+1\}.$$

When the Doppler effect is taken into account, this cross section has to be averaged over all effective energies that the nuclei see with an incident photon of energy E. We define three variables x, y, and t as follows:

$$x = 2(E-E_r)/\Gamma; \quad y = 2(E'-E_r)/\Gamma; \quad t = (\Delta/\Gamma)^2$$

Then the average of the NRF absorption cross section is

$$\sigma_D(E) = \int \sigma_{abs}{}^0(E')w(E')dE' = \sigma_{\max}^0[\frac{1}{2(\pi t)^{1/2}}]\int_{-\infty}^{\infty}\frac{\exp[-(x-y)^2/4t]}{1+y^2}dy.$$

For large values of t, the above integral can be approximated by

$$\sigma_D(E) = \int \sigma^0(E')w(E')dE' = \sigma_{\max}^0(\frac{\pi}{2t})^{1/2}\exp(-x^2/4t)$$
$$= \sigma_{\max}^0(\Gamma\pi^{1/2}/2\Delta)\exp\{-[(E-E_r)/\Delta]^2\}$$

This is the effective NRF cross section for a photon of energy E, with the Doppler broadening taken into consideration.

The assumption of t being large is usually met in reality. The typical value of Δ is on order of eV while the typical value of Γ is on order of meV. Assuming Δ = 1 eV and Γ = 1 meV, we can get the plot of σ_{abs}^{0} and σ_{D} as a function of energy. Notice the different scales in both energy and amplitude.

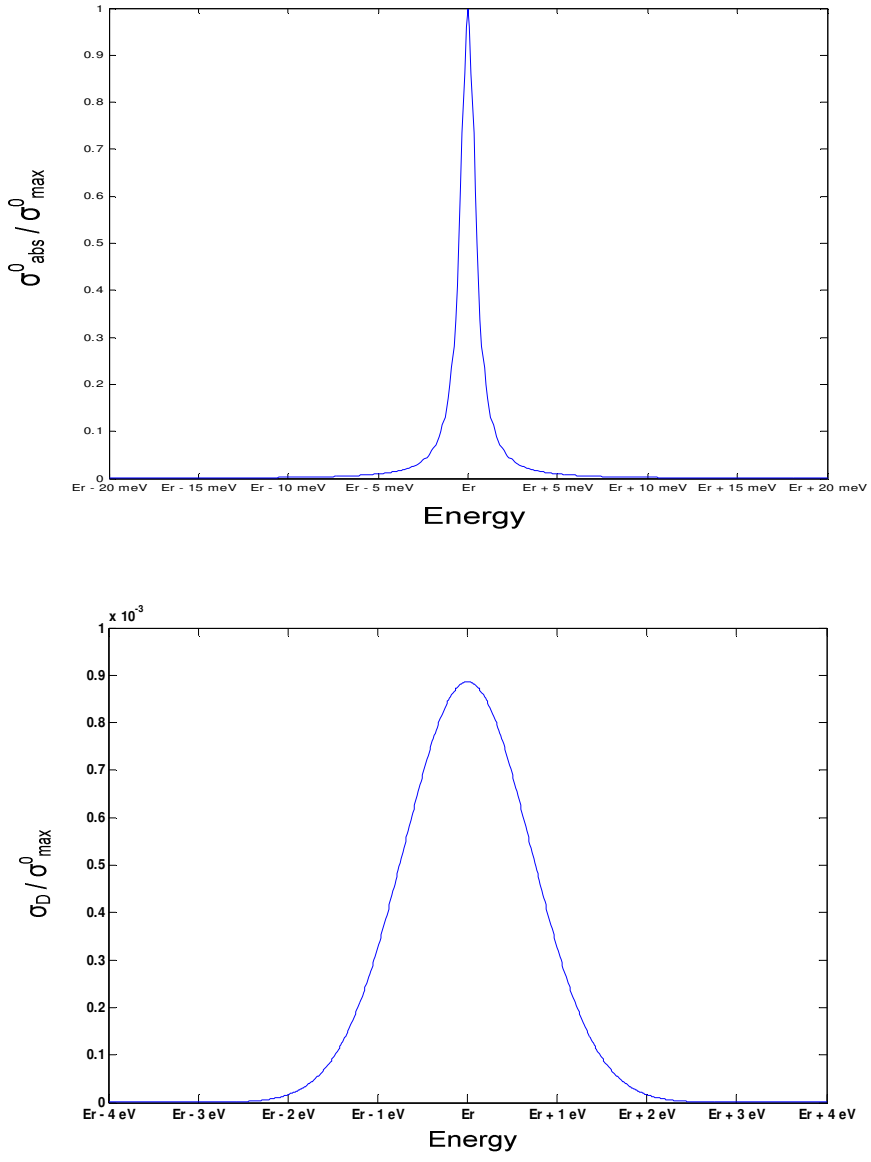

Figure 4.5 Absorption cross section before and after Doppler broadening

The integrated cross-section is defined as the integral of the cross section over the whole energy range. It can be written as

$$\int \sigma_D(E)dE = \int\int \sigma^0(E')w(E')dE'dE = \sigma^0_{\max}\int [\frac{1}{2(\pi t)^{1/2}}]\int_{-\infty}^{\infty} \frac{\exp[-(x-y)^2/4t]}{1+y^2}dydx\frac{dE}{dx}$$

From the definition of the variable x,

$$x = 2(E-E_r)/\Gamma; \quad dx = \frac{2}{\Gamma}dE,$$

$$\int \sigma(E)dE = \frac{\sigma^0_{\max}\Gamma}{2}\int [\frac{1}{2(\pi t)^{1/2}}]\int_{-\infty}^{\infty} \frac{\exp[-(x-y)^2/4t]}{1+y^2}dydx$$

The integral on the right in the above equation has the value π regardless of the value of t.

$$\int [\frac{1}{2(\pi t)^{1/2}}]\int_{-\infty}^{\infty} \frac{\exp[-(x-y)^2/4t]}{1+y^2}dydx = \pi.$$

So the integrated NRF cross-section is

$$\int \sigma_D(E)dE = \frac{\sigma^0_{\max}\Gamma\pi}{2}.$$

As can be seen here, the integrated NRF cross-section is not affected by Doppler broadening. This result is very useful in the estimation of interaction rates, because the width of the NRF effective cross-section is so narrow that in most cases the flux of the incident photon can be approximated by a constant independent of the energy in the calculation. For a thin scatter, the NRF interaction rate can be derived as

$$r = \int N\sigma_D(E)\phi(E)dE = N\phi(E_r)\int \sigma_D(E)dE = N\frac{\sigma^0_{\max}\Gamma\pi}{2}\phi(E_r)$$

where N is the number of nuclei exposed to the photon beam.

In the derivation of the effective Doppler-broadened NRF cross-section, it was assumed that the velocity of the nuclei in the absorption material follows the Maxwell distribution. This is a good assumption in gaseous materials. However, usually materials

involved in NRF experiments are solids. In his study of neutron resonance, Lamb pointed out that the effective cross-section in a solid has the same form as that in a gaseous material at a higher temperature, as long as the solid may be treated as a Debye continuum and that lattice binding is weak [90]. The ratio of the effective temperature to the actual temperature is

$$T_{eff} / T = 3(T/\theta)^3 \int_0^{\theta/T} t^3 (\frac{1}{e^t - 1} + \frac{1}{2}) dt ,$$

where θ is the Debye temperature of the solid.

4.3 Sources in Nuclear Resonance Fluorescence Experiments

The natural width of an excited nuclear level is of the order of meV. Even after Doppler broadening, the equivalent width of such a level is only several eV. Thus, only photons with energies in the local vicinity of the resonant energy contribute to the resonant excitation. One troublesome aspect of NRF is that the resonance emission occurs at sufficiently lower energy than required for absorption. This means that one cannot merely excite a sample of a material of interest and use its emissions as an interrogating source. This will be discussed below.

4.3.1 Recoil Energy Loss

When the source nuclei can be considered to be free, the recoil energy of a mass M after absorption or emission of a resonant photon of energy E_r is:

$$\Delta E = \frac{E_r^{\ 2}}{2Mc^2}$$

Thus the absorption line and the emission line are split by an energy of $2\Delta E = \frac{E_r^{\,2}}{Mc^2}$, shown in Figure 4.6. In the figure, $\frac{E_r^{\,2}}{Mc^2}$ is the energy loss due to recoil. Δ_e and Δ_r are Doppler widths for the scattering photons and the incident photons, respectively. Different symbols were used in case the source and scatterer are at different temperatures.

For energy levels of ^{238}U near 2.2 MeV, this splitting is 21.7 eV, which is much larger than the natural width of the levels (~ meV) and also larger than the Doppler width at room temperature (1.06 eV). Because of the recoil energy loss, the absorbing material is transparent to its own resonant photons. However, this also prevents a given isotope from being used as both excitation source and absorber.

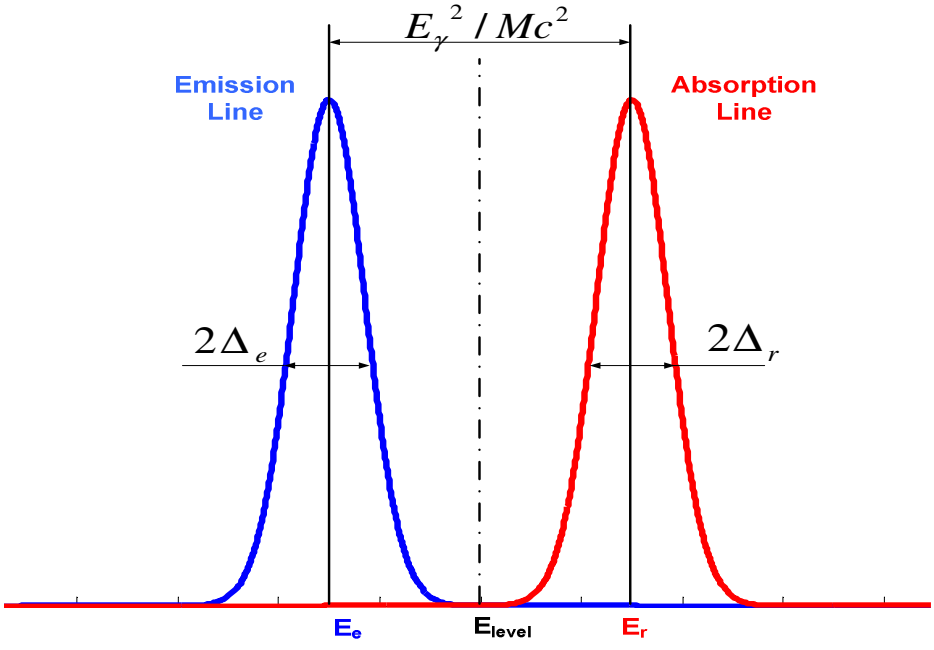

Figure 4.6 Relationship between absorption and emission lines when nuclei are free and at rest before absorption and emission.

The discussion above is based on the free recoil assumption. In order for this assumption to stand true, the binding between the nuclei has to be weak. The problem of free recoil in solid materials has been discussed by Lamb [90]. Experiments showed that this assumption is valid in most cases and it will be assumed to be true in the following.

For convenience, we separate radioactive isotope sources into two kinds. In the first kind, the mean lifetime of excited levels of the source nuclei is much longer than the time between consecutive collisions of nuclei with their surroundings. Thus, the source nuclei will be at thermal equilibrium with the surrounding particles before the emission of gamma rays. Because of energy losses due to recoil, this kind of isotope cannot serve as both source and target material in NRF experiments. The energy loss can be compensated by the centrifuge method or the thermal method discussed earlier. In the other kind of source, where the mean life of the excited level is not significantly longer than the time between consecutive collisions, emission of gamma rays happens before the nuclei reach thermal equilibrium. Some remaining momentum from previous processes leading to excited levels for the source nuclei (for example, beta decay) is left and can be helpful to compensate the energy loss due to recoil. This led to the Gordzins' successful observation of NRF using Eu_2O_3 as both source and target [91], and Burgov and Terekhov's success with ^{24}Mg [92].

Radioactive isotope sources that can excite the resonance are rare because of the recoil energy loss. Their relevance to homeland security applications is very limited.

4.3.2 Nuclear Reactions as a Source

Nuclear reactions, such as neutron capture, can serve as a source of NRF photons. In solids and liquids, the average time between consecutive collisions of atoms is on the order of ps (10^{-12} s), although this time is much longer in gaseous materials. In nuclear reactions, because of the higher excitation energies of nuclear levels, the majority of gamma transitions have half lives shorter than 10^{-14} seconds. Thus, emission of gamma rays following these reactions will happen well before the recoiling nuclei reach thermal equilibrium with the surrounding particles, and the emission line will be broadened due to the Doppler effect. The line broadening following nuclear reactions is usually orders of magnitude larger than the value of energy loss due to recoil. Thus, NRF should be easily observable using these gamma rays as an excitation photon source. In fact, the Doppler broadening is so large that the excitation of levels in other nuclei becomes possible, as some fall in the energy range covered by the emission spectrum. For example, Rasmussen used the Doppler-broadened 4.43 MeV gamma radiation from the reaction $N^{15}(p,\alpha)C^{12*}$ to measure the lifetimes of the 4.43 MeV level of C^{12} and the 4.46 MeV level of B^{11}[93].

4.3.3 Bremsstrahlung Sources

Nowadays, the most chosen excitation sources are electron bremsstrahlung x-ray sources. Bremsstrahlung x-rays have wide energy spectra, ranging from zero to the endpoint energy of the incident electrons. Thus, a single irradiation is capable of exciting multiple levels in the scatterer, as shown in Figure 4.7.

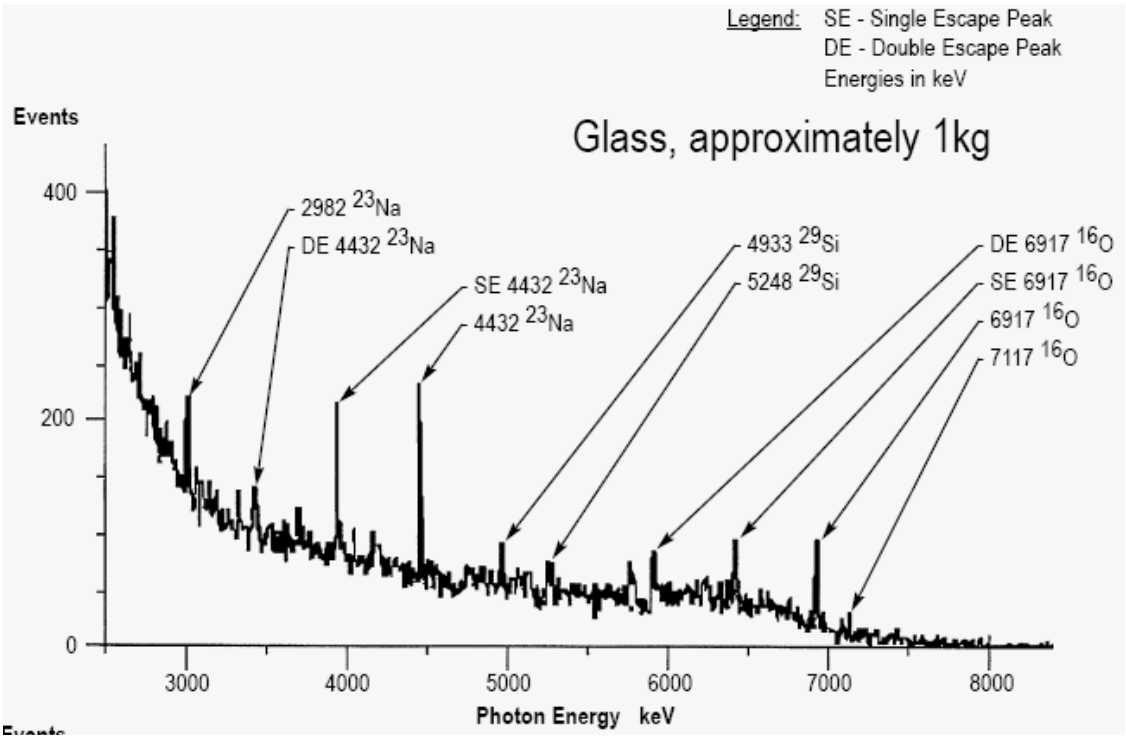

Figure 4.7 Sample spectrum of NRF from 1 kg glass [94]

In his work, Schiff confirmed the possibility of observing NRF using bremsstrahlung sources with continuous energy distributions [71]. He also pointed out the severe background problem using this kind of source. The first successful NRF experiment using bremsstrahlung x-rays was performed by Hayward and Fuller in 1957. They successfully observed the resonant photons from the 15.1 MeV level in ^{12}C using a 19 MeV electron bremsstrahlung source.

Bremsstrahlung x-ray sources are widely available these days. However, most of the electron accelerators can only work in pulse mode. A typical pulse mode LINAC can produce microsecond-wide electron pulses with a repetition rate of several hundred Hz. This equals to a duty cycle of 0.001%. Since nuclei return to ground state or lower excited states with very short half life (~10^{-14} second), resonance photons are emitted

almost immediately after the excitation. Measurement of these photons is limited to the time when the beam is active. The response time for regular spectroscopic systems is of the order of a microsecond. Thus, the maximum count rate people can get using pulse mode LINAC and traditional spectroscopic systems is usually the repetition rate of the beam [55]. Considering the huge background caused by the off-resonant photons, this counting rate is too low for time-constrained portal security applications. For this reason, bremsstrahlung sources with much higher duty cycles are desired in NRF experiments. Van de Graaff electron accelerators can work in DC mode, with a duty cycle of 100%. This helps to get a reasonable counting rate with appropriate settings. Plus, the endpoint energy of these machines can be easily adjusted. Thus, it's possible to set the endpoint energy close to the energy levels of interest. This will greatly lower the background in NRF measurements generated by the down-scattering of the high-energy photons. Recent successes in implementation of NRF techniques in homeland security applications [37-38] all chose to use Van de Graaff electron accelerators working in DC mode.

Another feature of bremsstrahlung x-ray sources worth mentioning besides duty cycle is the endpoint energy. As described earlier in this chapter, the width of the NRF cross section is of the order of eV after Doppler broadening. On the other hand, the energies of typical bremsstrahlung x-rays range from zero to several MeV. Thus, only a tiny portion of the spectrum contributes to the excitation process. Off-resonant photons bring nothing but background and unnecessary dosage. When measuring resonant photons at a backscattering angle, the main sources of the background are: 1) multiple scattered photons with higher initial energies; 2) bremsstrahlung x-rays generated by high energy electrons produced in the scattering material by incident photons; 3) elastically

scattered photons. Keeping the endpoint energy of the beam within 1 MeV of the energy levels of interest can greatly reduce the background in NRF measurements.

4.4 Detection Schemes

As mentioned in section 4.1, there are two detection schemes commonly used in NRF experiments: the scattering method and the self-absorption method. In this section, these two methods are discussed.

4.4.1 The Scattering Method

A typical experimental scattering setup is shown in Figure 4.1: the incident irradiation is tightly collimated so that nothing else but the sample is irradiated by the beam. A detector with adequate energy resolution is placed at a backscattering angle, also narrowly collimated so that it only sees the sample. When using bremsstrahlung sources, collimation and shielding are extremely important in this kind of experiment, because scattering from surrounding objects could significantly degrade the signal to noise ratio, where the enormous counting rate of off-resonant photons can saturate the detector even at a very low resonant photon flux.

As derived in section 4.2.3, the pure resonance (ground -> excited level ->ground) NRF reaction rate for a thin scatterer can be written as

$$r = \int N\sigma_D(E)\phi(E)dE = N\phi(E_r)\int \sigma_D(E)dE = N\frac{\sigma_{\max}^0 \Gamma\pi}{2}\phi(E_r),$$

where N is the number of nuclei exposed to the beam, and $\phi(E_r)$ is the flux of photons at resonant energy E_r. This reaction rate is independent of the Doppler width of the absorption line.

In cases where the excited levels de-excite to an interim level instead of the ground level, the reaction rate can be re-written as

$$r = \int N\sigma_D(E)\phi(E)dE = N\phi(E_r)\int \sigma_D(E)dE = N\frac{\sigma_{\max}^0 \pi}{2}(\frac{\Gamma_0\Gamma_f}{\Gamma})\phi(E_r),$$

where Γ_0 is the partial width for the gamma transition to the ground state and Γ_f is the partial width for the gamma transition to the interim final level.

In homeland security applications, the parameters for the gamma transition and the nuclear levels are usually well known. What the detector system ideally measures is the count rate of the emitted resonant photons. Thus, if the shape and intensity of the incident beam is known beforehand, the number of nuclei of interest exposed to the beam can be determined using the equations given above. However, there is no easy way to directly measure the energy distribution of the incident x-rays. This limits the scattering method to just detection and isotope identification, which is sufficient for this application.

The situation gets complicated when the sample can no longer be considered as a thin scatterer. This happens when $nD\sigma_D(E_r)$ is not much smaller than unity. Here, n is the particle density in the sample, D is the thickness of the sample along the beam direction, and $\sigma_D(E_r)$ is the peak value of the NRF cross section. Under these conditions, the resonant photon flux at a certain depth in the sample will differ from that at the surface, plus the shape of the beam will vary at different thicknesses as well. In order to calculate the number of nuclei of interest exposed to the beam, the isotope

content of the sample would be required. This, however, is unknown and is exactly what people are trying to measure in homeland security applications. Also, since the NRF cross section is large, resonant photons will be depleted beyond a small thickness. Material beyond this thickness makes no contribution to the resonance process, but will produce background in the measurement results.

4.4.2 Self-absorption Method

A typical self-absorption experiment is shown in Figure 4.2. A notch detector is located out of the beam and is pointed at a sample of the isotope of interest at a backscattering angle, measuring the resonant photons scattered by this sample.

In the simplest case, both the absorber and the scatterer can be considered as thin. The count rate with and without the absorber in the beam can be written as follows:
With thin absorber:

$$\begin{aligned} r(d_A) &= \int (1 - n_A d_A \sigma_{abs}(E)) \phi(E) n_S d_S \sigma_D(E) dE \\ &= \phi(E_r) \int (1 - n_A d_A \sigma_{abs}(E)) n_S d_S \sigma_D(E) dE \end{aligned}$$

Without thin absorber:

$$r(0) = \int \phi(E) n_S d_S \sigma_D(E) dE = \phi(E_r) \int n_S d_S \sigma_D(E) dE ,$$

where n_S and n_A are the particle density in the scatterer and absorber; d_S and d_A are the thickness of the scatterer and absorber in the beam direction, $\sigma_D(E)$ is the NRF cross section with Doppler broadening, and $\sigma_{abs}(E)$ is the total absorption cross section for the absorber.

The fraction change in the count rate R is defined as

$$R = \frac{r(0) - r(d_A)}{r(0)} = \frac{\int n_A d_A \sigma_{abs}(E) n_S d_S \sigma_D(E) dE}{\int n_S d_S \sigma_D(E) dE} = \frac{n_A d_A \int \sigma_{abs}(E) \sigma_D(E) dE}{\int \sigma_D(E) dE}$$

This value is independent of the resonant photon flux intensity and is proportional to the number of nuclei of interest present in the absorber.

For thick samples, the situation is much more complicated. Most systems under development for homeland security applications target mainly the detection and identification of SNM, instead of quantification [37-38, 79].

4.5 Modification of MCNP5 to Include NRF Interaction

Nuclear Resonance Fluorescence is not included in any standard Monte Carlo code up to now. To better understand the feasibility of utilizing this technique in detection of SNM for homeland security applications, an effort has been made to include this reaction in MCNP5 simulations.

There are two subroutines in the source code of MCNP5 which need to be modified to include NRF interactions in the simulation, 'photot.F90' and 'colidp.F90'. In subroutine 'photot.F90', the code reads cross section data files and gives out photon-atomic reaction cross sections (photoelectric, coherent and incoherent scattering, pair production, and total cross section) at current photon energy for each nuclide in the current cell by interpolation of values on a coarse energy grid provided by the database.

There is no complete cross section database available for NRF interactions. The NRF interaction cross section can be described very well using the Breit-Wigner formula as described in previous sections. In this modification the cross section was approximated

using a Gaussian function or a hat-top function for simplicity and reduced computational load. The calculation results were recorded and added to the value of the total cross section, shown in Figure 4.8.

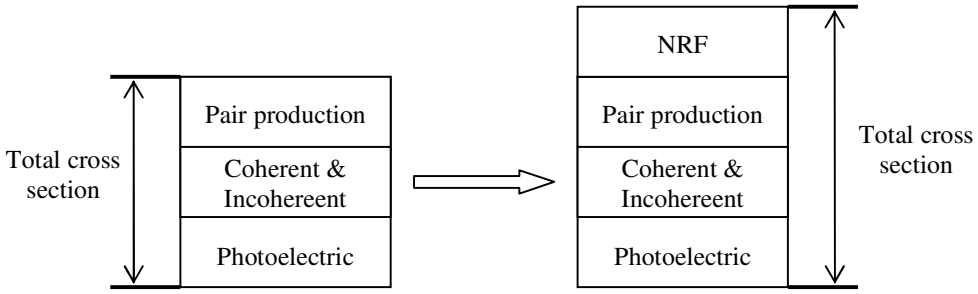

Figure 4.8 Modification of subroutine photot.F90

In subroutine 'colidp.F90', the code samples nuclides (based on total cross section) and type of interaction (based on partial cross sections). If the nuclide of interest is chosen, and the NRF reaction is sampled, the photon is re-emitted in all directions with an energy that equals the incident energy minus recoil energy loss. A few assumptions have been made here. First, the resonant photon is assumed to be emitted isotropically. This is true for odd-A nuclei, but not an accurate approximation for even-A nuclei. Second, the excited nuclei are assumed to de-excite only to the ground state. Third, the excited nuclei are assumed to reach thermal equilibrium before emission of resonant photons. In solids, this is a reasonable assumption for levels with lifetime significantly longer than 10^{-14} second. Otherwise, the emission photons will carry some memory of the preceding process leading to the excited state, i.e., absorption of incident photons in this case. To get better counting statistics, the width of the cross section peak was broadened to 1 keV from its real value around 1 eV. This would greatly decrease the computation

time without affecting the shape of the resulting spectrum, because the cross section of the photon-atomic interaction is essentially flat over this small energy range.

Simulations have been run and an obvious difference can be observed with or without the isotope of interest present in the beam. The setup of the simulation is shown in Figure 4.9 below for a self-absorption experiment.

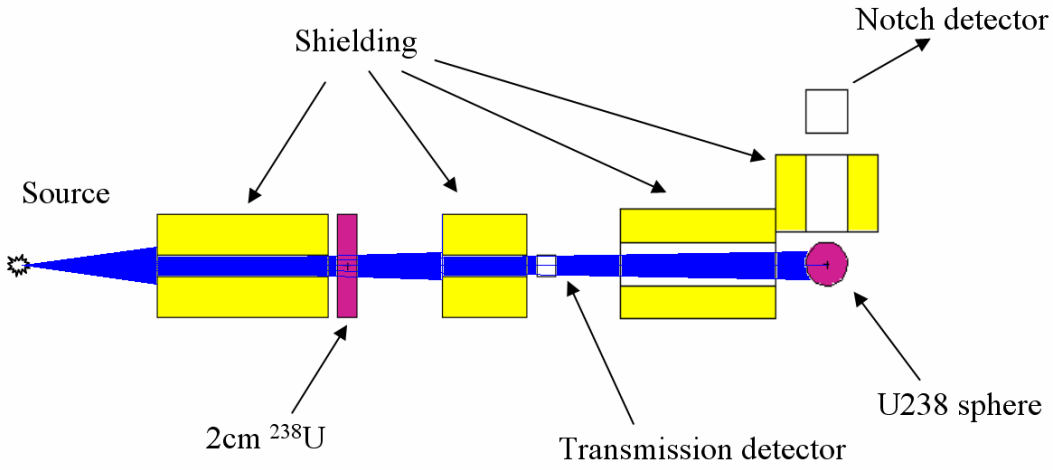

Figure 4.9 Setup of the MCNP5 simulation

Without the NRF feature enabled, we expected the transmission detector to give out a fairly flat spectrum in the energy range of interest, because in such a narrow range (around 2 MeV, several keV wide), the cross section for atomic reaction doesn't change much at all. However, with the NRF feature enabled, a notch in the transmission spectrum is expected, simply because the cross section of NRF changes abruptly within a narrow energy region. The spectra recorded by the transmission detector with or without the NRF feature enabled are shown in Figure 4.10 below.

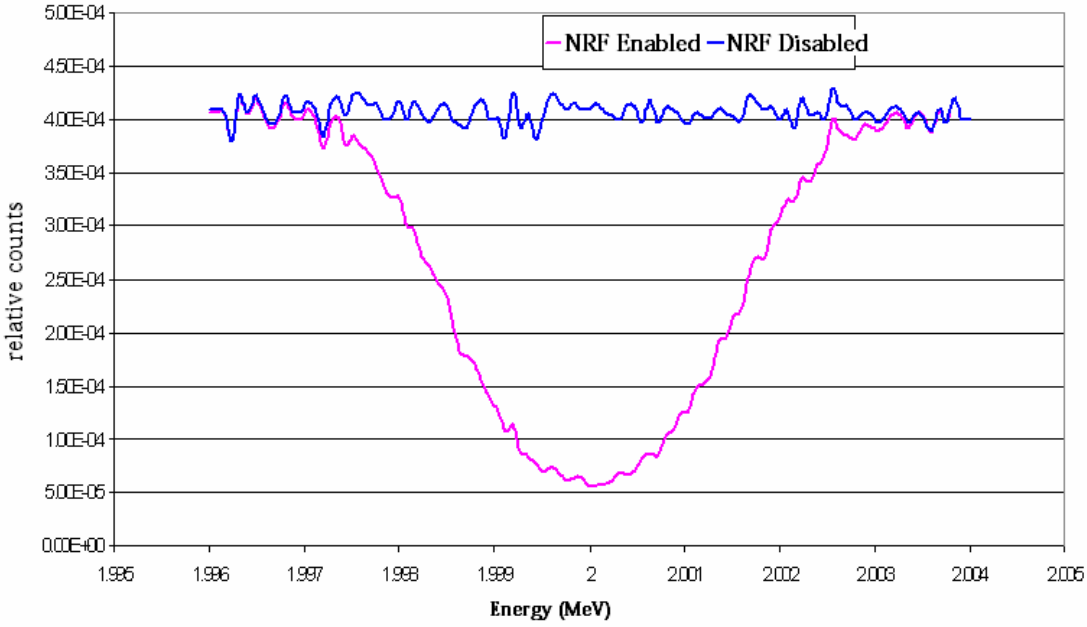

Figure 4.10 Spectra recorded by the transmission detector

If the NRF feature is enabled in the first step, a notch will be created by the 2 cm ^{238}U sample in the beam, as shown in Figure 4.10. Thus, a decrease in the count of resonant photons is expected in the notch detector. On the other hand, if no SNM was excited in the beam, the transmission spectrum would be flat, and a resonant peak should be present at the resonant energy above a very low background in the spectrum measured by the notch detector. The results of the simulation were shown below, in Figure 4.11.

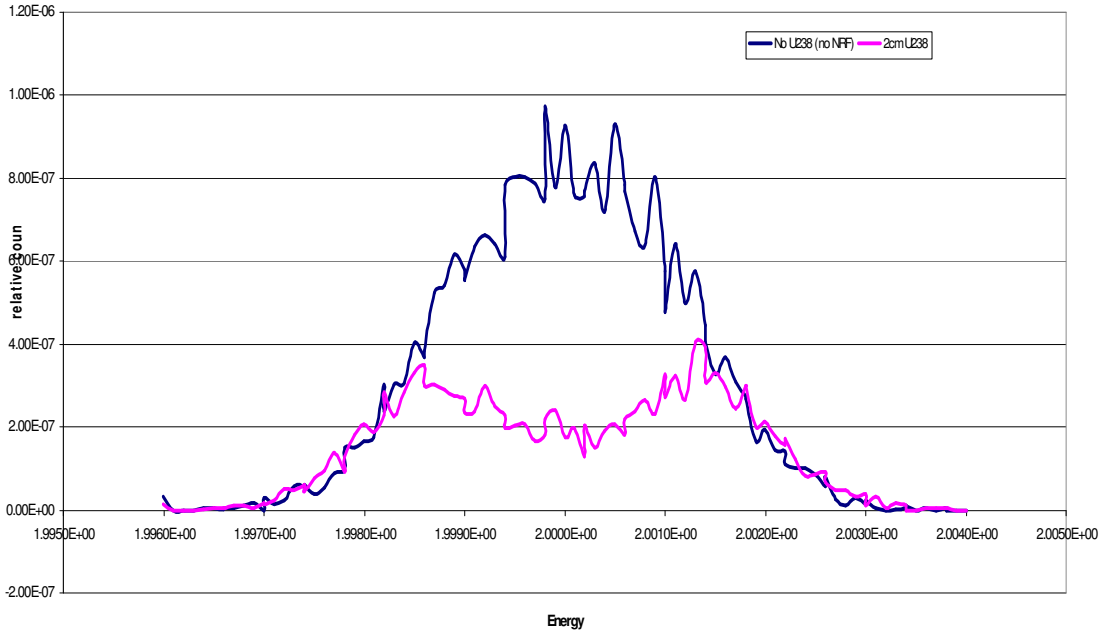

Figure 4.11 Spectra recorded by the notch detector

A more accurate treatment of the cross section can be implemented in further development. Further, a more realistic angular distribution of the scattered photons after NRF will be essential for applications relying upon the angular discrimination.

4.6 NRF Experiments

A series of NRF experiments were performed at the Radiation Laboratory of the University of Notre Dame. The lab is equipped with a Van de Graaff electron accelerator, with 100% duty cycle (DC beam) and an endpoint energy adjustable up to 3 MeV. The beam current in the DC mode can be set to as high as 200 μA. Bremsstrahlung x-rays generated by energetic electrons being stopped by a 1 mm thick tungsten converter were

used as the interrogation source in these NRF experiments. Resonant peaks from various samples were sought using both a $LaCl_3$ detector and an HPGe detector.

4.6.1 Photon Source

As discussed in section 4.3.3, in NRF experiments, high intensity, large duty cycle and adjustable endpoint energy are preferred when bremsstrahlung sources are used. Van de Graaff electron accelerators fall in this category. The machine available at the Radiation Laboratory of the University of Notre Dame is shown in Figure 4.12. The NRF experiments were set up to use the 90 degree port, marked in the picture.

Figure 4.12 3 MeV Van de Graaff electron accelerator at the Radiation Laboratory of the University of Notre Dame

This accelerator can produce an electron beam with 100% duty cycle. The energy of this beam is adjustable up to 3 MeV. The beam current in DC mode can be set as high

as 200 μA. However, it is usually set to around 100 μA in order to keep the temperature of the electron radiator low.

Unfortunately, there was a problem with the electron beam alignment (most likely caused by malfunctioning focusing magnets) when the first set of NRF experiments was performed. Instead of evenly distributing electrons over the beam cross section, the energetic electrons concentrated on two bright points, as shown in Figure 4.13. The points are so separated that the tungsten bremsstrahlung converter (1 inch by 1 inch) was not big enough to cover both of them. This caused a loss of half of the beam current. When one point was directed to hit the center of the converter, the other one hit the wall of the beam pipe and produced background. This irregular distribution of electrons across the beam cross section likely caused the MCNP simulation results to deviate from the measurement results, as shown below.

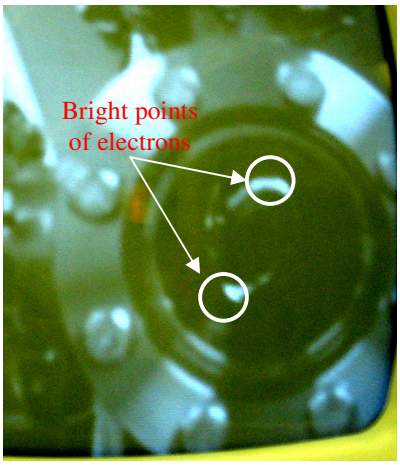

Figure 4.13 The uneven distribution of electrons across the beam cross section

A new target stage was needed to convert the energetic electrons to bremsstrahlung x-rays. In order to maximize the production of bremsstrahlung x-rays, materials with high density and high atomic number were considered for the converter.

Also, the converter needed to withstand the heat generated during the process, so the ideal material should have a high melting point as well. For machines operating with high power such as this, an additional cooling system was deemed necessary. Tungsten is a widely used material for a bremsstrahlung converter. It has a density of 19.25 g/cm^3 and a high atomic number of 74. The melting point of tungsten is 3695 K.

The bremsstrahlung converter needed to be thick enough to stop virtually all the 3 MeV electrons. Otherwise, ozone will be produced in the test hall. The simulation result of electron tracks in tungsten using CASINO code [95] is shown in Figure 4.14. Based on the simulation results, a 1 mm thick tungsten slab is sufficient to stop the 3 MeV electrons.

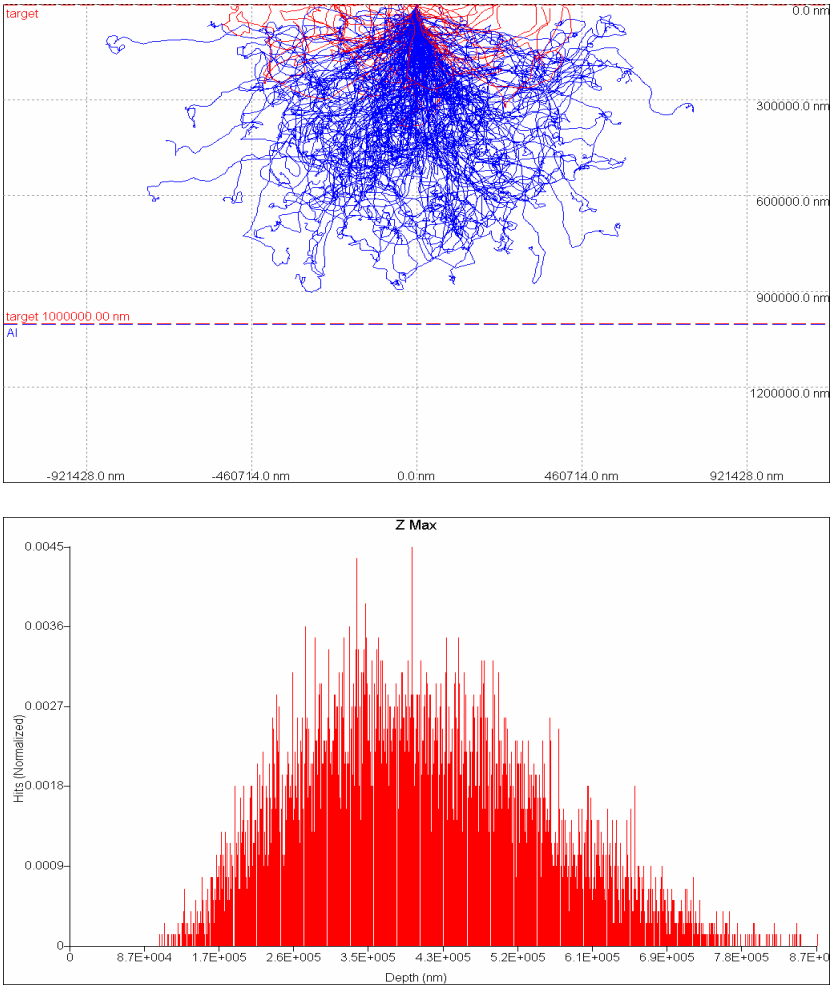

Figure 4.14 The simulation result of 3 MeV electron tracks in tungsten and the histogram for electron penetration depth

The target stage needed to be able to dissipate the heat generated during the bremsstrahlung process. Assuming the beam current is set to 100 μA and the beam size is 1 cm by 1 cm, the power delivered onto the converter by the beam is 300 W/cm^2, if all the energy is deposited in form of heat. Since bremsstrahlung x-rays will carry some energy out, this is a conservative estimate. In order to dissipate this heat, a water cooling system was implemented in the target stage design. The design is shown below in Figure 4.15. Cooling water was passed through the u-shaped cooling pipe during the

experiments to keep the base cool. Nitrogen was used to sweep oxygen out of the gap between the tungsten target and the beam window, in order to reduce ozone production.

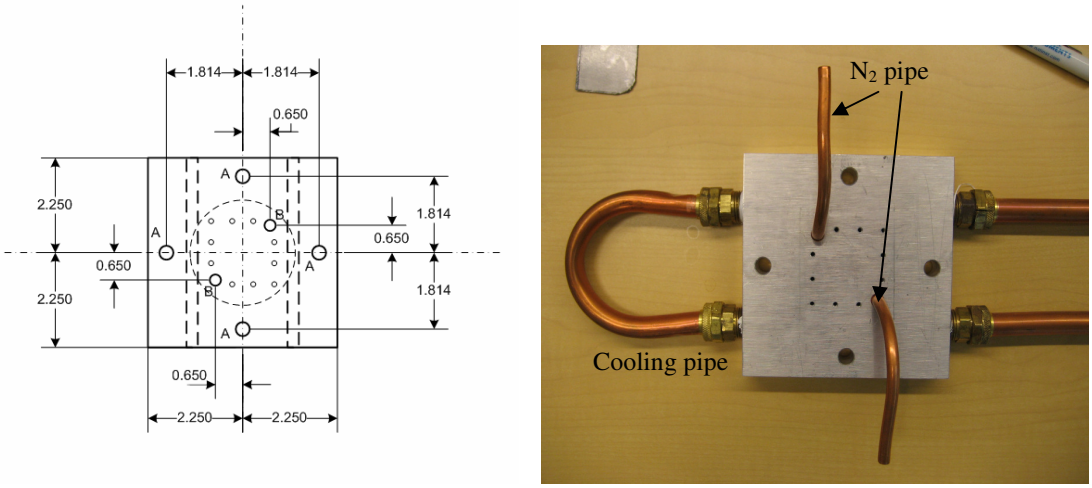

Figure 4.15 Target stage and the design drawing (unit: inch)

The cooling capability of this design was calculated using COMSOL [96]. The results are shown below in Figure 4.16. Assuming the temperature of the cooling water is 300 K and the rate of flow is 5 m/s in the pipe, the calculation predicted a maximum temperature of 380 K at the center of the converter. The calculation also showed no sign of deformation damage.

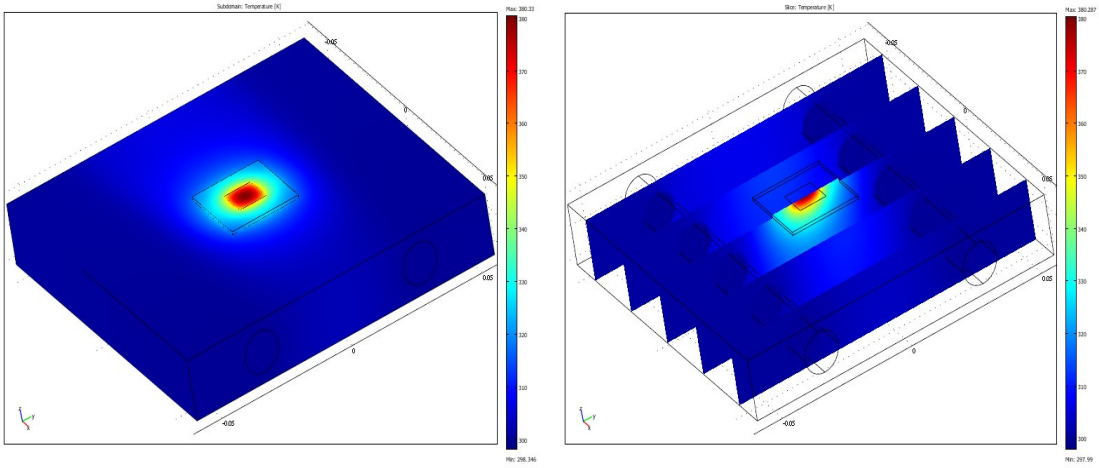

Figure 4.16 Temperature distribution calculated using COMSOL

A MCNP5 simulation was performed to estimate the flux of resonant photons produced by this target stage. The setup of the simulation is shown below in Figure 4.17.

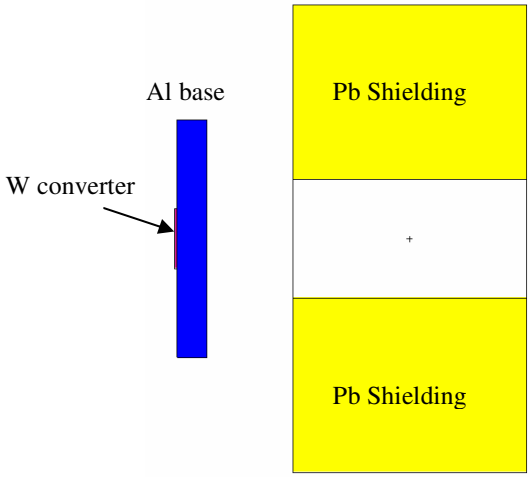

Figure 4.17 MCNP5 simulation of the target stage

The size of the electron beam was assumed to be 1 cm^2. Simulation results predicted that the flux on the beam axis at a distance of 22 inches from the converter is $3.2\times10^2/(eV\cdot cm^2\cdot s)$ at 2.1-2.2 MeV.

4.6.2 Detectors

In the experiments performed at the Radiation Laboratory of the University of Notre Dame, two detectors were used to measure resonant photon spectra: a 1.5 inch by 1.5 inch $LaCl_3$ scintillation detector and an HPGe detector with 90% relative detection efficiency compared to a 3 inch by 3 inch NaI detector.

The $LaCl_3$ scintillation detector has a very fast decay constant of 28 ns. Together with the digital spectroscopic systems described in Chapter 3, it can measure energy spectra at a counting rate as high as 10^6 cps with no dead time and little degradation of energy resolution, as shown in section 3.2.3. However, because of its small size, this $LaCl_3$ scintillation detector has fairly low detection efficiency. Its volume is only 1/8 of that of a 3 inch by 3 inch NaI detector. Thus, the solid angle it occupies is ¼ of what a 3 inch by 3 inch NaI would have at the same distance. An MCNP5 simulation showed that the intrinsic total efficiency falls to about 60 % of what it is for a 3 inch by 3 inch NaI detector for photons with energy around 2 MeV. The energy resolution of the $LaCl_3$ detector (4% at 662 keV) is high compared with other scintillation detectors, e.g. NaI detectors (6% at 662 keV). However, this resolution is a significantly worse than the ~0.2% HPGe detectors can provide. In NRF experiments, since the resonant photons have a very narrow energy spread while the background noise is continuous, signal to noise ratio (SNR) is inversely proportional to the energy resolution of the detector. Thus,

the spectra measured by the $LaCl_3$ detector will have a SNR which is worse than that measured by HPGe detectors. In homeland security applications, the SNR is directly related to the measurement time required to achieve a certain false positive/negative error rate [79]. Thus, a degraded SNR means that a longer measurement time is required if a certain error rate is to be achieved.

On the other hand, HPGe detectors offer the best energy resolution among commonly available photon detectors. The one used in our NRF experiments is the ORTEC GEM90. It offers a relative detection efficiency of 90% when compared to a 3 inch by 3 inch NaI detector. The energy resolution is claimed to be 2 keV at 1.33 MeV. However, the best resolution that was obtained with our unit is 3.2 keV at 1.33 MeV, shown in Figure 4.18 below.

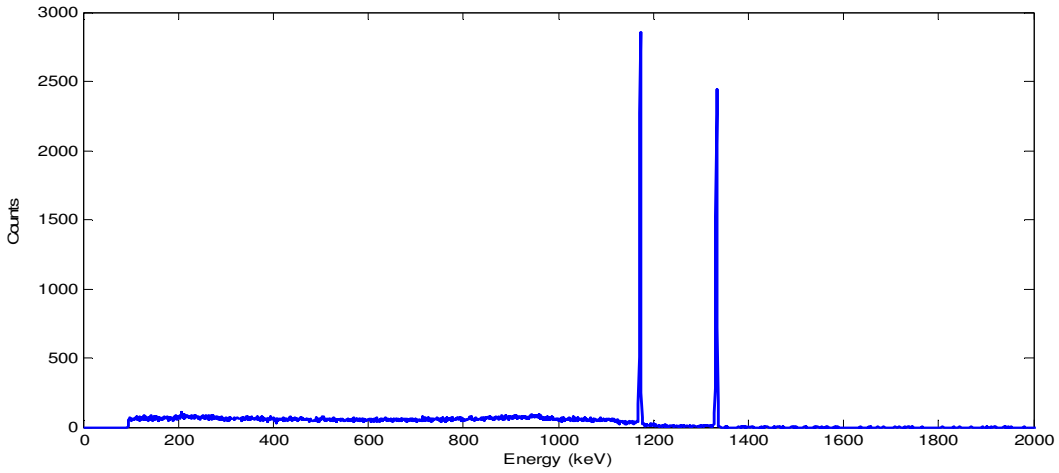

Figure 4.18 Co-60 gamma ray spectrum measured with an ORTEC GEM90 detector. The energy resolution at 1.33 MeV is 3.2 keV

The disadvantage of using HPGe detectors in NRF experiments is the slow processing time for each event. Since the shape of the output signal from the HPGe detectors varies according to the interaction position, the time constant of the shaping amplifiers used with HPGe detectors is usually set to a value close to the maximum of the charge collection time, which is of the order of a microsecond for a crystal as big as the GEM90. Plus, conventional spectroscopic systems usually have a processing time of several microseconds following each event. With the pile-up rejection feature enabled, this limits the maximum throughput rate to less than 10^5 cps. In addition, the energy resolution (FWHM) of HPGe detectors rises roughly linearly with the count rate up to around 10^5 Hz [97]. As discussed above, good energy resolution is essential in NRF experiments. In order to get an adequate SNR, a common rule is to keep the dead time below 10% in each measurement. This results in a maximum counting rate of 10^4 cps for our system (ORTEC GEM90 detector and ORTEC 926 MCA).

4.6.3 Scattering Experiments

A series of scattering experiments was performed at the Radiation Laboratory of the University of Notre Dame, using both the $LaCl_3$ detector and the HPGe detector described in the previous section. Resonant peaks from various samples were sought.

4.6.3.1 Scattering Experiments using a $LaCl_3$ detector

The schematic of the experimental setup is shown below in Figure 4.19.

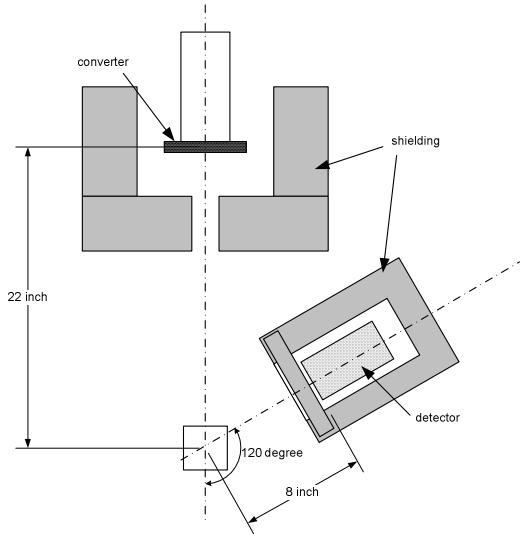

Figure 4.19 Schematic for the scattering experiments using $LaCl_3$ detector

In these experiments, the bremsstrahlung x-rays generated by the 3 MeV Van de Graaff accelerator were collimated down to a 2 by 2 inch beam. The scatterer is located in the beam, 22 inches away from the bremsstrahlung converter. The $LaCl_3$ detector is shielded by 8 inches lead on each side, and 6 inches on top and bottom. A 1 inch thick lead sheet was put in front of the detector to block low-energy photons. Power supply and signal wires ran through the back of the detector shielding. The shield in the backward direction was 4 inches of lead. The detector was located 8 inches from the scatterer, at a backscattering angle of 120 degree, as shown in Figure 4.17. Pictures of the actual setup are shown in Figure 4.20.

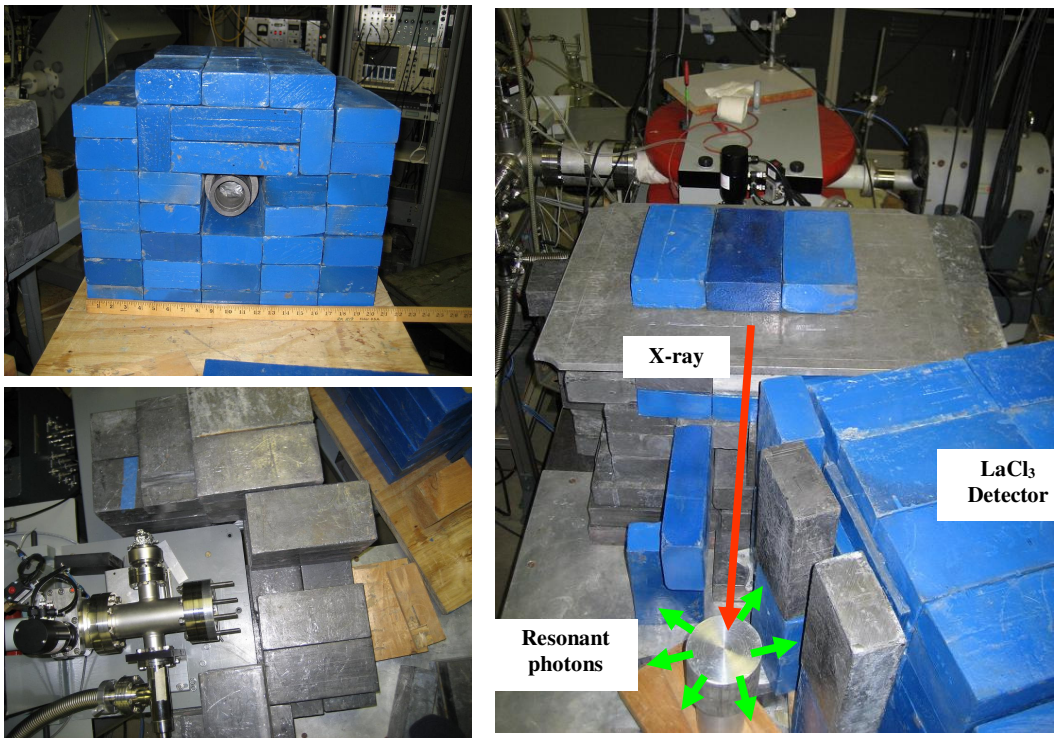

Figure 4.20 The actual setup for the scattering experiments using a $LaCl_3$ detector.

The spectroscopic system used in these experiments includes a pre-amplifier (ORTEC 113), a shaping amplifier (ORTEC 571), and a Multi-Channel Analyzer (AMPTEK MCA-8000A). The input capacitance of the pre-amplifier was set to 0 pF. The shaping time of the shaping amplifier was set to 1 μs. The coarse gain was set to 100 and the fine gain was set to 0.7.

The beam current was chosen to be 120 μA in these experiments. With the shielding configuration described above, dead time in the spectroscopic system was less than 10 % even for a dense scatterer like our 109 g depleted uranium rod.

A. NRF experiments with BN sample using the $LaCl_3$ detector.

The first set of experiments was performed to investigate the 2.12 MeV level in ^{11}B. The 2.12 MeV level in ^{11}B has a half life of 3.8 fs (i.e., a width of 173.2 meV) and a total angular momentum of -1/2. The peak NRF absorption cross section for the magnetic dipole transition between the ground level (angular momentum = -3/2) and the 2.12 MeV level can be calculated using the Breit-Wigner formula, as discussed in previous sections.

$$\sigma_{\max}^{0} = 2\pi\hat{\lambda}^2 \frac{2J_1+1}{(2J_0+1)} = 2\pi\left(\frac{0.0058\,\mathring{A}}{2\pi}\right)^2 \frac{2\times 1/2+1}{2\times 3/2+1} = 267.7\,barn$$

The integral cross section is

$$\int \sigma_D(E)dE = \frac{\sigma_{\max}^{0}\Gamma\pi}{2} = 72.83\,barn\cdot eV$$

The Doppler width at room temperature for the ^{11}B sample can be calculated as follows:

$$\Delta = \frac{E}{c}\sqrt{\frac{2kT}{M}} = \frac{2.12\,MeV}{c}\sqrt{\frac{2\times 26\,meV}{11\times 1.67\times 10^{-27}\,kg}} = 4.96\,eV\,.$$

Thus the shape of the cross section can be approximated using a top hat function with an amplitude σ_D = 7.34 barn (= $72.83\,barn\cdot eV/(2\Delta)$) and a width of 9.92 eV (= 2Δ), shown below in Figure 4.21.

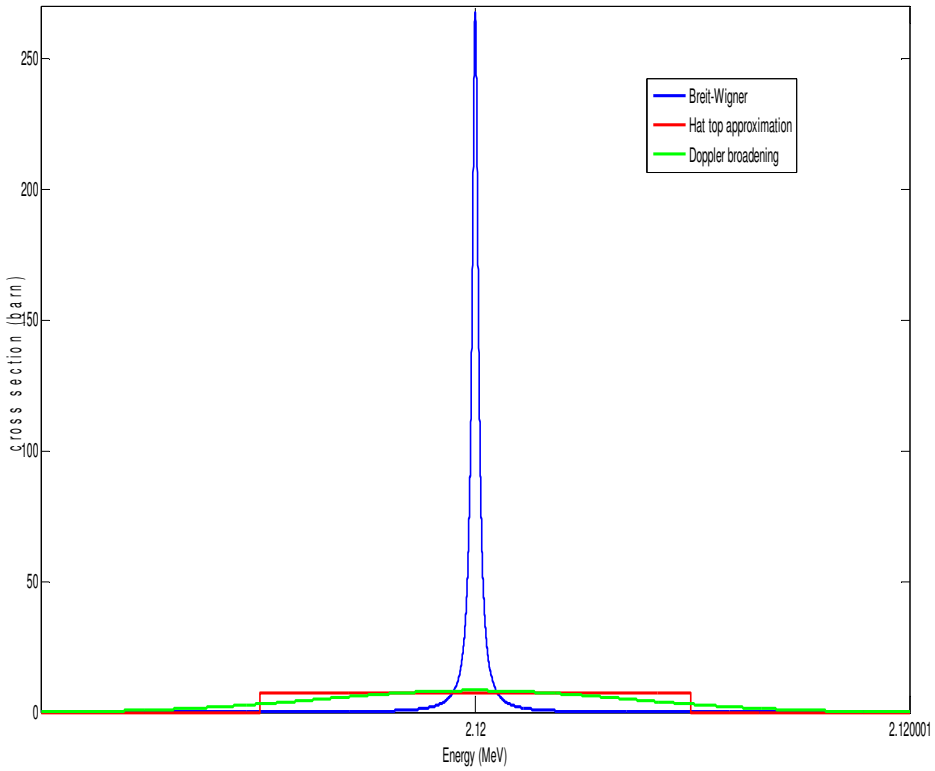

Figure 4.21 ^{11}B NRF cross section before (blue), after (green) Doppler broadening and the top hat approximation (red).

The total photon-atomic cross section in BN was estimated to be 1.78 barn at 2.12 MeV [98]. Thus, the NRF interaction dominates in the vicinity of the resonant energy, as we show next.

The scatterer used in this experiment was a 2×2×3 inch BN sample. The density of the BN sample is 1.9 g/cm^3, and the natural abundance of ^{11}B is 80%. Thus, the number of ^{11}B nuclei contained in this sample is 1.0×10^{25}. The attenuation coefficient for NRF interactions can be calculated as

$$\tau_{res} = \rho_{^{11}B}\sigma_D = 0.27cm^{-1},$$

where $\rho_{^{11}B}$ is the particle density for ^{11}B in the sample, and σ_D is the amplitude of the Doppler broadened NRF cross section. In comparison, the attenuation coefficient for atomic interactions can be calculated as

$\tau_t = \rho_{BN}\sigma_t = 0.08\,cm^{-1}$, about a factor of 3 smaller than NRF.

For a 2 inch thick sample, the probability for a resonant photon to escape without NRF interactions or atomic interactions is

$$p_e = \exp(-(\tau_{res} + \tau_t)d) = 0.17\,.$$

Since the beam size was collimated down to 2×2 inches, the interaction rate in the sample is estimated to be

$$\begin{aligned}\dot{R} &= \phi \cdot 2\Delta \cdot S(1 - p_e)\frac{\tau_{res}}{\tau_{res} + \tau_t} \\ &= 3.2\times10^2\,/(eV \cdot cm^2 \cdot s)\times 2 \times 4.96\,eV \times 4\,inch^2 (1-0.17)\frac{0.27}{0.27+0.08} \\ &= 5.2\times10^4\,/\,s\end{aligned}$$

If some degree of beam divergence at the tangent existed, the actual beam current ϕ would be lower than the value used in the above equation. This makes the reaction rate given here an overestimation.

Here, absorption by photon-atomic interactions was ignored, since the NRF interaction dominates for resonant photons, as discussed above. The resonant photon flux is taken from the simulation mentioned in section 4.5.1.

The solid angle occupied by the $LaCl_3$ detector is:

$$\Omega = \frac{S}{d^2} = 0.0088\pi\,.$$

The attenuation of resonant photons by the 1 inch lead window is:

$$\exp(-\mu t) = \exp(-11.3\ g/cm^3 \times 4.6\times10^{-2} cm^2/g \times 2.54cm) = 0.27,$$

where the value for the attenuation coefficient is taken from reference [98].

The intrinsic peak efficiency for a 1.5×1.5 inch $LaCl_3$ detector was estimated to be $\varepsilon_{ip} = 0.05$ near 2 MeV, based on an MCNP5 simulation.

Thus, the predicted counting rate under the resonant peak is

$$\dot{r} = \dot{R}\frac{\Omega}{4\pi}\varepsilon_{ip}\exp(-\mu t) = 5.2\times10^4 \times \frac{0.0088\pi}{4\pi} \times 0.05 \times 0.27 = 1.5\ cps.$$

Some assumptions made in the foregoing derivation are:

1) The resonant photons are emitted isotropically. This is a reasonable assumption for nuclei with odd atomic number.

2) No attenuation of resonant photons in the sample was considered.

A Monte Carlo simulation was performed using our modified version of MCNP5 to predict counting rate in the detector as well. The incident photons were assumed to be evenly distributed in an energy range from $E_r - 10eV$ to $E_r + 10eV$, where E_r is the resonant energy. Further, the photons are assumed to be distributed evenly over a 2×2 inch beam cross section. The NRF cross section was approximated using the top hat shape shown in Figure 4.21. Simulation showed that the probability for these photons to be recorded in the detector is 8.6×10^{-6}. The resonant photon flux was estimated to be $3.2\times10^2/(eV\cdot cm^2\cdot s)$ from the simulation described in section 4.5. Thus, the interaction rate can be calculated as

$$\dot{r}' = 8.6\times10^{-6} \times 3.2\times10^2/(eV\cdot cm^2\cdot s) \times 20eV \times 4inch^2 = 1.4\ cps$$

This value is very close to the estimation given by the analytical method above.

Two 40-minute measurements were performed. One measurement was made with the BN sample in the beam and the other without. The results are shown below in Figure 4.22.

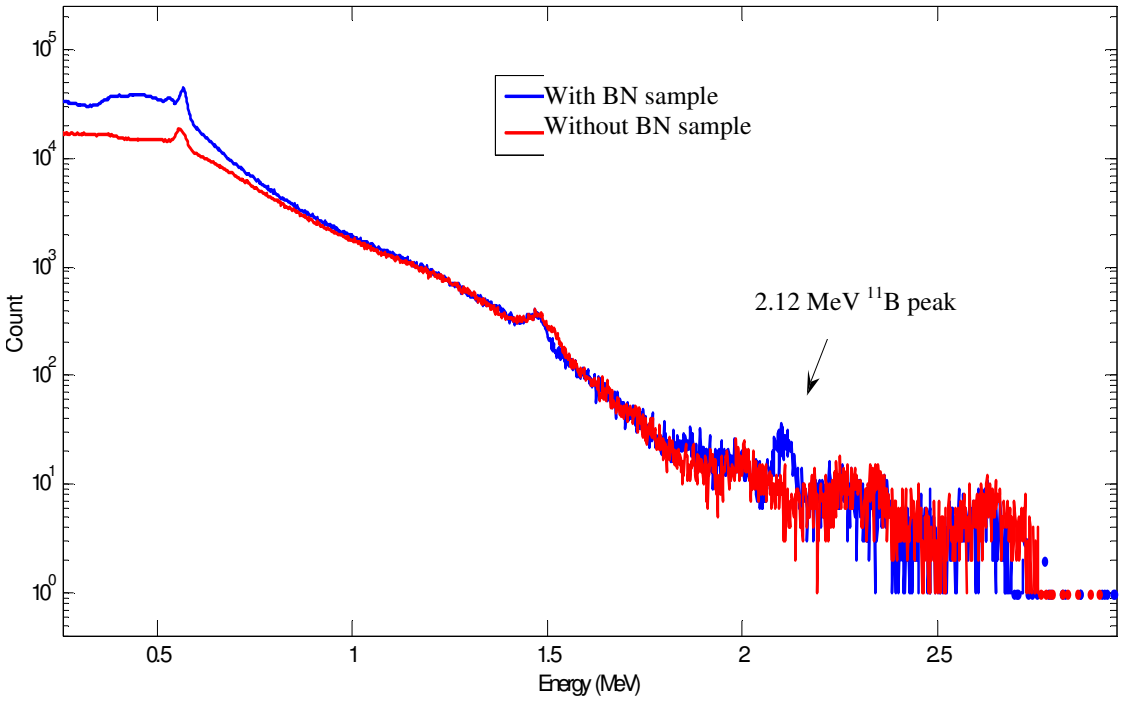

Figure 4.22 Measurement results from NRF experiments using a BN sample.

The 2.12 MeV resonant peak from NRF of the ^{11}B nuclei stands out clearly from the background. The total count rate was about 5000 cps for both measurements. The dead time for these measurements was less than 3%. The net rate under the photopeak was measured to be 0.19 ± 0.01 cps. The signal to noise ratio was 2.27.

As observed here, the measured counting rate is significantly smaller than the prediction given by either the analytical method or the Monte Carlo method. The primary reason is likely the inaccurate modeling of the electron beam in both methods, as described earlier in section 4.6.1 and which accounts for a factor of ~2. Another possible

reason is the beam depletion inside the BN sample. The flux of the resonance photon decreases rapidly along the beam path inside the sample. The MCNP simulation gave the average flux on the front side of the sample. And the equation used above assumes a thin sample geometry. These could have overestimated the reaction rate and account for a factor of ~4. More accurate estimation can be achieved by simulating resonant photon flux as a function of depth inside the sample and using a thick sample model to calculate the reaction rate. The hump around 1.5 MeV and the structure above 2 MeV are produced by the inherent radioactivity of the $LaCl_3$ crystal. High energy radiations (gamma rays, alpha particles) emitted by impurities in the $LaCl_3$ crystal [99] add background counts to those from multiple scattering, coherent scattering, and bremsstrahlung of high energy electrons generated in the sample by the incident x-rays.

In summary, the results given by the analytical method and the Monte Carlo method are close. This confirms that absorption of the resonant photons after de-excitation, which is not included in the analytical method, is not significant in our relatively small samples. Although the predicted count rate was substantially below what was expected, the NRF peak could be clearly seen using the $LaCl_3$ detector and conventional pulse processing equipment.

B. NRF experiments with Al sample using the $LaCl_3$ detector

This set of experiments was performed to investigate the 2.21 MeV level in ^{27}Al. The 2.21 MeV level in ^{27}Al has a half-life of 26.4 fs (i.e. a width of 24.9 meV) and a total angular momentum of +7/2. The transition between this level and the ground level (angular momentum = +5/2) is a blend of magnetic dipole and electric quadrupole

processes. The peak NRF absorption cross section can be calculated using the Breit-Wigner formula as discussed in previous sections.

$$\sigma_{\max}^{0} = 2\pi\lambda\!\!\!^{-2}\frac{2J_1+1}{(2J_0+1)} = 2\pi\left(\frac{0.0056\,\mathring{A}}{2\pi}\right)^2\frac{2\times 7/2+1}{2\times 5/2+1} = 665.5\,barn\,,$$

and the integral cross section is

$$\int \sigma_D(E)dE = \frac{\sigma_{\max}^{0}\Gamma\pi}{2} = \frac{665.5barn\times 24.9meV\times\pi}{2} = 26.03\,barn\cdot eV\,.$$

The Doppler width at room temperature for the ^{27}Al sample can be calculated as follows:

$$\Delta = \frac{E}{c}\sqrt{\frac{2kT}{M}} = \frac{2.21MeV}{c}\sqrt{\frac{2\times 26meV}{27\times 1.67\times 10^{-27}kg}} = 3.3\,eV\,.$$

Thus, the shape of the cross-section can be approximated using a top hat function with an amplitude of 3.94 barn ($=26.03\,barn\cdot eV/(2\Delta)$) and a width of 6.6 eV, shown as follows in Figure 4.23.

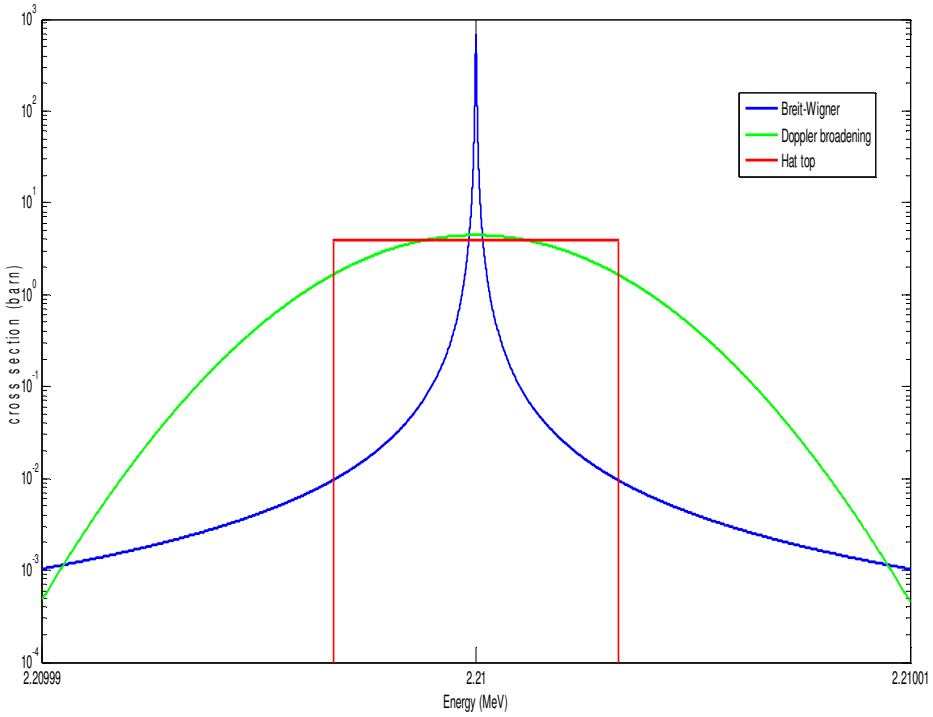

Figure 4.23 ^{27}Al NRF cross section before (blue), after (green) Doppler broadening and the top hat approximation (red).

The total photon-atomic cross section in a natural aluminum sample was estimated to be 1.95 barn at 2.21 MeV [98]. The NRF interaction cross section is comparable to that of the photon-atomic interaction, but does not dominate as in the BN sample, shown in Table 4.1.

Table 4.1 Comparison of photon atomic interaction vs. NRF interaction near the resonant energies in BN and Al samples.

	Photon atomic cross section at resonant energy (barn)	NRF cross section after Doppler broadening (top hat approximation) (barn)
BN	1.78	7.34
Al	1.95	3.94

The scatterer used in this experiment was a 3×3 inch Al cylinder. The density of the Al sample is 2.7 g/cm^3, and the natural abundance of ^{27}Al is 100%. Thus, the number of ^{27}Al nuclei contained in this sample is 2.1×10^{25}.

The attenuation coefficient for NRF interactions can be calculated as

$$\tau_{res} = \rho\sigma = 2.1\times10^{25}/(\pi\times(1.5")^2\times3")\times3.94\,barn = 0.24\,cm^{-1}.$$

The attenuation coefficient for photo-atomic interactions can be calculated as

$$\tau_{atom} = \rho\sigma_{atom} = 2.1\times10^{25}/(\pi\times(1.5")^2\times3")\times1.95\,barn = 0.118\,cm^{-1}.$$

For a 3 inch thick sample, the probability for a resonant photon to escape without an NRF interaction or a photo-atomic interaction with ^{27}Al nuclei is

$$p_e = \exp(-(\tau_{res}+\tau_{atom})d) = 0.065.$$

The net interaction rate of resonant photons for the 2×2 inch beam is

$$\begin{aligned}\dot{R} &= \phi\cdot 2\Delta S(1-p_e)\frac{\tau_{res}}{\tau_{atom}+\tau_{res}}\\ &= 3.2\times10^2/(eV\cdot cm^2\cdot s)\times6.6\,eV\times4\,inch^2\times(1-0.065)\times\frac{0.24}{0.24+0.118}\\ &= 3.4\times10^4/s\end{aligned}$$

Following the same route as for the BN sample, the predicted counting rate under the resonant peak is

$$\dot{r} = \dot{R}\frac{\Omega}{4\pi}\varepsilon_{ip}\exp(-\pi t) = 1.01\,cps.$$

A similar Monte Carlo simulation was performed to predict the counting rate in the detector as well. Simulation showed that the probability for these photons to be recorded in the detector is 7.2×10^{-6}. The resonant photon flux was estimated to be

$3.2\times10^{2}/(eV\cdot cm^{2}\cdot s)$ from our earlier simulation. Thus, the detector photopeak count rate can be calculated as

$$\dot{r}' = 7.2\times10^{-6}\times3.2\times10^{2}/(eV\cdot cm^{2}\cdot s)\times20\,eV\times4inch^{2} = 1.17\ cps\,.$$

Two 40-minute measurements were performed. One measurement was with the Al sample in the beam and the other without. The results are shown below in Figure 4.24.

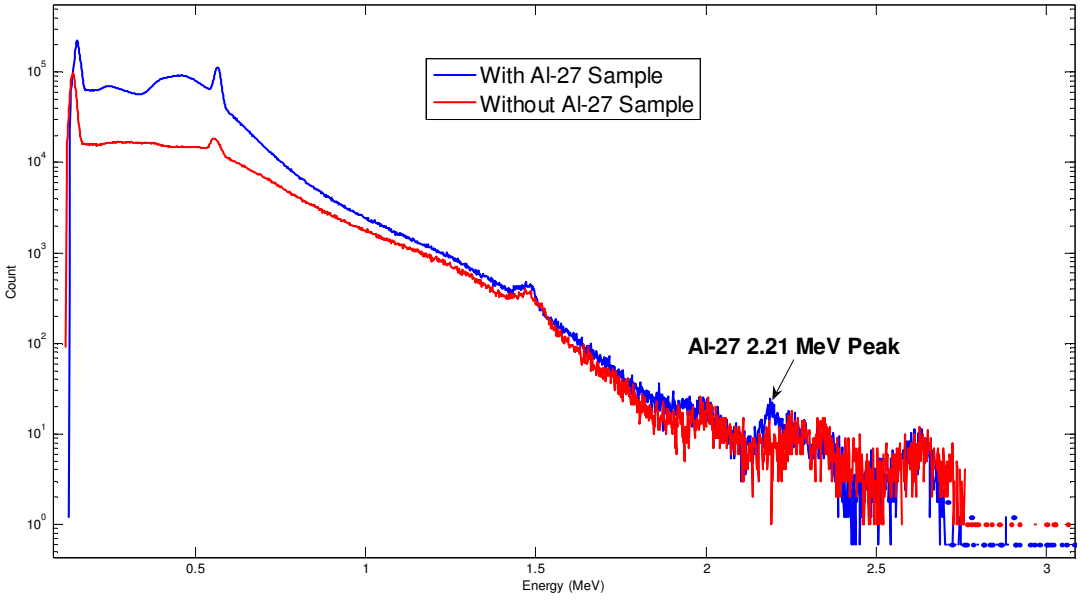

Figure 4.24 Measurement results from NRF experiments with Al sample.

The 2.21 MeV resonant NRF peak of the ^{27}Al nuclei can be distinguished from the background. The total count rate was about 10^4 cps and the dead time was 4.5% for the measurement with Al sample in the beam. The net rate under the photopeak was 0.1 ± 0.06 cps. The signal to noise was 0.62. Possible reasons for the inferior SNR are: 1) more scattering of off-resonant photons into the photopeak because of the higher electron density in the Al sample; 2) slightly worse energy resolution at the higher energy; 3)

more fluctuation in counts from impurities in the $LaCl_3$ detector [98] because the ^{27}Al resonant peak is located right on top of the high energy structure in the spectrum. Ideally, the third reason can be overcome by taking a longer measurement.

Again, the counting rate given by the analytical method and the Monte Carlo method are close, but both of them over-predicted the counting rate by a factor of ~ 10 due to problems with the focus of the electron beam.

C. NRF experiments with DU sample using the $LaCl_3$ detector

Another set of experiments was performed to investigate the excited levels in ^{238}U between 2.1 MeV and 2.5 MeV. These known levels are listed below, in Table 4.2. Data was taken from NNDC (National Nuclear Data Center) for (γ, γ') reactions.

Table 4.2 Excited levels of interest in ^{238}U

E_{level} (keV)	J	Width (eV)	Eγ (keV)	Iγ	Transition	Final Level (keV)
2468	1+	0.032	2423	50		45
			2468	100	M1	0
2410	1+	0.028	2365	54		45
			2410	100	M1	0
2295	1+	0.014	2250	59		45
			2295	100	M1	0
2245	1+	0.031	2200	47		45
			2245	100	M1	0
2209	1+	0.058	2164	55		45
			2209	100	M1	0
2176	1+	0.058	2131	52		45
			2176	100	M1	0

Here, we choose the level at 2.176 MeV as an example to illustrate how the counting rate was estimated.

The 2.176 MeV level in ^{238}U has width of 58 meV and a total angular momentum of +1. The transition between this level and the ground level (total angular momentum =

0) is an M1 transition. It can also decay to the 45 keV level with a branching ratio of 1/3. Thus, the peak NRF absorption cross section can be calculated using the Breit-Wigner formula (section 4.2.1) as:

$$\sigma_{abs}^{0} = 2\pi\lambda\!\!\!^{-2}\,\frac{2J_1+1}{(2J_0+1)}\,\frac{\Gamma_0}{\Gamma} = 2\pi\left(\frac{0.0057\,\mathring{A}}{2\pi}\right)^2 \frac{2\times1+1}{2\times0+1}\times\frac{2}{3} = 1034.2\,barn,$$

and the integral cross section is

$$\int \sigma_D(E)dE = \frac{\sigma_{\max}^{0}\Gamma\pi}{2} = \frac{1034.2\,barn\times58meV\times\pi}{2} = 94.2\ barn\cdot eV\ .$$

The Doppler width at room temperature for the ^{238}U sample can be calculated as follows:

$$\Delta = \frac{E}{c}\sqrt{\frac{2kT}{M}} = \frac{2.176\,MeV}{c}\sqrt{\frac{2\times26\,meV}{238\times1.67\times10^{-27}\,kg}} = 1.09\ eV\ .$$

Thus, the shape of the cross-section can be approximated using a top hat function with an amplitude of 43.2 barn (= 94.2 $barn\cdot eV$ /(2×1.09 eV)) and a width of 2.18 eV, shown as follows in Figure 4.25.

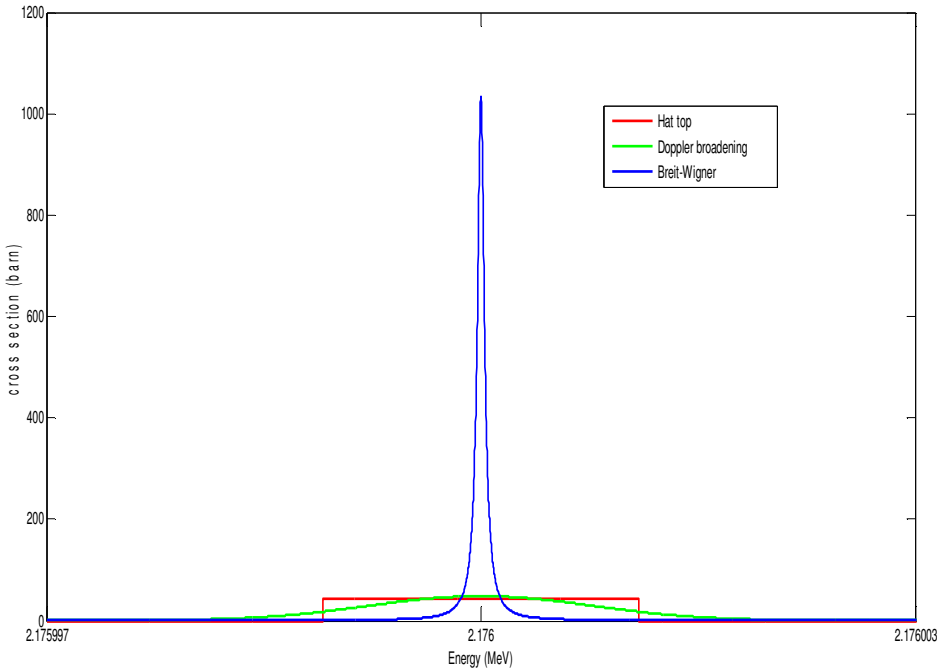

Figure 4.25 ^{238}U NRF cross section before (blue), after (green) Doppler broadening and the top hat approximation (red).

The total photon-atomic cross-section in the DU sample was estimated to be 19.4 barn at 2.176 MeV [98]. Comparison between BN, Al and DU samples is shown in Table 4.3.

Table 4.3 Comparison of photon atomic interactions vs. NRF interactions near the resonant energies in BN, Al and DU samples

	Photon atomic cross section at resonant energy (barn)	NRF cross section after Doppler broadening (top hat approximation) (barn)
BN	1.78	7.34
Al	1.95	3.94
DU	19.4	43.2

The scatterer used in this experiment was a 10 cm long DU rod with a diameter of 1 cm. The density of the DU sample is 19.1 g/cm^3. Assume it is UO_2 with 100% ^{238}U. Thus, the number of ^{238}U nuclei contained in this sample is 3.3×10^{23}.

The attenuation coefficient for NRF interaction can be calculated as

$$\tau_{res} = \rho\sigma = 1.82\,cm^{-1},$$

where ρ is the particle density for ^{238}U nuclei as well as UO_2 atoms.

The attenuation coefficient for the photo-atomic interaction can be calculated as

$$\tau_{atom} = \rho\sigma = 19\,g/cm^3/(238+32)/(1.67\times10^{-24}\,g)\times19.4\,barn = 0.82\,cm^{-1}.$$

If the DU rod sample is oriented perpendicular to the beam, the probability for a resonant photon to escape without an NRF or photo-atomic interaction with ^{238}U nuclei is

$$p_e = \exp(-(\tau_{res}+\tau_{atom})d) = 0.07.$$

The flux of resonant photons at the sample surface is

$$\begin{aligned}\dot{R} &= \phi\cdot 2\Delta S(1-p_e)\frac{\tau_{res}}{\tau_{atom}+\tau_{res}}\\ &= 3.2\times10^2/(eV\cdot cm^2\cdot s)\times2.18\,eV\times5.08\,cm^2\times(1-0.07)\times\frac{1.82}{1.82+0.82}\\ &= 2.25\times10^3/s\end{aligned}$$

Following the same route as for the Al sample, the predicted counting rate under the resonant peak is

$$\dot{r} = \dot{R}\frac{\Omega}{4\pi}\varepsilon_{ip}\exp(-\pi t) = 0.06\,cps.$$

The same MCNP5 simulation as performed earlier for BN and Al samples predicted a counting rate of 0.1 cps. In a similar 40-minute measurement, no resonant peaks were observed from the DU sample.

If the relationship between predicted and measured results observed in previous sections stands true here, the measured counting rate would be less than 0.01 cps. In a 40-minute measurement with the $LaCl_3$ detector used here, this equals 24 counts spread over 50 channels. This could easily be buried in the statistical variance in these channels. Thus, to increase the SNR, a detector with better energy resolution was needed.

4.6.3.2 Scattering Experiments Using a $LaCl_3$ detector and FPGA Based DAQ System

Similar experiments as described above were performed using the FPGA based DAQ system described in Chapter 3. In this digital DAQ system, the input signal was digitized and processed in real time. This can greatly decrease the processing time and increased the throughput rate of the spectroscopic system. Theoretically, this can either give better energy resolution (thus better SNR) than the analog system at the same input rate; or enable the spectroscopic system to operate at a higher input rate while maintaining the same energy resolution.

In this experiment, by carefully adjusting the detector to sample distance and the beam current, we were able to achieve roughly the same net count rate under resonant peaks, while getting slightly better SNR than the results from the analog system. The following spectra were taken with a beam current of 30 μA. The detector to sample distance was measured to be roughly 5 inches.

The result from the same BN sample used before is shown below in Figure 4.26.

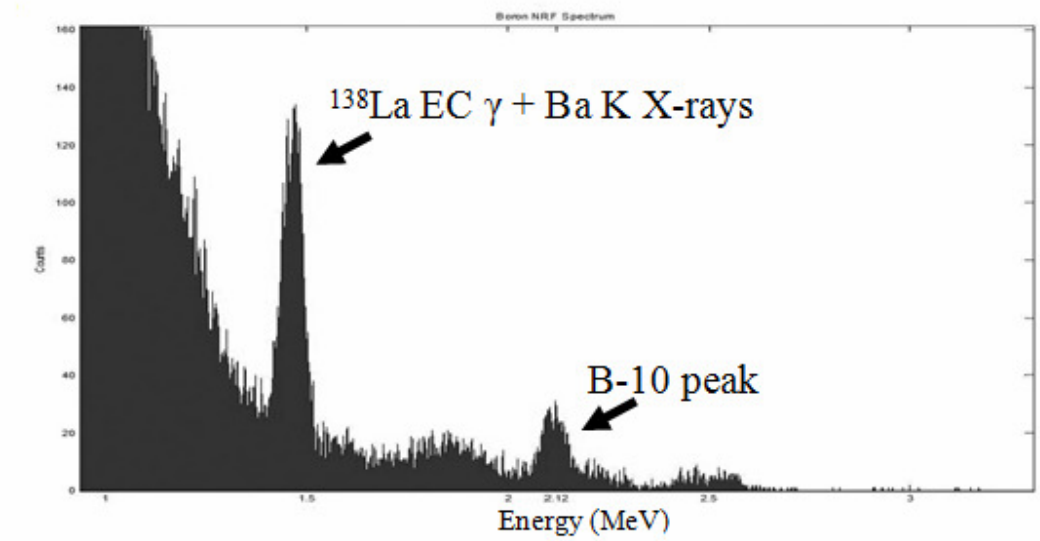

Figure 4.26 NRF measurement result with BN sample

The net count rate under the Boron resonance peak was 0.2 cps. The signal to noise ratio was calculated to be 3. The result with the Al sample and the Si sample is shown in Figure 4.27.

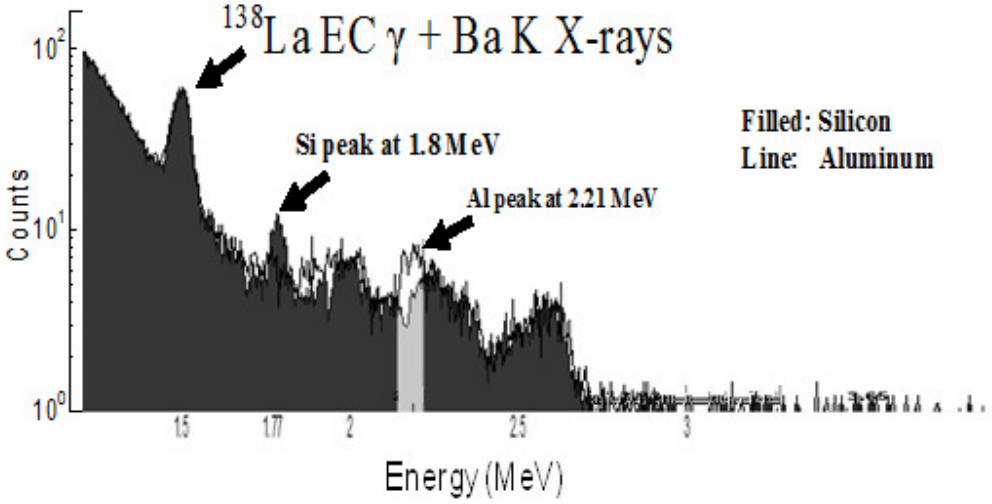

Figure 4.27 NRF measurement results with Si sample and Al sample

The SNR was calculated to be 3.2 for Si peak at 1.8 MeV and 0.68 for Al peak at 2.21 MeV. However, we were still not able to observe the NRF peak from our DU sample with this improved SNR. The measurement result with the thinned DU sample is shown in Figure 4.28.

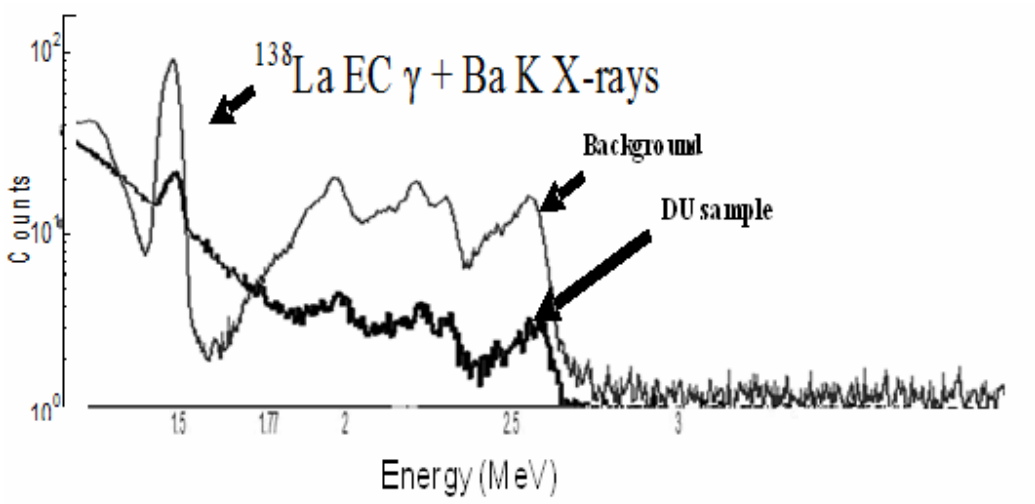

Figure 4.28 NRF measurement results with DU sample

4.6.3.3 Scattering Experiments using an HPGe detector

Similar experiments were also performed using an HPGe detector. The HPGe detector used in these experiments has some advantages over the $LaCl_3$ detector used in the previous experiments:

1) It has a much bigger volume (3×3 inch vs. 1.5×1.5 inch). This leads to a higher detection efficiency and higher peak-to-total ratio in the spectra measured. The intrinsic peak efficiency at 2 MeV is 16% [100], which is 3.2 times the value for the $LaCl_3$ detector used in previous experiments.

2) The energy resolution is 10 times better than the $LaCl_3$ detector (3 keV vs. 31.2 keV at 1.33 MeV). Better energy resolution gives better signal-to-noise ratio, as discussed in previous sections.

The setup of these experiments is similar to what was shown in Figure 4.19. However, the distance between the scatterer and the detector was increased to 10 inches. The HPGe detector (ORTEC GEM90) has an integrated preamp with a shaping time measured to be 40 μs. The first spectroscopic system used with the detector was the same as that used with the $LaCl_3$ detector. With a beam current at 120 μA, the system couldn't function because of severe pile-up. We were also forced to lower the beam current to accommodate the long shaping time and processing time following each detected event in the spectroscopic system used with the HPGe detector. The spectrum shown below in Figure 4.29 was measured with a beam current of 30 μA for 13 minutes, using the same BN sample as in the previous section.

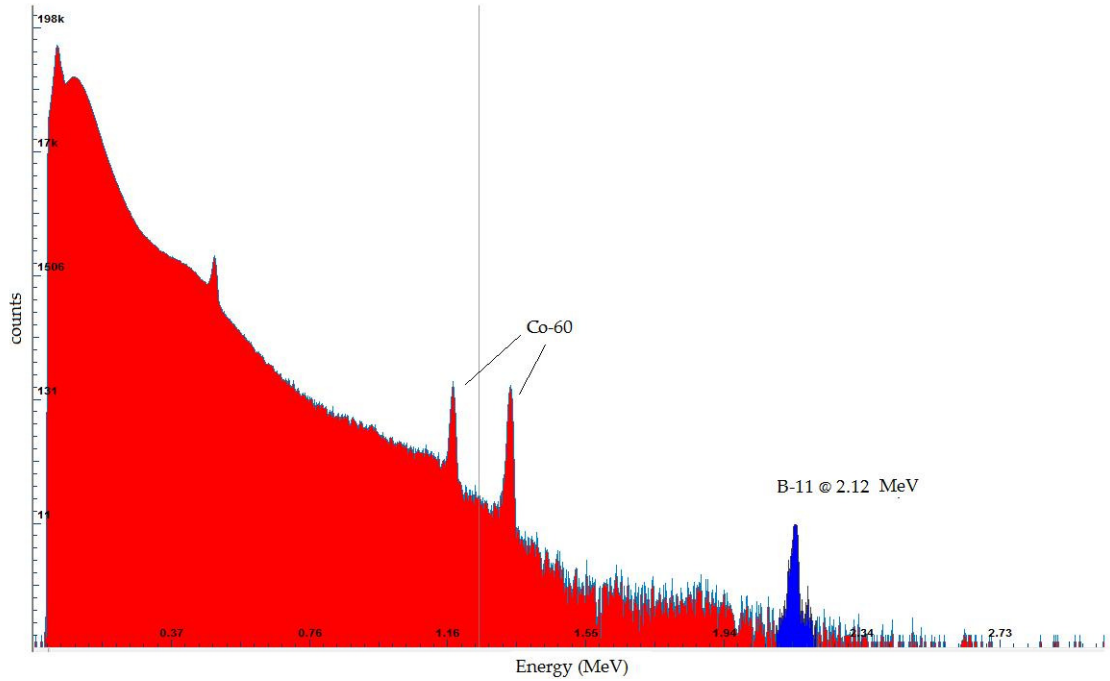

Figure 4.29 Spectrum from the BN sample measured with the HPGe detector.

The count rate was 2.2×10^4 cps and the dead time was 11%. The resolution at 1.33 MeV was measured to be 15 keV, which is far worse than the best resolution we have observed (3 keV). This degradation was caused by the slow processing time of the analog system. At such a high count rate, there wasn't enough time for the signal to fully return to the baseline before the next pulse came in.

Even with a much lower beam current, the count rate under the photo-peak was still measured to be higher than what was observed in previous experiments using the $LaCl_3$ detector (0.48 cps vs. 0.19 cps). This was attributed to a higher detection efficiency and peak-to-total ratio. The SNR improved to 4.65, compared with 2.27 using the $LaCl_3$ detector.

A 5-minute spectrum was measured with the Al sample. The result is shown below in Figure 4.30.

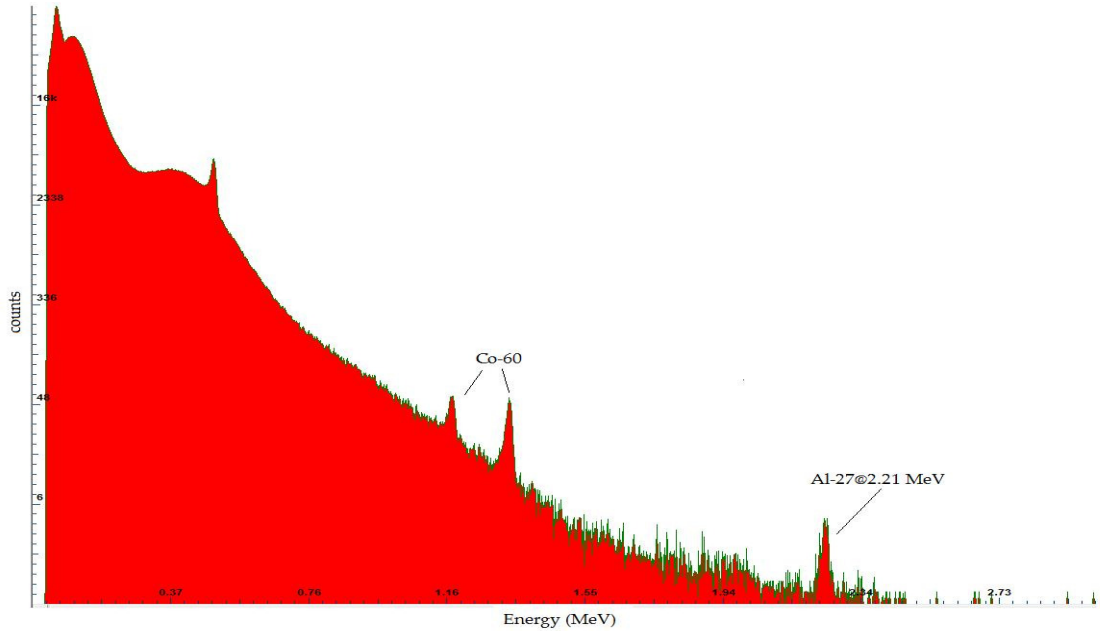

Figure 4.30 Spectrum of the Al sample measured with the HPGe detector.

Although the spectrum was measured under the same conditions (geometry and beam current were kept the same) as the BN, the count rate was higher (5.8×10^4 cps) and the dead time was longer (24%), because the Al sample has a greater electron density, thus more scattering. The resolution at 1.33 MeV was measured to be 20 keV. The count rate under the photo-peak was 0.32 cps and the SNR was measured to be 2.09.

As can be observed, utilizing the HPGe detector greatly improved the performance of the detection system. Both detection efficiency and SNR were significantly improved. However, we still failed to observe NRF peaks from ^{238}U using this much-improved system, even with a bigger sample (3 inch by 3 inch by 1 inch DU block). The primary reasons for this are that the DU sample is so dense that background in the high energy range is significant (caused by multiple scatterings in the sample), bremsstrahlung x-rays produced by high energy electrons knocked off DU atoms by high

energy incident photons, and coherent scattering. If these kinds of background can be somehow decreased, this will improve SNR.

Compared to the shape of the NRF cross section, the background spectrum varies much more slowly as a function of energy. Thus, by improving the energy resolution, we can improve the SNR. One source of background at higher energies is the pile-up of low-energy pulses, which are so close to each other that the spectroscopic system cannot resolve them, taking them as a single pulse with much higher amplitude. The background caused by pile-up can be significantly decreased by utilizing the pileup rejection (PUR) function included in the shaping amplifier. The PUR output from the shaping amplifier prevents the MCB from processing pulses when pile-up occurs. So to reduce the effects of pileup, we lowered the beam current and employed pileup rejection to see if this was significant.

The following spectrum shown in Figure 4.31 for the BN sample was measured with a beam current of 20 μA, with the PUR function enabled. The measurement time was 10 minutes and the counting rate was only 854 cps. The energy resolution at 1.33 MeV was 3 keV. The net count rate under the photo-peak was measured to be 0.13 cps.

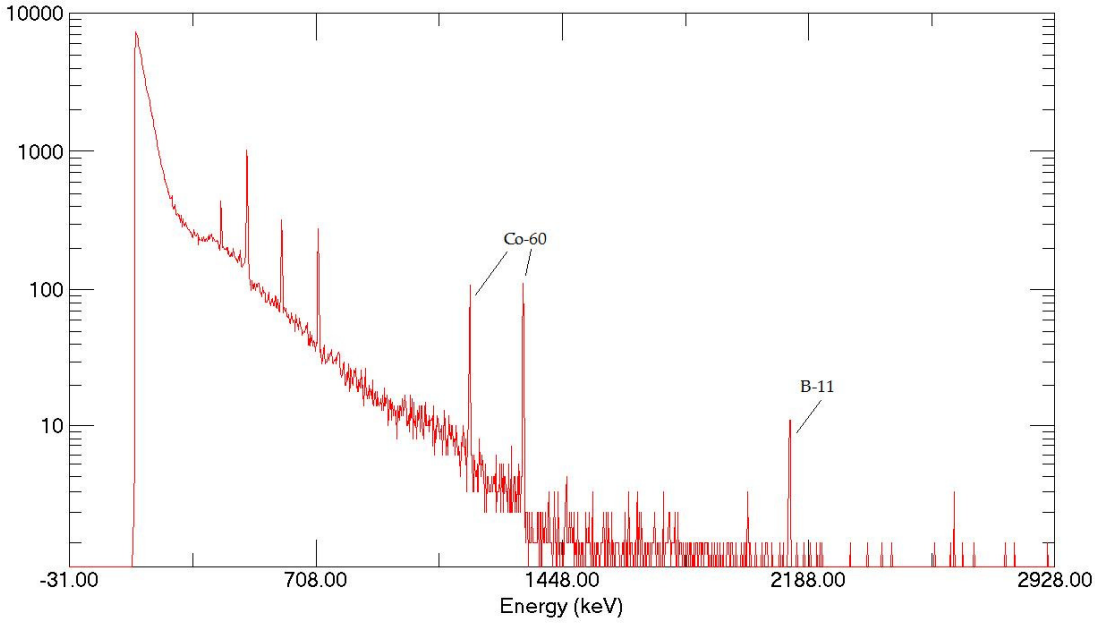

Figure 4.31 Spectrum from the BN sample measured by the HPGe detector at 20 μA with the PUR enabled.

This measurement showed that the spectroscopic system can give excellent performance at low count rates with the PUR enabled. Under the same conditions, a measurement was performed with a thinner DU sample (3 inch by 3 inch by 0.1 inch slab) and PUR enabled. The result is shown below in Figure 4.32. The count rate was 2.3×10^3 and the resolution at 1.33 MeV was measured to be 3 keV. The measurement time was 5.8 hours. Figure 4.33 shows the details of the region of interest (2.1 – 2.5 MeV).

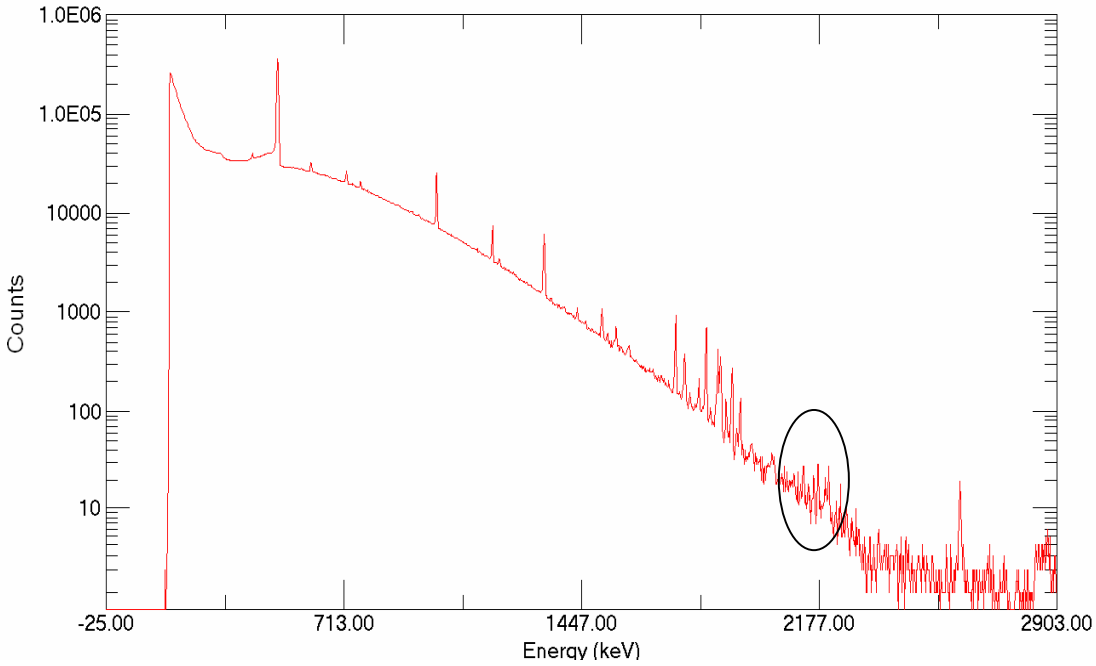

Figure 4.32 Spectrum from the DU sample measured by the HPGe detector (region of interest is marked)

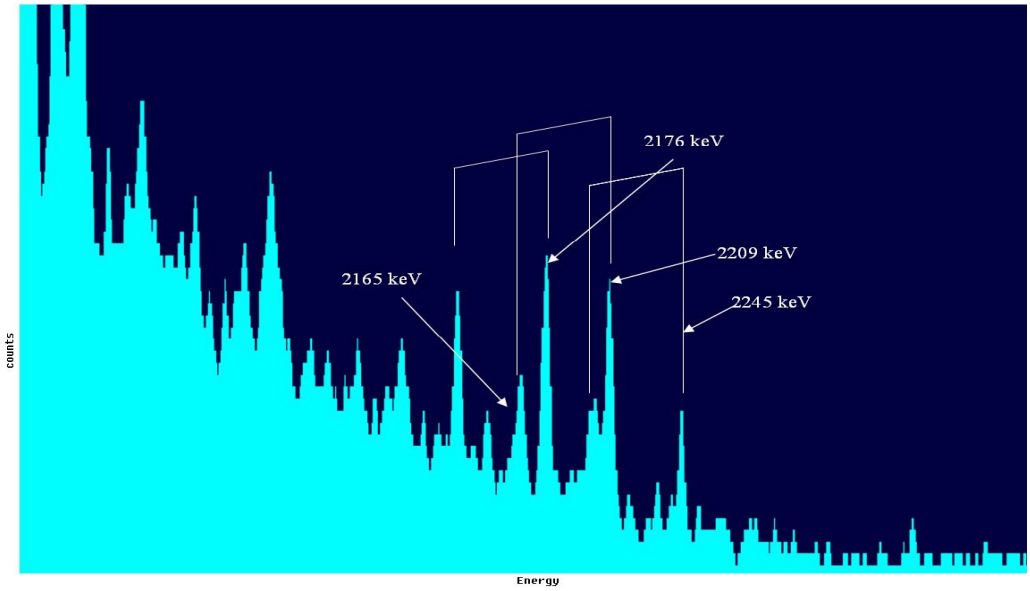

Figure 4.33 Details of the ROI in the DU spectrum [see Table 4.2]

The NRF peaks from transitions of the ^{238}U nuclei can be clearly observed in the spectrum with good SNR (for the strong resonance at 2176 keV, the SNR was 49.6±7%). However, the count rate for the resonant photons was only 0.01 cps at 2176 keV. For each transition, there is a pair of peaks separated by 45 keV, representing the possibility for each excited level to decay to either the ground level or the 45 keV excited level, as shown in Table 4.2.

4.7 Conclusions and Discussion

In this chapter, NRF experiments performed at the Radiation Laboratory of the University of Notre Dame using a 3 MeV Van de Graaff electron accelerator were described.

The samples used in these experiments include a 2 × 2 × 3 inch BN solid, a 3 × 3 inch Al cylinder, a 10 cm long DU rod with a diameter of 1 cm, and a 3 × 3 × 0.1 inch DU slab. Initially, a 3 × 3 × 1 inch DU bulk was ordered for the NRF experiment. Later, it was realized that majority of the incident photons at resonant energies were scattered by the nuclei within a few millimeter of the incident surface, because of the high density of DU. The rest of the sample made no contribution to the NRF photon measurements. Photon-atomic scattering of incident photons in this part of the sample produced background and increased pileup in the spectroscopy system. Thus, it was necessary to make the sample much thinner than what we ordered. The depth of the sample was reduced to roughly 0.1 inch in the successful measurements shown in Figures 4.32 and 4.33.

A newly-developed lanthanum halide scintillation detector was used in the NRF experiments. Because of the cost issue, the size of the detector was limited to 1.5 ×1.5

inch. This greatly reduced the detection efficiency and the peak-to-total ratio. The low detection efficiency leading to long detection times and a low peak-to-total ratio affected the SNR of the resonance spectra. The low SNR again led to long detection times if a certain error rate was to be achieved. All of these can be improved by increasing the size of the detector.

Another limiting factor for the scintillation detector used in these experiments is the energy resolution. The best energy resolution observed from our detector was 3% at 1.33 MeV (40 keV), but worsens at higher counting rates. In NRF technique, the SNR is closely related to energy resolution. Unfortunately, the width of the emission line of the NRF interaction is much narrower than the smallest energy difference that can be resolved by commercially available radiation detectors. As the energy resolution degrades, more background is registered under the photopeak, and the worse the SNR is. The measurement results showed that the energy resolution of the lanthanum halide detectors was good enough for detection of strong resonances in light nuclei, for example, B, Al and Si. However, in the case of detection with dense materials (for example, SNM), the much higher background at high energies limited us to detectors with better energy resolution, namely HPGe detectors. The FPGA based DAQ system described in Chapter 3 was used together with the $LaCl_3$ detector in NRF experiments. Although we were able to achieve better SNR while maintaining roughly the same net count rate under the resonant peak, we failed to observe NRF from DU using this setup as well.

HPGe detectors provide the best energy resolution among all commonly available radiation detectors. The detector used in our experiments has an energy resolution of 3 keV at 1.33 MeV, 13 times better than what the $LaCl_3$ detector offers. The greater energy

resolution brought a much higher SNR, as shown by the measurements. Also, the PUR feature built into the spectroscopy system further reduced the background at high energy. The resonance from the DU sample was successfully observed in the measurements with a good SNR (49.6% for the resonance at 2176 keV). However, the counting rate of the resonance photons was low (0.01 cps at 2176 keV). The beam current was limited to 20 μA, otherwise the energy resolution would start to degrade due to pileup. Because the HPGe detector was on loan from Argonne National Laboratory, we were not at liberty to modify the integral pre-amp nor made use of our pulse processing electronics discussed in Chapter 3. Using multiple detectors could compensate for the loss of counts caused by the low beam current while keeping a good SNR.

Experimental results are summarized in Table 4.4.

Table 4.4 Summary Table of Observed NRF Lines

Sample	Isotope	Size	$LaCl_3$ + Analog DAQ		$LaCl_3$ + FPGA DAQ		HPGe	
			Observed?	SNR	Observed?	SNR	Observed?	SNR
BN	B-11	2" x 2" x 3"	Yes	2.27	Yes	3	Yes	4.65
Al	Al-27	3" x 3" Cylinder	Yes	0.62	Yes	0.68	Yes	2.09
Si	Si-28	3" x 3" Cylinder	N/A	N/A	Yes	3.2	N/A	N/A
DU	U-238	10 cm x 1 cm rod	No	N/A	N/A	N/A	N/A	N/A
		3" x 3" x 1"	N/A	N/A	N/A	N/A	No	N/A
		3" x 3" x 0.1"	No	N/A	No	N/A	Yes (PUR enabled)	0.496

The bremsstrahlung x-ray source used in this work is the most common source of producing the resonance photons. A very high photon flux can be generated using this type of source, but because of the broad energy spectrum of the bremsstrahlung source, their efficiency in NRF experiments is very low. The typical energy spread of photons from a bremsstrahlung source is on the order of 1 MeV, while the width of the absorption

line in the NRF interaction is only several eV after Doppler broadening. This can be seen in the measured spectra where only a negligibly small percentage of the detected photons contain information of interest. Furthermore, high energy off-resonant photons generate background in the NRF measurements by down-scattering and also producing problematic secondary electrons in the sample. Low energy off-resonant photons contribute to the pile-up that degrades the energy resolution of the detector. Obviously, bremsstrahlung x-ray sources are not ideal for NRF technique. The development of sources with tunable energy and narrow energy span would make the NRF technique a more feasible tool for security applications.

CHAPTER 5

Summary and Conclusions

To identify U-235 for homeland security applications, it is likely that active interrogation techniques will be needed. Because of the likely reticence to use fast neutrons, this leaves x-rays as the only current practical option. As a result, this work looked at two detection methods. The first method is the detection of SNM based on delayed gamma rays emitted by fission products after photon induced fission reaction. After irradiation by a 9 MeV interrogating X-ray beam, fission products were observed from depleted Uranium. used throughout this work as our target material. After waiting for several minutes we saw gamma rays emitted by fission products with medium to long half lives [cf. Table 2.5]. The time decay of the delayed gamma ray emission was also studied, by integrating the delayed gamma ray spectrum every 3 seconds starting at 37 seconds after a 24 seconds irradiation [cf. Fig. 2.8]. Using the time information, additional fission products were identified [cf. Table 2.7]. In the absence of spectroscopy, just using high energy (> 3 MeV) delayed gamma ray count rate as a function of time was also established [cf. Fig. 2.9 and Fig. 2.10] as a means to identify sensitive materials. This result agreed with data reported by other researchers [31]. In order to measure delayed gamma ray spectrum shortly after the irradiation, we then modified the DAQ electronics to synchronize with the LINAC pulses. We also moved the detector into the irradiation hall and shielded/collimated it to ensure normal operation when the beam was

turned on. The measurement started at 6 ms after each LINAC pulse until the next pulse arrived. At shorter times after the irradiation, we saw short lived fission products like Cs-138 and Sr-94 [cf. Fig. 2.15 and Fig. 2.16]. The key result from our work was to show that while fission products are easily observable up to several minutes after the interrogation, an advantage of measuring sooner after the irradiation is greater sensitivity and the ability to observe the more intense and shorter-lived fission products.

In Chapter 3, two digital spectroscopy systems developed to handle high count rate events in active interrogation were discussed. The first system is based on a National Instruments DAQ card [cf. Table 3.1 and Fig. 3.2]. It has high sampling rate and excellent resolution. They system is synchronized with the accelerator pulses. Waveform of the input signal is acquired and processed using a deconvolution method [cf. Fig. 3.5]. Together with a fast scintillator detector, spectra were measured without experiencing significant dead time and degradation in energy resolution at a high event rate (~10^6 cps) [cf. Fig. 3.7]. The system was implemented together with a fast lanthanum halide detector in a series of photofission experiments to measured delayed gamma rays emitted by fission products. We weren't able to see individual gamma lines using this electronics together with the $LaCl_3$ detector because the energy resolution of the $LaCl_3$ detector was not sufficient. But we were able to see a more than 60% count rate difference with would be enough to identify photofission was occurring [cf. Fig. 3.9].

Another system was developed based on a fast ADC chip and an FPGA chip [cf. Fig. 3.10]. The 14-bit ADC worked at a sampling rate of 125 MSPS. The input signal is digitized and processed in real-time on the FPGA chip, using either trapezoidal shaping method [cf. Fig. 3.14] or MWD shaping method [cf. Fig. 3.19]. The spectrum was created

and stored on the FPGA board. This eliminated the system dead time caused by the slow communication between the DAQ system and PC. The performance of the system was tested up to a count rate of 10^6 cps using a fast $LaCl_3$ detector. We observed good energy resolution at low count rate and good throughput rate at high count rate with little degradation in energy resolution [cf. Fig. 3.23 and Fig. 3.24].

The second detection method was based on nuclear resonance fluorescence technique. Resonance photons carry unique information of energy levels inside nuclei and can be used as signature signals for isotope identification. Scattering experiments were set up at the Radiation Laboratory of the University of Notre Dame. We used a 3 MeV Van de Graaff accelerator as our photon source [cf. Fig. 4.12]. Using an HPGe detector, we were able to measure NRF peaks from various isotopes. For light materials, like B, Si and Al, the peaks are easily observable and the SNR was greatly improved when we implemented the PUR technique [cf. Fig 4.29 – Fig. 4.31]. NRF peaks from ^{238}U samples were successfully observed using the 90% efficient HPGe detector but required PUR, long acquisition times, and a thinned sample. The net count rate under the 2176 keV peak was measured to be 0.01 cps and the SNR was 49.6 ± 7% [cf. Fig. 4.32 and Fig. 4.33].

We also tried to measure NRF using a $LaCl_3$ detector with the FPGA based DAQ system described in Chapter 3. NRF peaks were observed from light materials like BN, Si and Al. However, we weren't able to observe NRF from DU using the $LaCl_3$ detector. Because of its energy resolution, the $LaCl_3$ detector could not provide a sufficient SNR to separate the DU resonance peaks from the background.

The results from this work show both methods could be effective in identifying sensitive material. Photofission may be a more realistic option in the short-term since the plan is to scan all cargo using 6-9 MeV transmission x-ray radiography. By adding spectroscopic detectors to these systems, photofission may be an observable that would lead to a more careful inspection of the cargo. We did not look at common materials in cargo that may confound this approach (e.g., uranium and thorium are common materials) nor examine whether there exists sufficient sensitivity to differentiate materials from their fission product distributions.

Nuclear resonance fluorescence seems like an ideal method to identify U-235. However, while we were able to (finally) observe U-238 NRF emissions, it was not easy even under ideal measurement conditions. The narrow resonance lines superimposed on a large background made this detection problem quite challenging even using highly-shielded HPGe detectors. Monoenergetic and continuous beam x-ray sources, coupled with high-Z, high volume detectors having eV resolution at MeV energies, might make this option more practical.

APPENDICES

Appendix 1. Hardware Specifications of the Xilinx Virtex-4 FPGA Development Board and the AVNET P240 Analog Module

The digital spectroscopic system developed is shown in Figure A1.1. The ADC module is a P240 Analog Module developed by AVNET. Through the P240 bus, this module is mounted on an FPGA evaluation board, the Xilinx Virtex-4 LX/SX MB Development Board, equipped with a single Xilinx Virtex-4 LX60 FPGA. The input signal is digitized by the ADC module and then transferred to the FPGA development board. A single FPGA chip is responsible for both data buffering and processing. Signal processing, spectroscopic measurement, data storage, and data transfer are handled by this FPGA simultaneously.

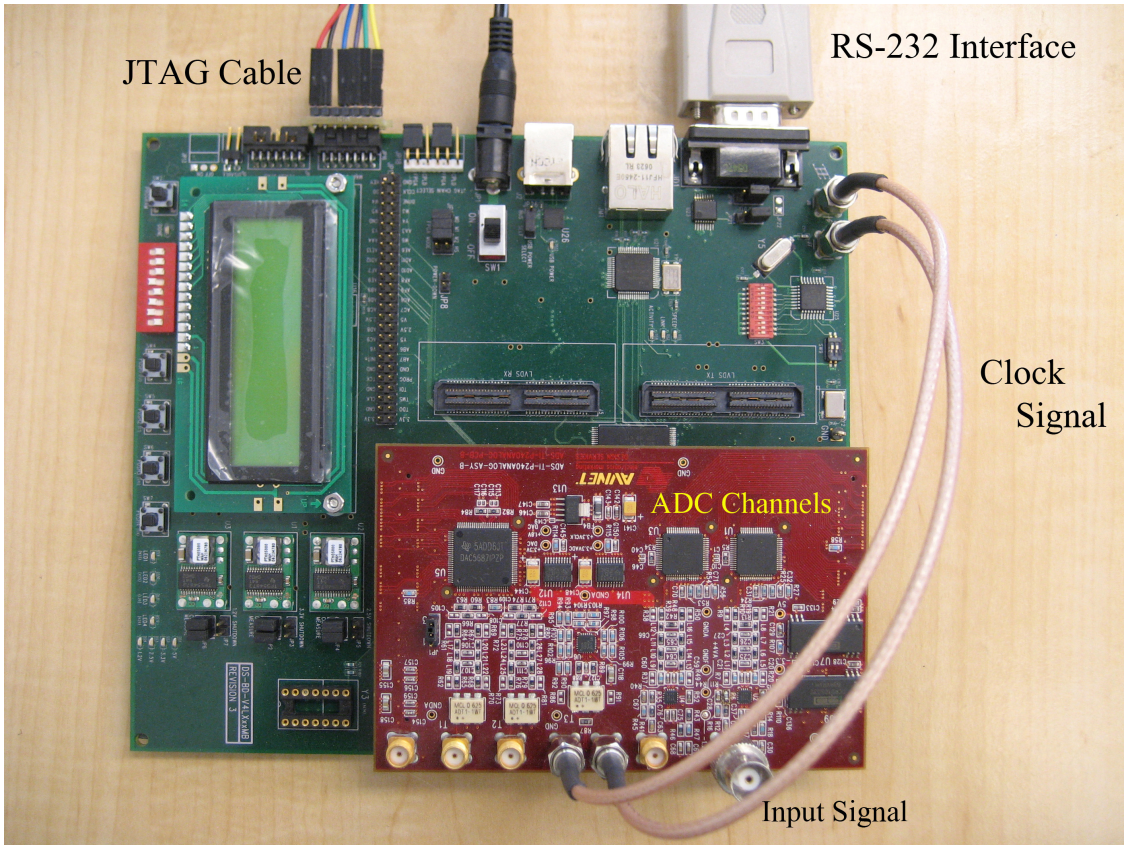

Figure A1.1 Digital Spectroscopic Measurement Based on Fast ADC (Red Board on the Top) and FPGA (Green Board at the Bottom)

A1.1 The ADC Module

In this system, an AVNET P240 Analog Module was used as the ADC module, shown in Figure A1.2 [101]. It provides an analog interface to the Virtex-4 development boards residing on the Virtex-4 FPGA. This module supplies dual-channel analog input and output. It is suitable for FPGA-based DSP applications in audio, video, and general mixed-signal applications.

The ADC module has four independent analog channels, two input channels and two output channels. The two analog input channels are identical in design. Each of them is equipped with a Texas Instruments ADS5500 14-bit, 125 MSPS A/D converter. The ADS5500 chip converts the input signal into 14-bit data for the FPGA processor implemented on the base Virtex-4 development board. The analog output channels feature a Texas Instruments 16-bit, 500 MSPS, 2X-16X interpolating dual-channel DAC converter. The DAC5687 features optional signal processing blocks, including digital interpolation filters, all programmable via an SPI port. The outputs are 50-ohm transformer coupled, equipped with analog reconstruction filter stages.

This analog module fully supports the Xilinx System Generator for DSP and the MathWork's Simulink to simplify application development. Key features are shown in Table A1.1. Figure A1.3 shows a block diagram of the P240 Analog Module.

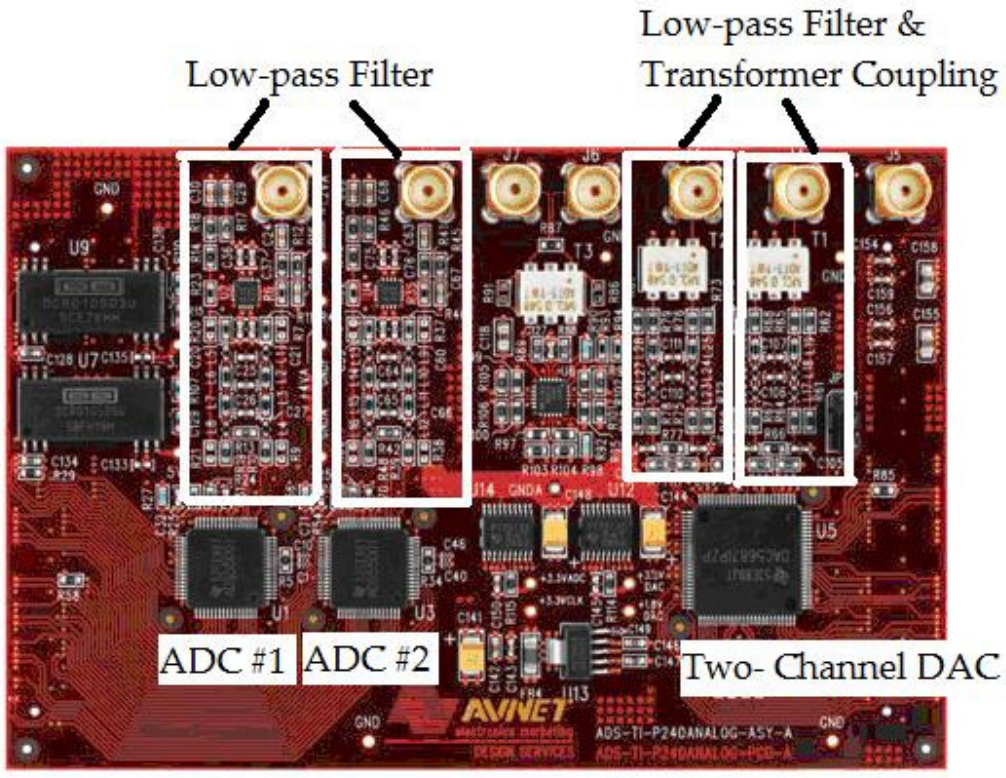

Figure A1.2 AVNET P240 Analog Module

Table A1.1 Key Features of the AVNET P240 Analog Module

Analog Input	Dual 14-bit, 125 MSPS ADC
	Single-ended 50 ohm inputs
	Low-pass 7^{th} order RLC anti-alias filter
Analog Output	16-bit, 500 MSPS, 2X-16X interpolating dual-channel DAC
	Internal and external reference
	Transformer coupled 50 ohm outputs
	Low-pass 5^{th} order RLC reconstruction filter
Clocking	External LVDS clock input
	Transformer coupled clock input

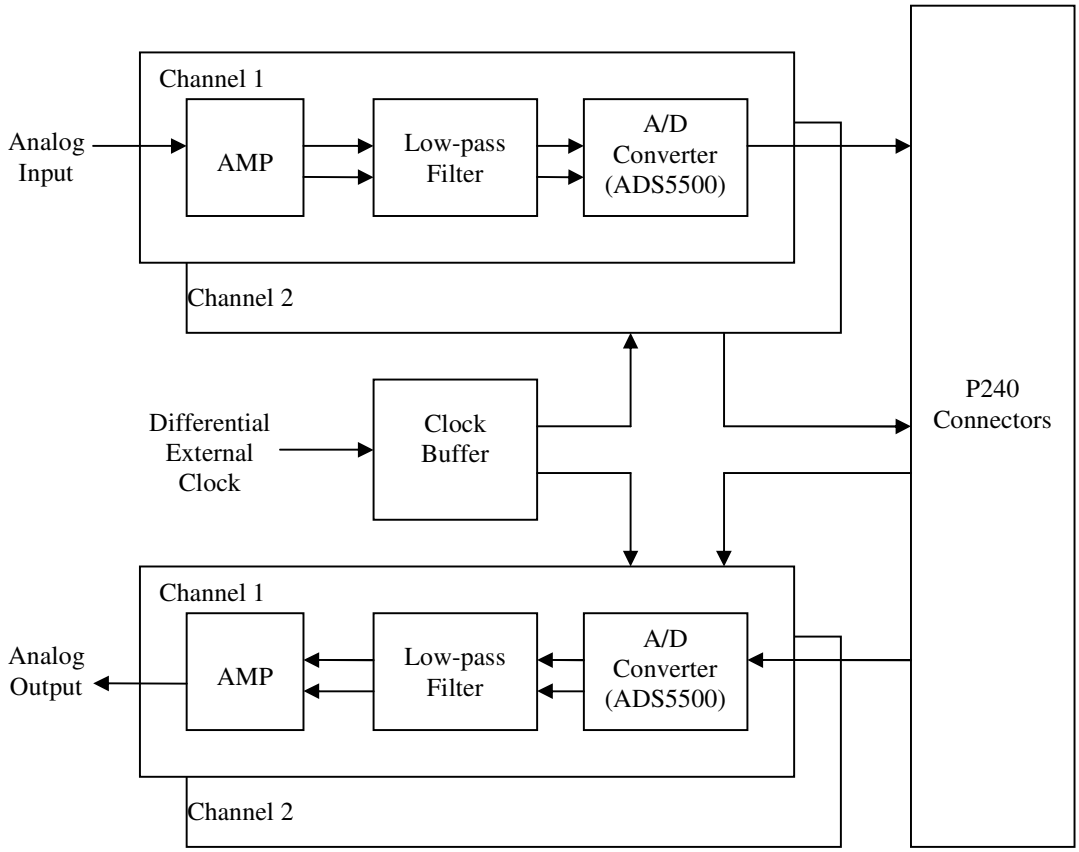

Figure A1.3 AVNET P240 Analog Module Block Diagram

In the digital spectroscopic measurement system described in this chapter, only the analog input section of this module was used. The details of the analog input section are shown in Figure A1.4.

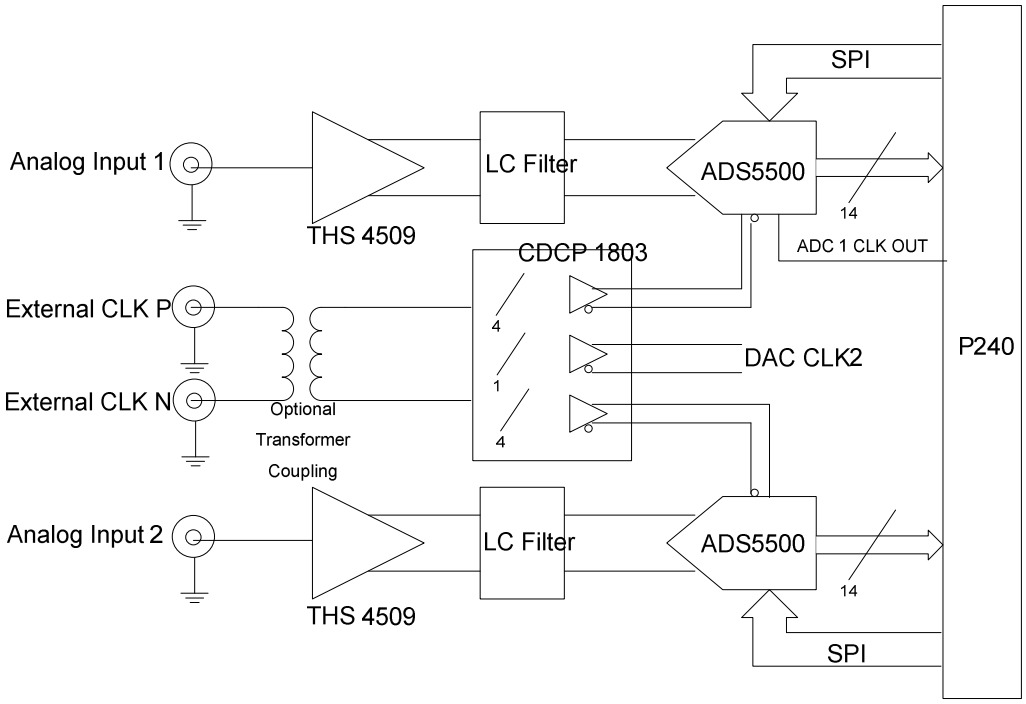

Figure A1.4 P240 Analog Module Input Section

Each analog input channel accepts a single-ended source with a 50-ohm output impedance. The incoming signal is AC coupled with the input end through a 0.22 μF capacitor. The THS 4509 wideband differential amplifier converts the single-ended input signal into a differential signal and provides a gain of 10 dB. This default gain can be changed by adjusting the values of the feedback resistors. This input stage is shown below in Figure A1.5.

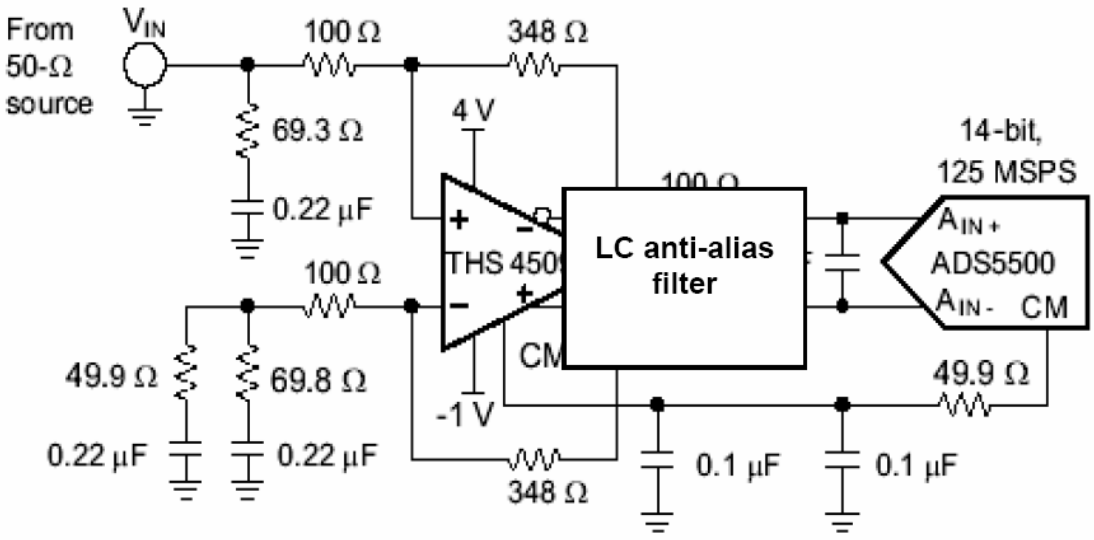

Figure A1.5 The Input Stage of the P240 Analog Module

Following the input stage is the 7th order RLC anti-alias filter. The -3 dB cut-off frequency of this circuit is 45 Mhz and it provides 60 dB attenuation at 100 MHz. These default values can be changed by modifying the values of the components. The DC attenuation through this low-pass filter is 6 dB. Hence, the total gain from the analog input end to the ADC input is 4 dB: 10 dB gain by the input stage and 6 dB attenuation by the low-pass filter.

Figure A1.6 shows the PSpice[103] simulation result of the system response to the pre-amp output signal from an HPGe detector. The polarity of the incoming signal is inverted and some overshoot is produced.

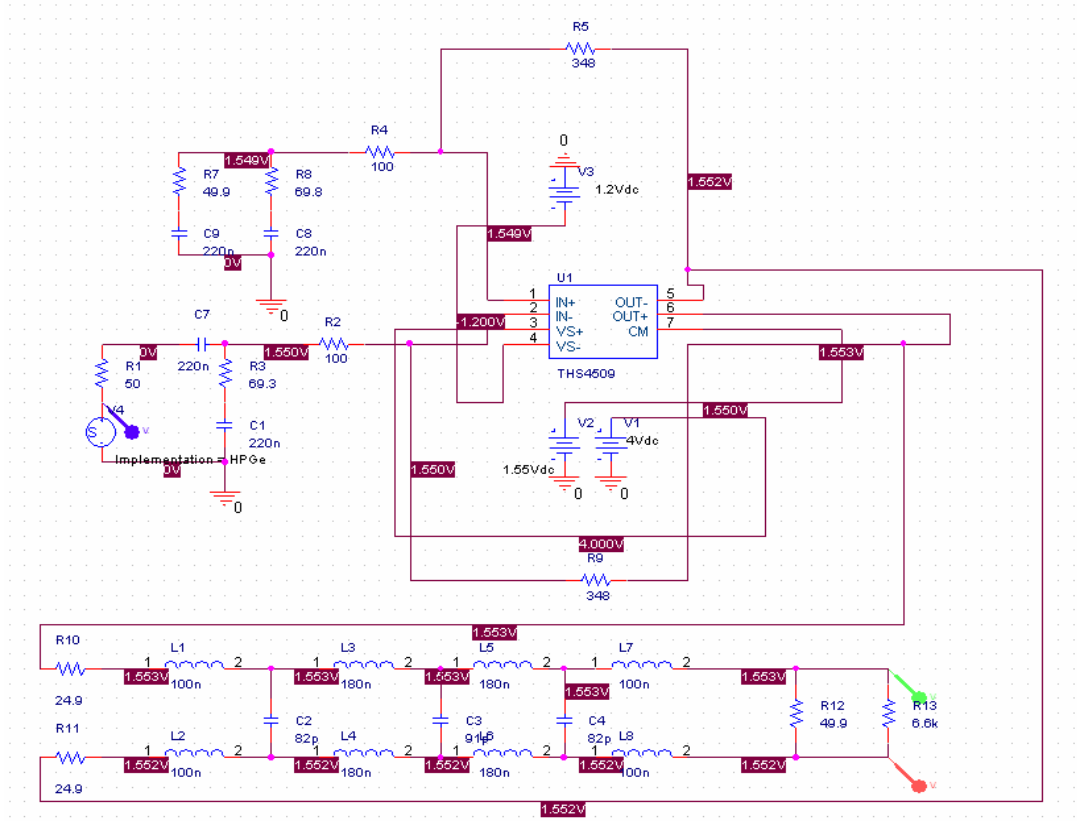

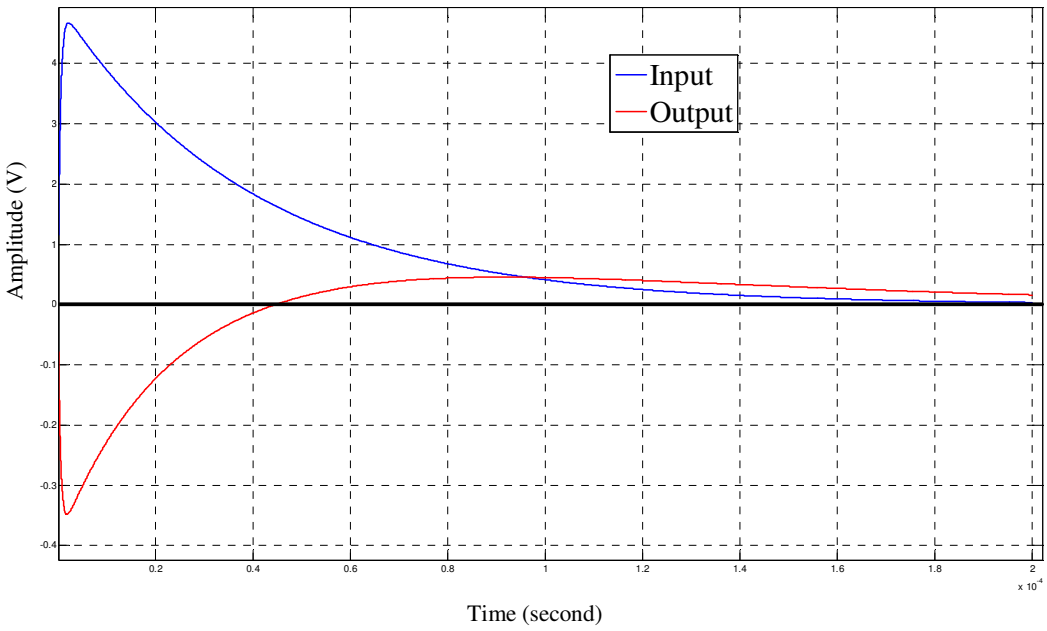

Figure A1.6 PSpice Simulation of the System Response

The analog to digital conversion in each analog input channel is done by a TI ADS5500 14-bit, 125 MSPS A/D converter. The ADC output format D13 (MSB) …… D0 (LSB) is two's complement data. The conversion result is valid on the rising edge of the clock pulse. The ADS5500 outputs its own clock to the FPGA through the P240 interface. This output clock is synchronized to the output data and has the same frequency as the input clock.

The P240 analog module features a CDCP 1803 clock buffer. It supplies a 4X divided clock signal to each of the two ADS5500 ADC's. In this design, the input to the CDCP 1803 clock buffer comes from the ICS8442 programmable LVDS Clock Synthesizer on the Virtex-4 base board via two coaxial cables, as shown before in Figure A1.1. The settings on the ICS8442 Synthesizer will be described in the next section.

A1.2 The Virtex-4 Development Board

The Virtex-4 development board provides a development platform for the Xilinx Virtex-4 FPGA's [102]. The board used in this design is equipped with a Xilinx Virtex-4 LX60 in the -10FF668 package, shown in Figure A1.7. In addition to the FPGA chip, this board also offers a group of prototyping peripherals and functions, including 10/100 MB Ethernet PHY, USB-to-UART bridge, RS232 interface, DDR memory, flash memory, user switches, LEDs, programmable clock synthesizer, LCD, and a high speed P240 expansion slot for addition of application modules and custom circuits. Configuration of the FPGA chip can be done through either the JTAG interfaces or the custom serial data

flash storage memory mounted on the System ACE interface. Key features of this development board are shown below in Table A1.2. The block diagram is shown in Figure A1.8.

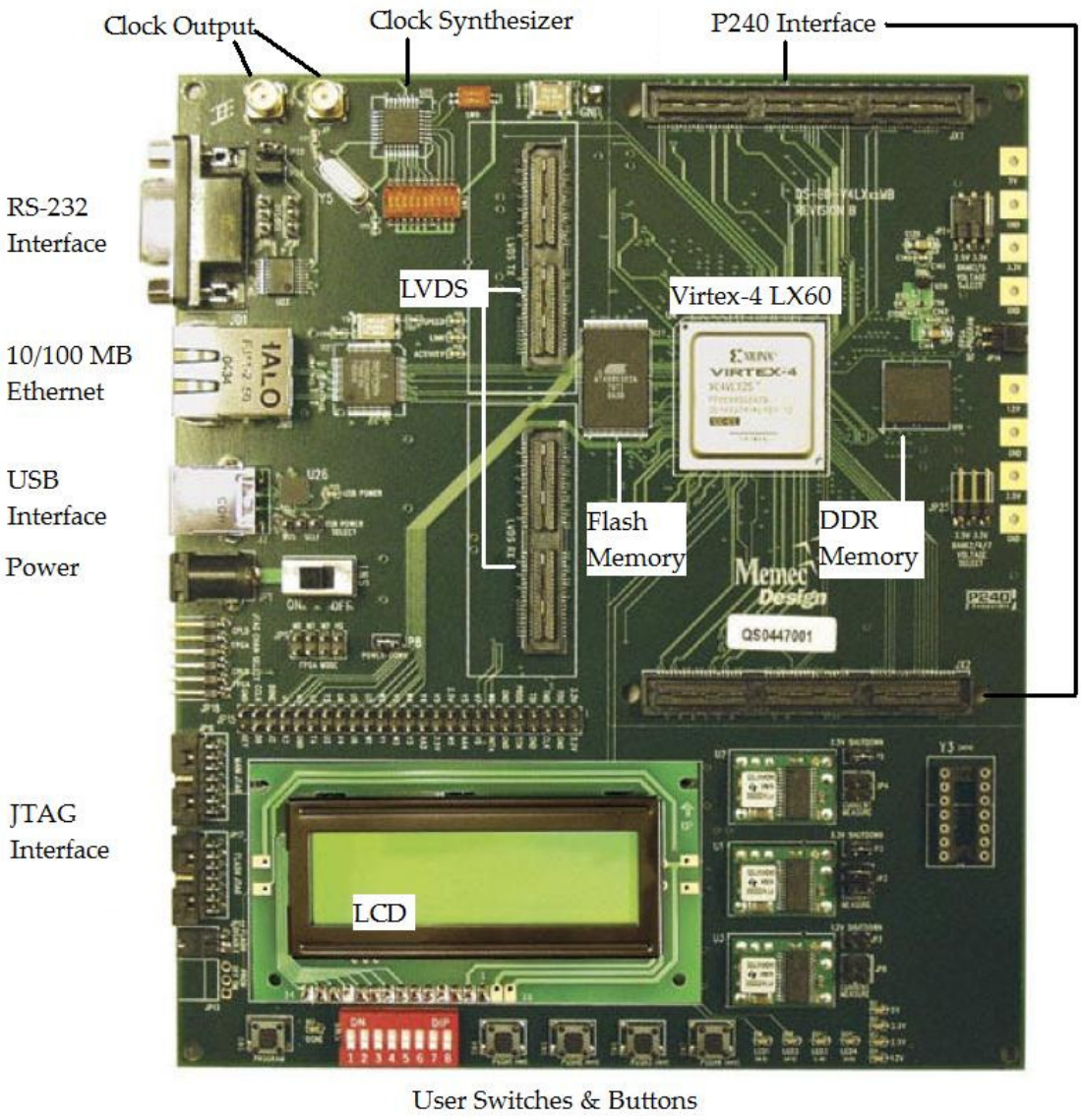

Figure A1.7 The Virtex-4 LX Development Board

Table A1.2 Key Features of the Virtex-4 LX Development Board

Xilinx Virtex-4 LX60 -10FF668 FPGA
64 MB of DDR SDRM
4 MB of Flash
16-Bit LVDS Transmit and Receive Interface
10/100 Ethernet PHY
Programmable LVDS Clock Source (25-700 MHz)
User LVDS Clock Outputs via Differential SMA Connectors
On-board 100 MHz LVTTL Oscillator
On-board LVTTL Oscillator Socket (4/8-Pin Oscillators)
P240 Connectors
LCD Panel
32Mb Serial Flash for FPGA configuration
PC4 JTAG Programming/Configuration Port
SystemACE Module Connector
RS232 Port
Four User LEDs
Four User Push Button Switches
An 8-position DIP Switch
USB-RS232 Bridge

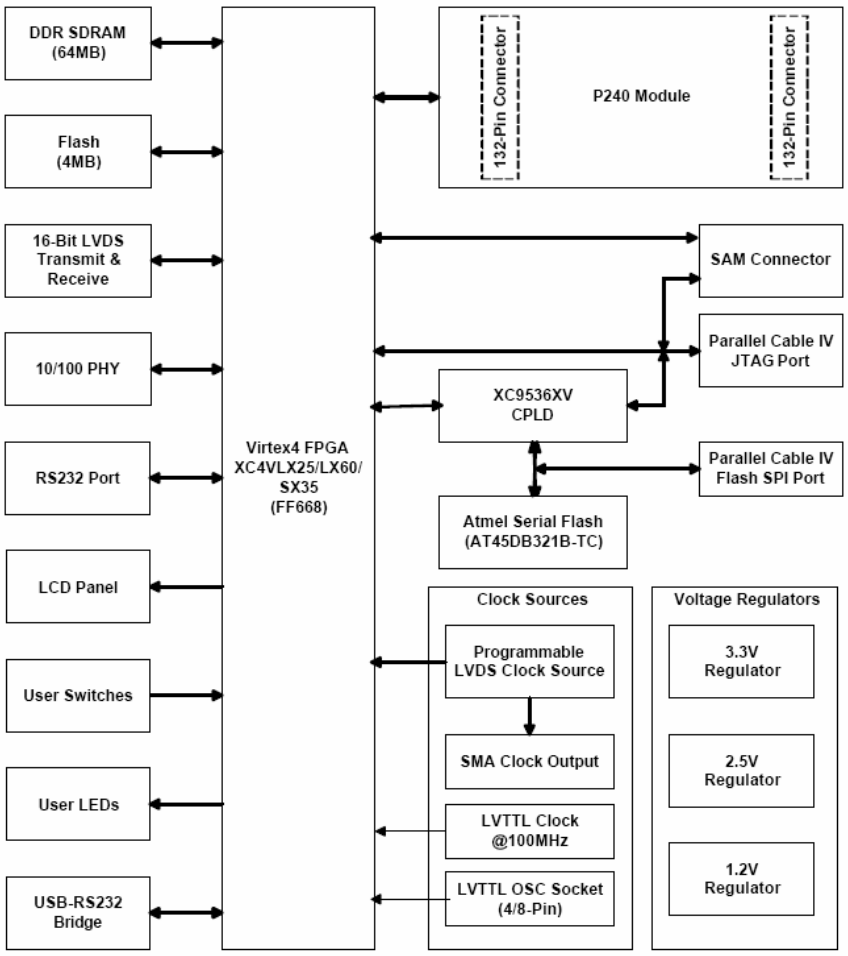

Figure A1.8 Virtex-4 Development Board Block Diagram

The centerpiece of this system is the Xilinx Virtex-4 LX60 FPGA. The Virtex-4 LX60 FPGA consists of a 128 x 52 array of Configurable Logic Blocks (CLB). Each of these CLBs contains four identical slices. Each slice consists of 4 input look-up tables (LUT), flip-flops, multiplexors, arithmetic logic, carry logic, and dedicated internal routing. The chip also includes 2880 kbits Block RAM memory consisting of 160 blocks of 18 kbits RAM. Eight Digital Clock Managers (DCM) provide zero clock delay.

Further, the DCMs can also provide various phases of the source clock, e.g. 90º, 180º, 270º. The DCMs can also act as clock multipliers or dividers. Although the Virtex-4 LX60 FPGA is not optimized for signal processing applications, its resources are more than adequate for the implementation of a simple digital spectroscopic measurement system. The main resources of the Virtex-4 LX60 FPGA are listed in Table A1.3.

Table A1.3 Resource of the Xilinx Virtex-4 LX60 FPGA

CLB Resources	CLB Array (Row x Column)	128 x 52
	Slices	26,624
	Logic Cells	59,904
	CLB Flip Flops	53,248
Memory Resources	Max. Distributed RAM Bits	425,984
	Block RAM (18 kbits each)	160
	Total Block RAM	2,880
Clock Resource	Digital Clock Managers (DCM)	8
	Phase-matched Clock Dividers (PMCD)	4
I/O Resource	Max Select I/O	640
	Total I/O Banks	13
	Digitally controlled Impedance	Yes
	Max differential I/O Pairs	320
DSP Resource	XtremeDSP Slices	64
Speed Grades	Commercial (Slowest to fastest)	-10,-11,-12

The Virtex-4 Development Board provides 64MB of DDR SDRAM memory. The width of the memory is 16-bit. The data pins, address pins, and control pins are directly connected to the Virtex-4 LX60 FPGA. A high-level block diagram of the DDR SDRAM interface is shown below in Figure A1.9. In this design, the γ-ray spectra are stored on this DDR SDRAM before they are transferred to the PC through the RS232 interface.

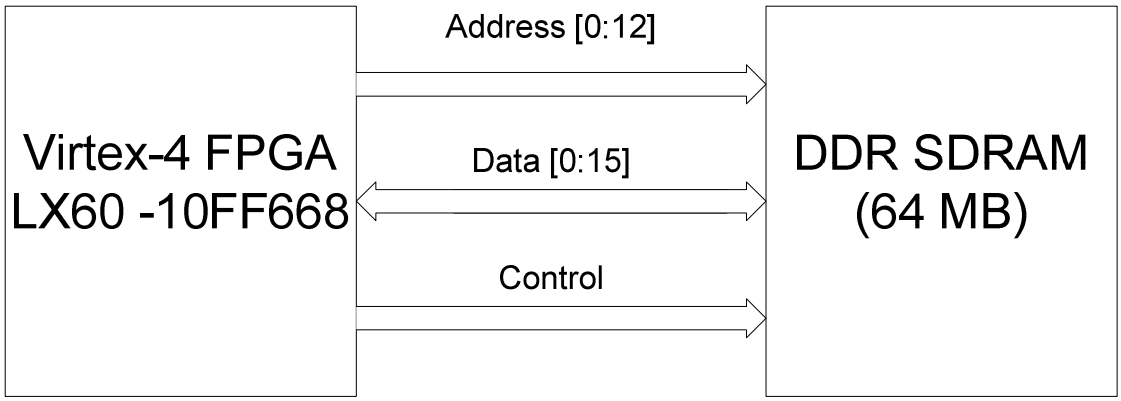

Figure A1.9 DDR SDRAM Block Diagram

The clock resources on the Virtex-4 LX development board can be grouped into two categories: differential clocks and single-ended clocks. The clock generation section provides all the clocks required for a MicroBlaze processor, the I/O devices on the board (serial port, USB-UART bridge, 10/100 MB Ethernet, LCD and etc.), as well as the DDR SDRAM, Flesh RAM. The differential clocks are mainly used by the LVDS interface, which was not implemented in this design.

An on-board 100 MHz oscillator supplies the system clock to the processor section. This 100 MHz clock will be fed into the Digital Clock Manager units to generate clock sources with various phases and frequencies. In addition to this 100 MHz oscillator, there is a socket provided on the development board. An 8-pin or 4-pin oscillator can be used to provide single ended LVTTL clock input with other frequencies. Figure A1.10 shows the clock resources available on the Virtex-4 LX development board.

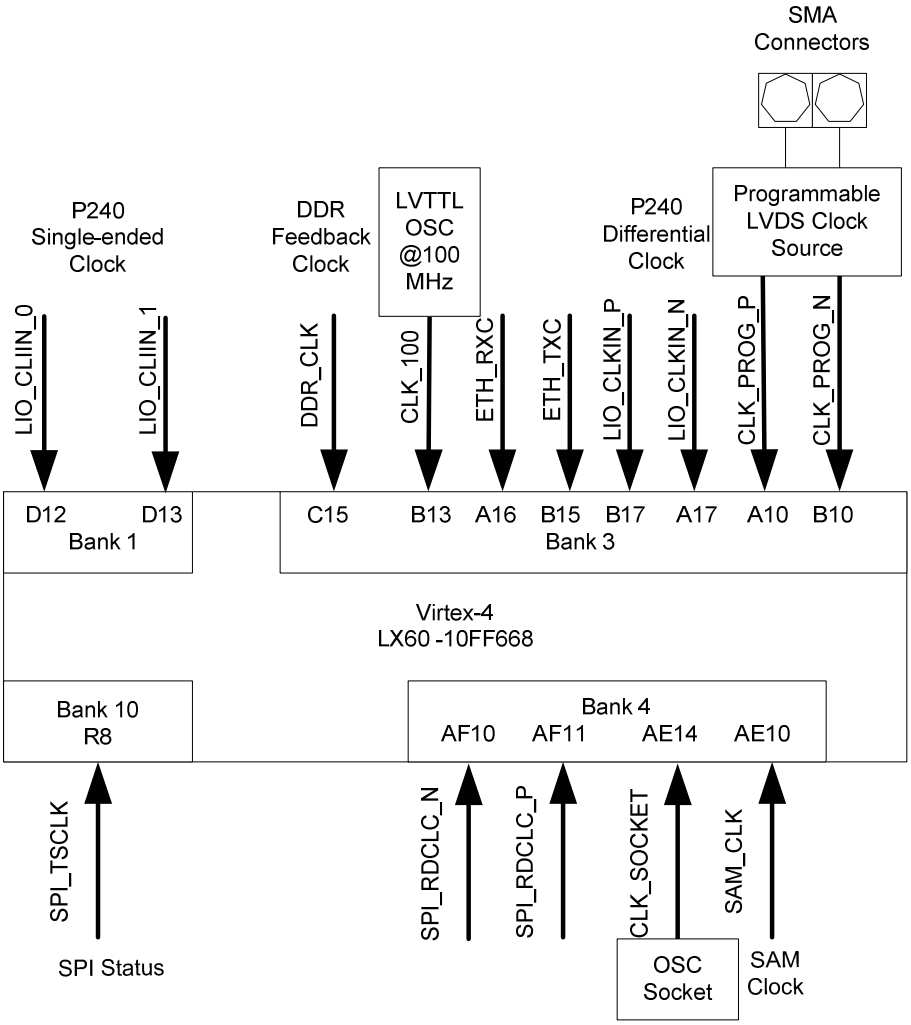

Figure A1.10 Clock Resources on the Virtex-4 LX Development Board

A programmable LVDS clock synthesizer is offered on the Virtex-4 LX development board to generate a reference clock for the LVDS interface. The differential output is also suitable in DSP designs to drive external DAC and ADC modules. In this design, the differential output from this clock synthesizer is fed to the P240 Analog

Module through the SMA connectors. The key features of the ICS8442 LVDS clock synthesizer are listed below in Table A1.4.

Table A1.4 Key Features of the ICS8442 LVDS Clock Synthesizer

Output Frequency Range	25 MHz to 700 MHz
RMS Period Jitter	2.7 ps (typical)
Cycle-to-cycle Jitter	27 ps (typical)
Output rise and fall time	650 ps (maximum)
Output Duty Cycle	48/52

Figure A1.11 shows a block diagram of the ICS8442 programmable LVDS clock synthesizer. The description of each pin is presented in Table A1.5.

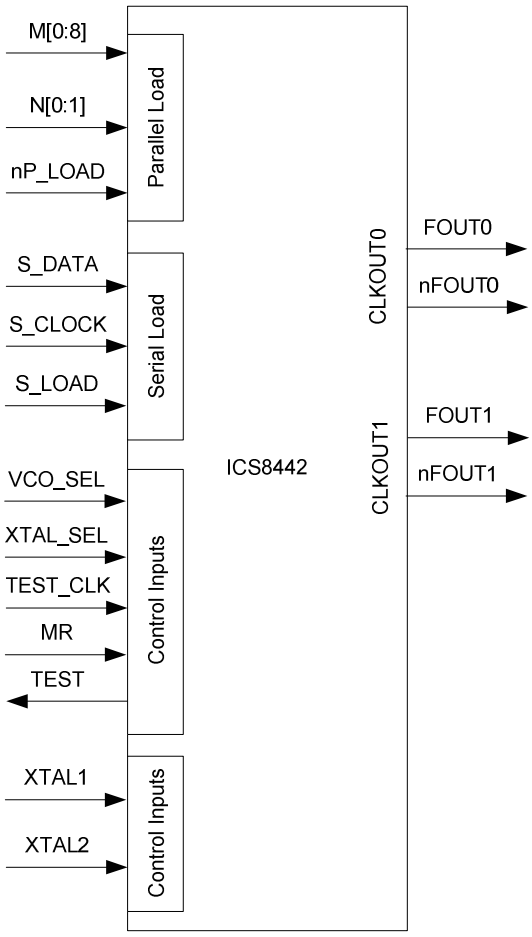

Figure A1.11 ISC8442 Clock Synthesizer Block Diagram

Table A1.5 ICS 8442 Clock Synthesizer Pin Description

Signal Name	Direction	Pull up/down	Description
M[0:4], M[6:8]	Input	Pull down	The M divider inputs, latched on the rising edge of the nP-LOAD signal
M[5]	Input	Pull up	
N[0:1]	Input	Pull down	The N divider inputs, latched on the rising edge of the nP-LOAD signal
TEST	Output		The TEST output is active during the serial mode of operations
MR	Input	Pull down	Active high reset signal
S_CLOCK	Input	Pull down	Serial interface clock input
S_DATA	Input	Pull down	Serial interface data input
S_LOAD	Input	Pull down	Serial interface load signal. The contents of the serial data shift register is loaded into the internal dividers on the rising edge of this signal
TEST_CLK	Input	Pull down	Test clock input
nP_LOAD	Input	Pull down	The rising edge of this signal is used to load the M and N divider into the device
XTAL1, XTAL2	Input	Pull down	Crystal clock input/output
XTAL_SEL	Input	Pull up	This signal is used to select between the crystal and the TEST_CLK input to the device. When this is high, crystal is selected.
VCO_SEL	Input	Pull up	This signal is used to place the internal Phase Lock Loop (PLL) in the bypass mode
FOUT0, FOUT1	Output		Positive LVDS clock outputs
nFOUT0, nFOUT1	Output		Negative LVDS clock outputs

In this design, a 25 MHz crystal was chosen as the input clock and the internal PLL was enabled for normal operation. The output ICS8442 output clock frequency can be calculated using the following formula (when a 25 MHz crystal is used as input clock source):

$$FOUT[0:1] = 25 \times M / N$$

The value of M and N can be set using the DIP Switches shown in Figure A1.12 below.

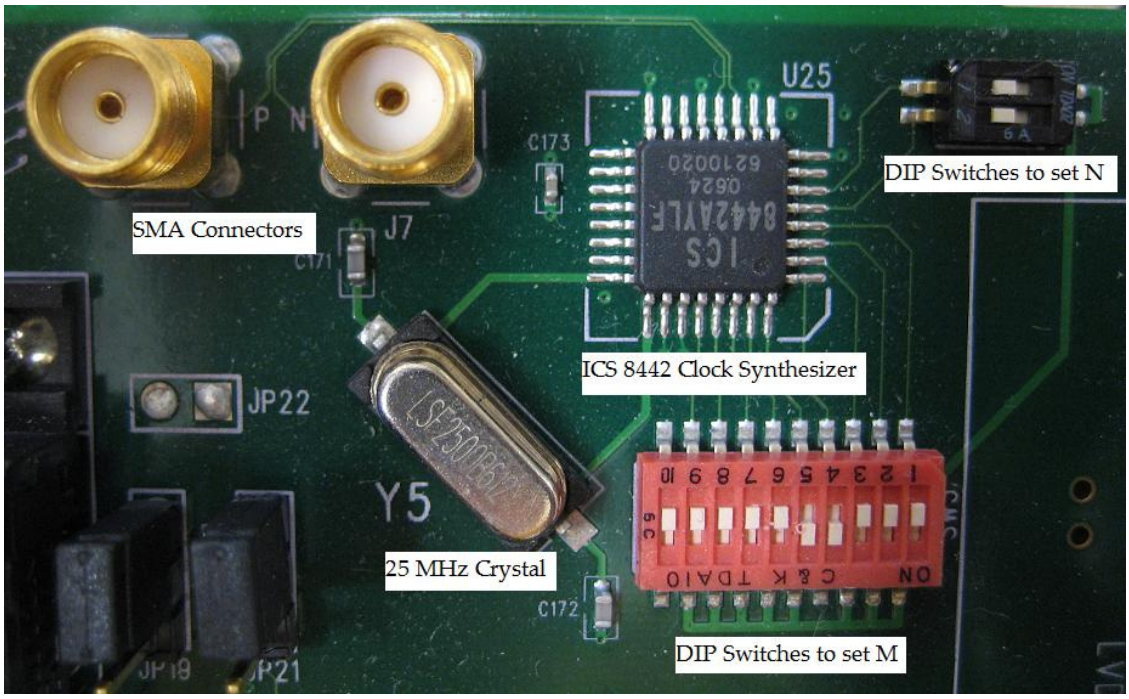

Figure A1.12 ICS 8442 Clock Synthesizer and Peripherals

M can be determined by setting the binary number M[0:8] using the DIP Switches. The valid values are between 8 and 28. N is set according to the rules shown in Table A1.6 below.

Table A1.6 Settings and Associated Values of N

N[1:0]	Value
00	1
01	2
10	4
11	8

In this design, the value of N is set to be 1 (00) and the value of M is set to be 16 (000010000). Hence, the frequency of the output clock source is:

$$FOUT[0:1] = 25 \times M / N = 25 \times 16 / 1 = 400MHz$$

As shown in Figure A1.13 below, FOUT0 is fed to the Virtex-4 FPGA chip for LVDS applications. FOUT1 is available through the SMA connectors for external add-on modules, for example the P240 Analog Module.

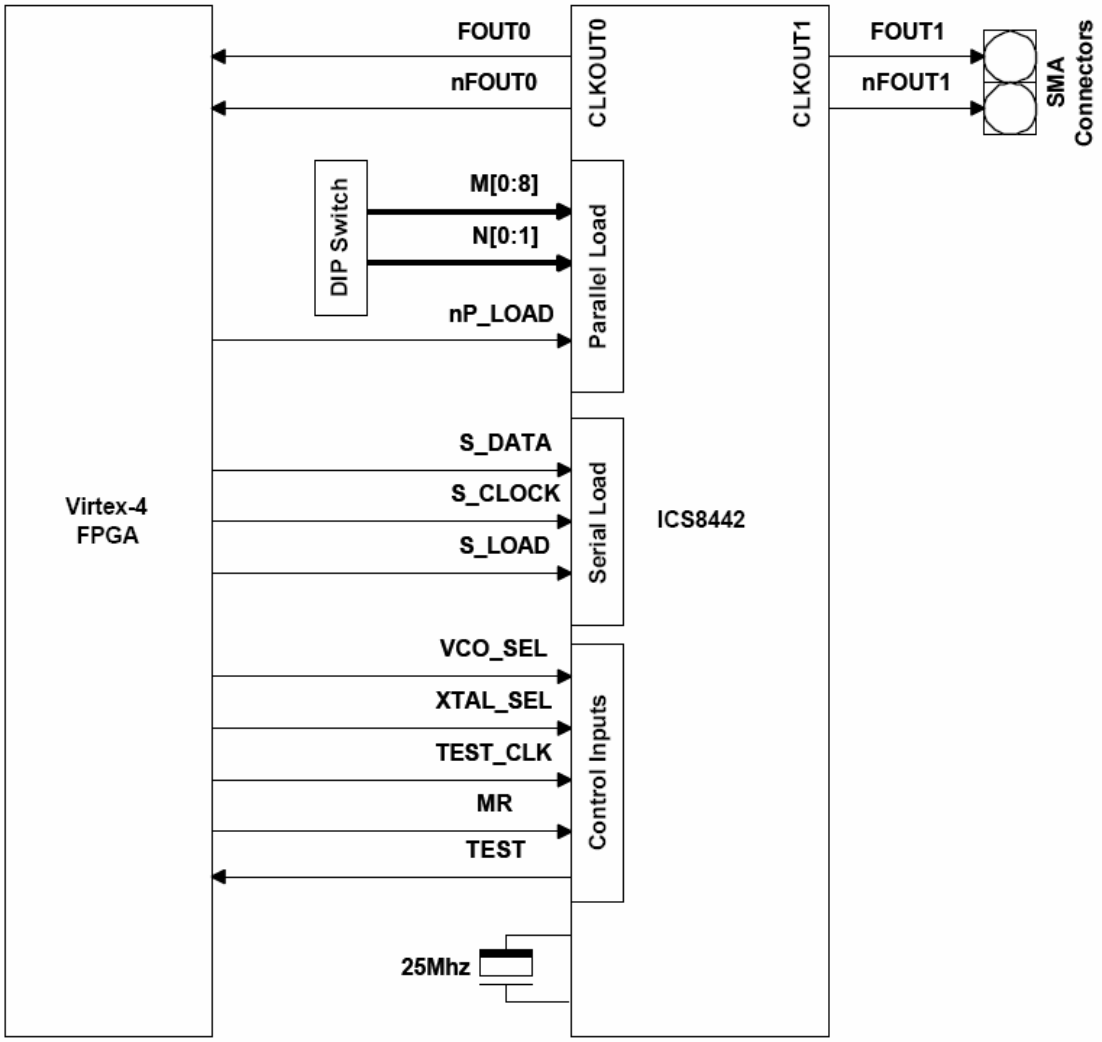

Figure A1.13 ICS8442 Clock Synthesizer Connections

Another feature of the development board that has been implemented in this digital spectroscopic measurement system design is the RS232 interface. The RS232 interface provided on the development board is equipped with available RX and TX

signals. Jumpers are used to connect the RTS and CTS signals. The connection is shown in Figure A1.14 below.

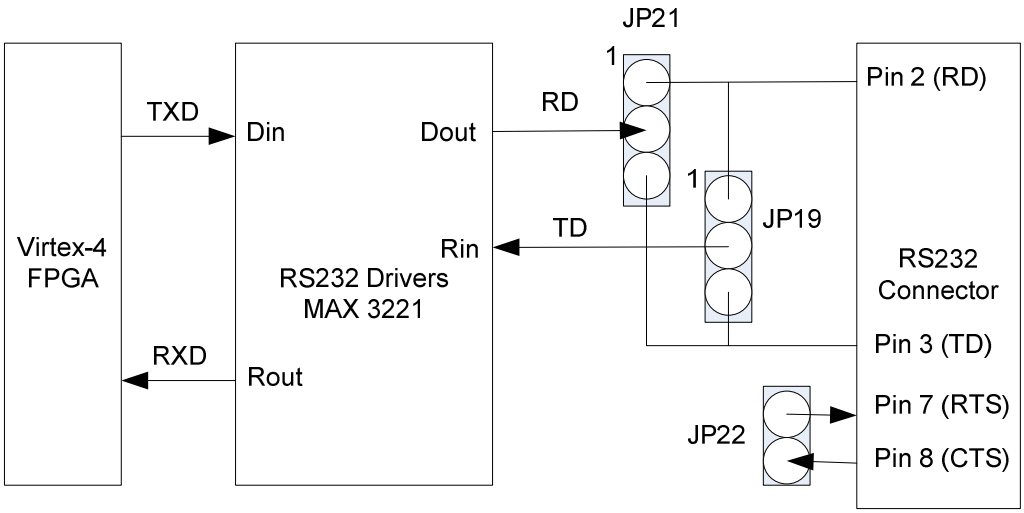

Figure A1.14 Connection of the RS232 Interface

The mode of operation can be set for the RS232 interface through two jumpers provided on the board, JP 19 and JP 21, shown in Table A1.7. In this design, the RS232 interface is set to Data Communication Equipment mode.

Table A1.7 Mode of Operation Settings

Model of Operation	JP 19	JP 21
Data Communication Equipment (DCE)	2-3	1-2
Data Terminal Equipment (DTE)	1-2	2-3

Appendix 2. Xilinx Blockset Components Utilized in the DAQ System Design

Table A2.1 Xilinx Blockset Components Utilized in this Design

Components	Description
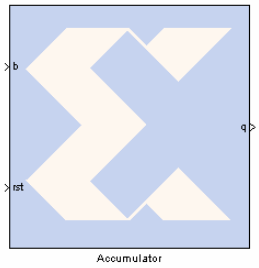	Implements an adder or subtractor based scaling accumulator. The current input is accumulated with a scaled current stored value. The scaling factor can be adjusted.
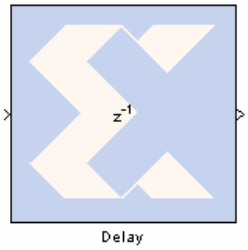	A delay line (shift register) of configurable length. The input will appear at the output after a specified number of sample periods.
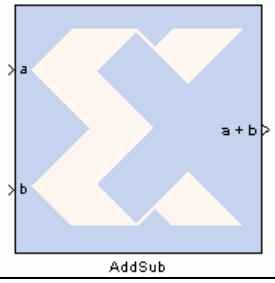	Implements an adder or subtractor. The operation can be fixed or switched dynamically.
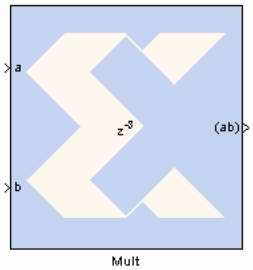	Implements a multiplier with the option to use the embedded multipliers available on Virtex-5, Virtex-4, Virtex-II and Spartan-3.

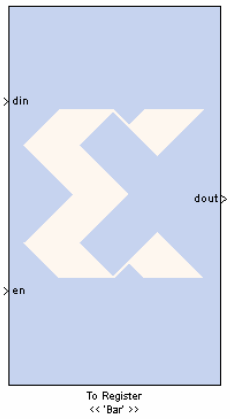	Implements a D flip-flop register and can be shared among multiple designs or sections of a design.
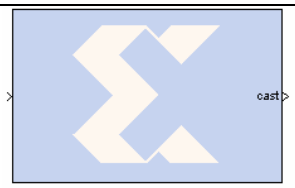	Convert the input to a desired arithmetic type.
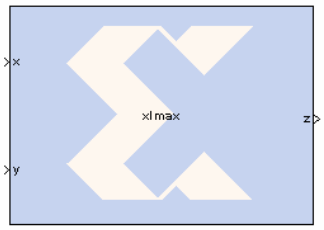	Import Matlab function and execute it within Simulink.
	Allows design in Simulink be attached to embedded processor systems created using the Xilinx Embedded Development Kit (EDK). In this design, models are exported as a pcore, which can be imported by EDK projects and attached to the MicroBlaze processor through a Fast Simplex Link (FSL) bus.
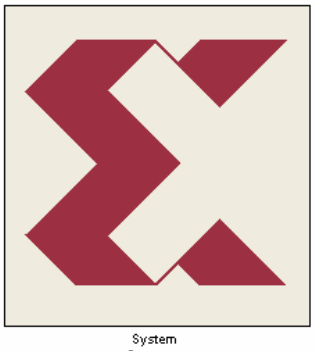	Provides control of system and simulation parameters. Used to invoke code generator. The compilation types include exporting the design to a Xilinx Embedded Development Kit (EDK) project.

BIBLIOGRAPHY

1. C.E. Grassley, M. Baucus, B. Thomas, C. B. Rangel, "Container security: Expansion of key customs programs will require greater attention to critical success factors," General Accounting Office, US Congress, GAO-03-770, July 25, 2003

2. Maritime Transport Committee, "Security in maritime transport: Risk factors and economic impact, " Organization for Economic Co-operation and Development; Directorate for Science, Technology and Industry, July, 2003

3. D. Reilly, N. Ensslin, H. Smith, Jr. and S. Kreiner, "Passive Nondestructive Assay of Nuclear Materials"

4. T. Gosnell, et al., "Gamma-ray identification of nuclear weapon materials", UCRL-ID-127436, Lawrence Livermore National Laboratory, 1997

5. S. Normand, B. Mouanda, S. Haan and M. Louvel, "Discrimination methods between neutron and gamma rays for boron loaded plastic scintillators," *Nucl. Instr. and Meth. A* **484**, pp. 342, 2002

6. T. Miller, "Measurement of pulse shape discrimination parameters for several scintillators," *Nucl. Instr. and Meth.* **63**, pp. 121, 1968

7. J. Czirr, "A comparison of scintillator solvents for pulse shape discrimination," *Nucl. Instr. and Meth.* **88**, pp. 321, 1970

8. R. Winyard, "Pulse shape discrimination in inorganic and organic scintillators," *Nucl. Instr. and Meth.* **98**, pp. 525, 1972

9. T. Kelly, J. Merrigan and R. Lambrecht, "Comparison of plastic scintillators with nanosecond lifetimes," *Nucl. Instr. and Meth.,* **109**, pp. 233, 1973

10. P. Lyons, J. Stevens, "Time response of plastic scintillators," *Nucl. Instr. and Meth.* **114**, pp. 313, 1974

11. F. Lynch, "Basic limitation of scintillation counters in time measurements," *IEEE Trans. Nucl. Sci.* NS-22(1), 58, 1975

12. S. Sanyal, S. Pancholi and S. Gupta, "Sub-nanosecond timing studies with plastic scintillation detectors," *Nucl. Instr. and Meth.* **136**, pp. 157, 1976

13. T. Gozani, "Active Nondestructive Assay of Nuclear Materials, Principles and Applications", Chapter 2

14. R. Kouzes, E. Siciliano, J. Ely, P. Keller and R. McConn, "Passive neutron detection for interdiction of nuclear material at borders", *Nucl. Instr. and Meth. A* **584**, pp. 383, 2008

15. R. Auguston and T. Reilley, Los Alamos Laboratory, "Fundamentals of passive nondestructive assay of fissionable material," LA-5651-M, September 1974

16. T. Dragnev, "Non-destructive assay techniques for nuclear safeguards measurements," *Atom. Energ. Rev.*, **11**, (no.2) pp. 341

17. B. Micklich, D. Smith, T. Massey, C. Fink, and D. Ingram, "FIGARO: detecting nuclear materials using high-energy gamma-rays," *Nucl. Instr. and Meth. A* **505**, pp. 466, 2003

18. V. Deshmukh, and V. Bhoraskar, "Bremsstrahlung spectra from lead and tantalum at 6 MeV electron energy," *J. Radioanal. Nucl. Chem.*, Letters **103**, pp. 87, 1986

19. IAEA Photonuclear Data Library, http://www-nds.iaea.org/photonuclear/

20. J. Jones, "Active non-intrusive inspection technologies for homeland defense," *Sixth International Meeting on Nuclear Application of Accelerator Technology*, 2003

21. J. Jones, et al., "Proof-of-concept assessment of a photofission-based interrogation system for the detection of shielded nuclear material, " INEEL-EXT-2000-01523, 2000

22. J. Jones, et al., "Photofission-based, nuclear material detection: technology demonstration, " INEEL-EXT-02-0106, 2002

23. J. Jones, B. Blackburn, D. Norman, S. Watson, K. Haskell, J. Johnson, A. Hunt, F. Harmon and C. Moss, "Status of the prototype pulsed photonuclear assessment (PAP) inspection system," *Nucl. Instr. and Meth. A* **579**, pp. 353, 2007

24. J. Jones, D. Norman, K. Haskell, J. Sterbentz, W. Yoon, S. Watson, J. Johnson, J. Zabriskie, B. Bennett, R. Watson, C. Moss and F. Harmon, "Detection of shielded nuclear material in a cargo container," *Nucl. Instr. and Meth. A* **562**, pp. 1085, 2006

25. C. Moss, C. Goulding, C. Hollas and W. Myers, "Linear accelerator-based active interrogation for detection of highly enriched uranium," *Application of Accelerators in Research and Industry: 17th Int'l. Conference*, 2004

26. C. Moss, C. Goulding, C. Hollas and W. Myers, "Neutron detectors for active interrogation of highly enriched uranium," *IEEE Trans. Nucl. Sci.*, Vol. 51, no. 4, pp. 1677, 2004

27. M. Gmar and J. Capdevila, "Use of delayed gamma spectra for detection of actinides (U, Pu) by photofission," *Nucl. Instr. and Meth. A* **422**, pp. 841, 1999

28. D. Slaughter, et al., Lawrence Livermore National Laboratory, "The 'nuclear car wash': a scanner to detect illicit special nuclear material in cargo containers," UCRL-JRNL-202106

29. D. Slaughter, M. Accatino, A. Bernstein, P. Biltoft, J. Church, M. Descalle, J. Hall, D. Manatt, G. Mauger, T. Moore, E. Norman, D. Petersen, J. Pruet and S. Prussin, "The nuclear car wash: A system to detect nuclear weapons in commercial cargo shipments," *Nucl. Instr. and Meth. A* **579**, pp. 349., 2007

30. S. Prussin, M. Descalle, J. Hall, J. Pruet, D. Slaughter, M. Accatino, O. Alford, S. Asztalos, A. Bernstein, J. Church, T. Gosnell, A. Loshak, N. Madden, D. Manatt, G. Mauger, A. Meyer, T. Moore, E. Norman, B. Pohl, D. Petersen, B. Rusnak, T. Sundsmo, W. Tenbrook and R. Walling, "Comparison of tests with 14 MeV neutrons to a Monte Carlo model for interrogation of thick cargos for clandestine fissionable materials," *Nucl. Instr. and Meth. A* **569**, pp. 853, 2006

31. E. Norman, S. Prussin, R. Larimer, H. Shugart, E. Browne, A. Smith, R. McDonald, H. Nitsche, P. Gupta, M. Frank, T. Gosnell, "Signatures of fissile materials: high-energy γ rays following fission," *Nucl. Instr. and Meth. A* **521**, pp. 608, 2004

32. B. Blackburn, A. Hunt, J. Jones, F. Harmon, C. Moss, S. Watson, J. Mihalczo, J. Johnson, "Utilization of actively induced prompt radiation emission for nonproliferation applications," *Conference on Accelerator Applications in Research and Industry*, 2006

33. F. Ruddy, J. Seidel, R. Flammang, B. Petrovic, A. Dulloo, T. Congedo, "Pulsed neutron interrogation for detection of concealed special nuclear materials," *Proc. SPIE* Vol. **6213**, 2006

34. C. Fink, D. Smith, B. Micklich and T. Massey "Gamma rays produced by 1.75 to 4 MeV proton bombardment of thick aluminum targets," *Nucl. Instr. and Meth. A* **505**, pp. 5., 2003

35. B. Micklich, D. Smith, T. Massey, C. Fink and D. Ingram, "Measurement of thick target high energy gamma ray yields from the $^{19}F(p, \alpha\gamma)^{16}O$ reaction," *Nucl. Instr. and Meth. A* **505**, pp. 1, 2003

36. U. Kniessl, H.H. Pitz and A. Zilges, "Investigation of Nuclear Structure by Resonance Fluorescence Scattering," *Prog. Part. Nucl. Phys.* **37**, pp. 349, 1996

37. W. Bertozzi, R. Ledoux, "Nuclear resonance fluorescence imaging in non-intrusive cargo inspection," *Nucl. Instr. and Meth. B* **241**, pp. 820, 2005

38. W. Bertozzi, R. Ledoux, "Nuclear resonance fluorescence imaging in non-intrusive cargo inspection," *Conference on Accelerator Applications in Research and Industry*, 2004

39. C. Hollas, D. Close and C. Moss, "Analysis of fissionable material using delayed gamma rays from photofission," *Nucl. Instr. and Meth. B* **24/25**, pp. 503, 1987

40. General Atomic, "Application of photo induced reactions to nuclear materials safeguards problems," GA-10106, San Diego, California, 1970

41. T. Gozani, "Threshold photofission with electron accelerators – why, how and applications," *Atomkernenergie*, **19**, pp. 63, 1972

42. R. Tuttle, "Delayed neutron spectra and their importance in reactor calculations," *Nucl. Sci. and Eng,* **56**, pp.37, 1975

43. Los Alamos Scientific Laboratory, "Nuclear safeguards research and development," LA-4227-MS, pp. 12, 1969

44. K. Baumung, K. Bohnel, J. Klunker, M. Kuchle, and J. Wolff, "Investigations into non-destructive safeguards techniques," *Proceedings IAEA-Karlsruhe, Germany Symposium on Safeguards Techniques*, vol. **2**, pp. 192, 1970

45. General Atomic, "Application of photo induced reactions to nuclear materials safeguards problems," GA-9614, San Diego, California, 1969

46. R. Metzger, K. Riper and M. Jones, "Ford motor company NDE facility shielding design," *Radiation Protection Dosimetry*, vol. **116**, pp. 236, 2005

47. F. Brown, et al., "MCNP Version 5," *Trans. Am. Nucl. Soc*., **87**, pp. 273, 2002

48. T2 Nuclear Information Service, Los Alamos National Laboratory, http://t2.lanl.gov/

49. Fission product yields, Lawrence Berkeley National Laboratory, http://ie.lbl.gov/fission.html

50. P. Fisher and L. Engle, "Delayed gammas from fission," *Physics Review*, **134**, pp. 810, 1964

51. N. Saurel, J. Capdevila, N. Huot and M. Gmar, "Experimental and simulated assay of actinides in a real waste package," *Nucl. Instr. and Meth. A* **550**, pp. 691, 2005

52. M. Gmar, F. Jeanneau, F. Lainė, H. Makil, B. Poumarede and F. Tola, "Assessment of actinide mass embedded in large concrete waste packages by photon interrogation and photofission," *Applied Radiation and Isotopes*, **63**, pp. 613, 2005

53. A. Jung, S. Lindenstruth, H. Schacht, B. Starck, R. Stock, C. Wesselborg, R. Heil, U. Kneissl, J. Margraf, H. Pitz and F. Steiper, "Electric and magnetic dipole excitations to bound states in ^{70,72,74,76}Ge," *Nucl. Phys. A* **584**, pp. 103, 1995

54. R. Duffield, "Fission energy barrier," Los Alamos Scientific Laboratory of the Univerisyt of California LA-1399, 1951

55. R. Belusevic, G. Nixon and D. Shaw, "An 80 Mbytes/s data transfer and processing system," *Nucl. Instr. and Meth. A* **295**, pp. 391, 1990

56. F. Goulding, "Pulse-shaping in low-noise nuclear amplifiers: a physical approach to noise analysis," *Nucl. Instr. and Meth* **100**, pp. 493, 1972

57. V. Jordanov, and G. Knoll, "Digital synthesis of pulse shapes in real time for high resolution radiation spectroscopy," *Nucl. Instr. and Meth A* **345**, pp. 337, 1994

58. V. Jordanov, G. Knoll, A. Huber, and J. Pantazis, "Digital techniques for real-time pulse shaping in radiation measurements," *Nucl. Instr. and Meth A* **353**, pp. 261, 1994

59. A. Georgiev, and W. Gast, "Digital pulse processing in high resolution high throughput gamma-ray spectroscopy," *IEEE Trans. Nucl. Sci.*, Vol. **40**, no. 4, pp. 770, 1993

60. M. Lauer, "Digital signal processing for segmented HPGe detectors preprocessing algorithms and pulse shape analysis," *Dissertation, Ruperto-Carola University of Heidelberg, Germany,* 2004

61. E.T.E. Reedy, et al., Nucl. Instr. And Meth. A (2009), doi:10.1016/j.nima. 2009.04.048

62. D. Wehe, H. Yang, and M. Jones, "Observation of ^{238}U photofission products," *IEEE Trans. Nucl. Sci.*, Vol. **53**, no. 3, pp. 1430, 2006

63. L. Kull, R. Bramblett, T. Gozani, and D. Rundquist, "Delayed neutrons from low energy photofission," *Nucl. Sci. and Eng.*, **39**, pp. 163, 1970

64. Van Grieken, R. E., Markowicz, A. A., "Handbook of X-Ray Spectrometry 2nd ed. , " Marcel Dekker Inc: New York, 2002

65. W. Kuhn, "Scattering of Thorium C″ γ-radiation by Radium G and Ordinary Lead, " *Phil. Mag.* **8**, pp. 625, 1929

66. L. Meitner and H. Hupfeld, "About the absorption law for short-wave γ radiation, " *Z. Phys.* **67**, pp. 147, 1931

67. F. Metzger, "Lower limit for the lifetime of the 0.8-Mev excited level of ^{96}Mo," *Phys. Rev.* **83**, pp. 842, 1951

68. F. Metzger, and W. Todd, "Lower limit for the lifetime of the 665-kev excited state of ^{96}Mo," *Phys. Rev.* **91**, pp. 1286, 1953

69. E. Pollard, and D. Alburger, "Large angle scattering of ^{24}Na gamma radiation," *Phys. Rev.* **74**, pp. 926, 1948

70. P. Moon, " Resonant Nuclear Scattering of Gamma-Rays: Theory and Preliminary Experiments," *Proc. Phys. Soc. Lond.* **A64**, pp. 76, 1951

71. L. Schiff, "Resonance fluorescence of nuclei, " *Phys. Rev.* **70**, pp. 761, 1946

72. F. Metzger, "Resonance fluorescence in nuclei," *Prog. In Nucl. Phys.* **7**, pp. 89, 1959

73. N. Pietralla, I. Bauske, O. Beck, P. Brentano, W. Geiger, R. Herzberg, U. Kneissl, J. Margraf, H. Maser, H. Pitz, and A. Zilges, " Absolute level widths in ^{27}Al below 4 MeV, " *Phys. Rev. C* **51**, pp. 1020, 1995

74. J. Margraf, A. Degener, H. Friedrichs, R. Heil, A. Jung, U. Kneissl, S. Lindenstruth, H. Pitz, H. Schacht, U. Seemann, R. Stock, and C. Wesselborg, " Photoexcitation of low-lying dipole transitions in ^{236}U, " *Phys. Rev. C* **42**, pp. 771, 1990

75. P. Mohr, J. Enders, T. Hartmann, H. Kaiser, D. Schiesser, S. Schmitt, S. Volz, F. Wissel, and A. Zilges, "Real photon scattering up to 10 MeV: the improved facility at the Darmstadt electron accelerator S-DALINAC," *Nucl. Instr. and Meth A* **423**, pp. 480, 1999

76. U. Berg, and U. Kneissl, "Recent progress on nuclear magnetic dipole excitations," *Ann. Rev. Nucl. Part. Sci.* **37**, pp. 33, 1987

77. N. Ryezayeva, T. Hartmann, Y. Kalmykov, H. Lenske, P. Neumann-Cosel, V. Ponomarev, A. Richter, A. Shevchenko, S. Volz, and J. Wambach, "Nature of low-energy dipole strength in nuclei: the case of a resonance at particle threshold in 208Pb," *Phys. Rev. Let.* Vol. **89**, no. 27, 2002

78. G. Warren, J. Caggiano, W. Hensley, E. Lepel, S. Pratt, C. Tien, W. Bertozzi, S. Korbly, R. Ledoux, and W. Park, "Nuclear Resonance Fluorescence of ^{235}U," *IEEE NSS Conference,* 2006

79. J. Pruet, D. McNabb, C. Hagmann, F. Hartemann, and C. Bartly, "Detecting clandestine material with nuclear resonance fluorescence," *J. Appl. Phys*. **99**, pp. 123102

80. H. Weller, and M. Ahmed, "The HIγS facility: a free-electron laser generated gamma-ray beam for research in nuclear physics," *Mod. Phys. Let. A* Vol. **18**, No. 23, pp. 1569, 2003

81. Duke University, North Carolina State University, University of North Carolina at Chapel Hill, "High intensity gamma-ray source," *Progress Report,* 2003-2004

82. C. Bartly, and F. Hartemann, "T-REX: Thomson-Radiated Extreme X-rays Moving X-Ray Science into the Nuclear Applications Space with Thompson Scattered Photons," *LLNL Report UCRL-TR-206825,* 2004

83. J. Pruet, D. McNabb, "T-REX: design considerations for detection of concealed ^{238}U," *LLNL Report UCRL-TR-219071,* 2006

84. J. Pruet, D. Lange, "Contraband detection with nuclear resonance fluorescence: feasibility and impact," *LLNL Report UCRL-TR-227067,* 2007

85. C. Barty, "FIND: fluorescence imaging in the nuclear domain," *LLNL Report UCRL-TR-210425,* 2005

86. H. Bethe, and G. Placzek, "Resonance effects in nuclear processes," *Phys. Rev.* **51***,* pp. *450,* 1937

87. K. Siegbahn, "α,β,γ - spectroscopy," North Holland, Amsterdam, 1965

88. A. Wapstra, G. Nigh, and R. Lieshout, "Nuclear spectroscopy tables," North Holland, Amesterdam, 1959

89. H. Bethe, "Nuclear physics B. Nuclear dynamics, Theoretical," *Rev. Mod. Phys.* **9** pp. 69, 1937

90. W. Lamb, "Capture of neutrons by atoms in a crystal," *Phys. Rev.* ***55*** pp. 190, 1939

91. L. Grodzins, "Lifetime of a 1^- level in Sm^{152}," *Phys. Rev.* **109,** pp. 1014, 1958

92. N. Burgov, and Y. Terekhov, Soviet Journ. Atomic Energy **2,** pp. 629, 1957

93. V. Rasmussen, F. Metzger, and C. Swann, "Lifetimes of the 4.43 MeV excited state of C^{12} and the 4.46 MeV excited state of B^{11}," *Phys. Rev.* **110,** pp. 154, 1958

94. W. Bertozzi, "Material identification and object imaging using nuclear resonance fluorescence," 2005

95. http://www.gel.usherbrooke.ca/casino/What.html

96. http://www.comsol.com/

97. J. Cooper, and D. Koltick, "Optimization of time and energy resolution at high count rates with a large volume coaxial high purity germanium detector," *Nuclear Science Symposium Conference Record, IEEE,* vol. **4**, pp. 2420, 2001

98. "Tables of x-ray mass attenuation coefficients and mass energy-absorption coefficients, " *National Institute of Standards and Technology*

99. J. Hartwell, and R. Gehrke, "Observation on the background spectra of four $LaCl_3$(Ce) scintillation detectors", *Applied Radiation and Isotopes* **63**, pp. 223, 2005

100. G. Knoll, "Radiation Detection and Measurement", pp. 335-341, Chapter 10, *Third Edition*

101. "P240 Analog Module User Guide," Avnet Electronic Marketing, 2005

102. "Virtex4 MB Development Board User Guide," Avnet Electronic Marketing, 2005

103. http://www.cadence.com/products/orcad/pspice_simulation/pages/default.aspx